# TECHNICAL ARTICLES
# VOL. 01

ASG SUPERCONDUCTORS

This collection of technical articles by ASG Superconductors from 2018 provides a vivid illustration of the often complex activities of a company in the high technology sector, made possible thanks to the skill and enthusiasm of all the people who every day contribute with their work.
Superconductivity was discovered in 1911, but the technology and applications linked to it are still “young”: recent achievements include the discovery of the Higgs Boson, the development and refinement of MRI magnetic resonance imaging and major steps forward in hadron therapy. Our current activities promise to bring us closer to harnessing nuclear fusion, providing a radical new and inexhaustible source of energy for the planet.
We can expect many further innovations to arise from the application of superconducting technology, which we hope to be able to relate in future volumes of this collection.

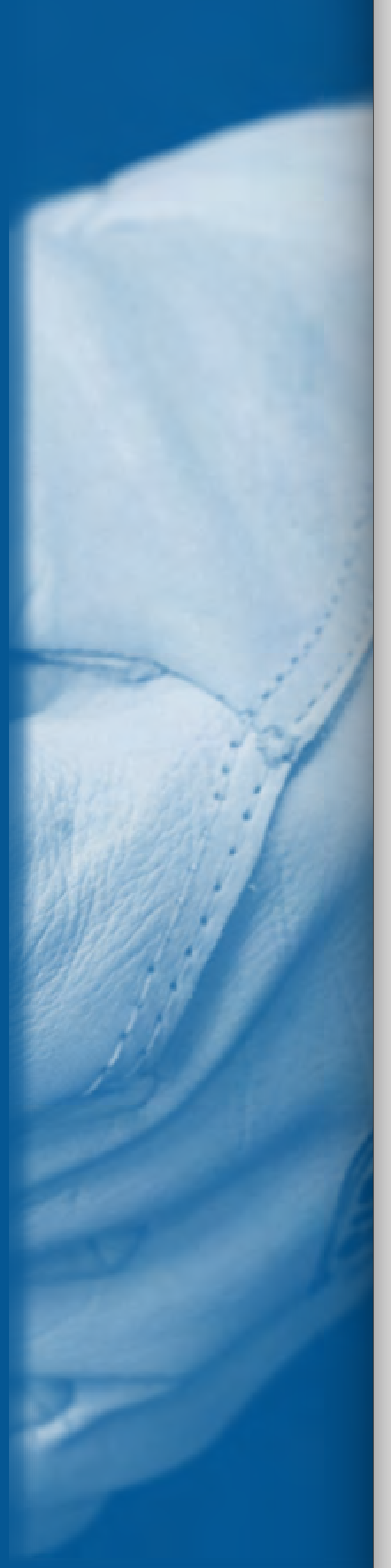

# TECHNICAL ARTICLES
# VOL. 01

A very special "thank you" to the authors and to all ASG's people.
Your everyday work at the technological frontier is paving the way to the future of research, energy and med-tech applications.

# FAULT CURRENT LIMITER

Rainbow behind high voltage electricity cables
near Great Wilbraham Cambridgeshire, England
© GettyImages, Ian Cumming / Design Pics





# FAULT CURRENT LIMITER: INNOVATIVE SOLUTIONS FOR ELECTRIC NETWORKS PROTECTION USING HIGHER TEMPERATURE SUPERCONDUCTING MATERIALS

David Klaus, Christian-Eric Bruzek

A saturated-core fault current limiter with superconducting magnets manufactured by ASG Magnets & Systems Unit is described.
The magnet coils are wound using magnesium diboride superconducting wire manufactured by the Columbus Unit of ASG Superconductors.

Magnesium diboride wire, optimised for this application by the Columbus division of ASG Superconductors has been incorporated into dry-cooled superconducting magnet assemblies by ASG in Genoa.
The magnets have been shown to effectively saturate the cores of a 36kV; 800A FCL and to withstand repeated fault currents without problems, including a fault of 3 seconds duration. The required performance of the FCL was achieved.

The ASG limiter has an "open-core" architecture and magnesium diboride wire has been used for the solenoids (magnets) which provide the saturating flux. The operating principle is identical to that of the closed[1]core arrangement. Any failure of the magnet cooling system or the magnet dc power supply results in the FCL shifting to a high-impedance state, so this approach is inherently fail-safe.

## 1 Introduction

Electricity supply networks are designed to have as low as possible source impedance because the widely varying demand for power results in widely varying load current magnitudes and it is necessary to maintain the network voltage at a constant level. This can be accomplished for slow demand shift (day/night, summer/winter) by means of transformer tap-changers, but rapid shifts in demand (industry, transport, domestic peaks) must not affect the supply voltage beyond strict limits, typically $\pm$ 6%.

Short-circuits in networks occur occasionally, due to cable or plant failure (excavation, insulation breakdown) or transient flashovers on overhead lines (lightning, vegetation). The current, known as fault current, which flows in the short-circuit, is limited only by the necessarily low network source impedance and can amount to tens of thousands of Amperes. Network components such as cables, lines, transformers and switchgear have limited fault current capacities which if exceeded can lead to catastrophic failure potentially causing explosion, fire and vaporisation of materials with attendant toxicity hazard.

If it becomes necessary to increase the load capacity of a network locally (housing or industrial development) this is accomplished by adding transformers or local generation leading inevitably to a reduction of the source impedance and an increase in the magnitude of the fault current (fault level). Enhancements of upstream network capacity or interconnection to increase plant redundancy can also cause the fault level to rise. If the increase in fault level is sufficient to risk exceeding safe levels for the network infrastructure, means to limit the fault current are required.

## 2 Fault current limiting

Fault-current limiting has traditionally been accomplished by raising the network source impedance, either by splitting circuits which are normally connected in parallel, or by inserting fixed impedances, usually primarily inductive in nature, into an electricity supply circuit, to restrict the magnitude of the current which flows if a short-circuit occurs. Series reactors or high-impedance transformers usually provide the inserted impedance.

This approach has the desirable effect of reducing the fault current to a safe level so that switchgear and other network equipment remain within their operational capacities i.e. short-circuit ratings are not exceeded. It also has the undesirable effect of increasing locally the network's source impedance, reducing the voltage stability (power quality) as the load current magnitude varies.

Solutions providing the fault limiting functionality whilst maintaining a low source impedance in the absence of a fault can be provided by emerging technologies. The availability of lower cost, higher temperature superconducting materials has been an enabling factor in the development of these technologies. Devices having these characteristics are known as fault current limiters (FCLs).

A fault current limiter must be able to change impedance autonomously, without active sensing or actuation systems which might be prone to failure. This is because FCLs are installed in series connection with other network components which have limited abilities to withstand the passage of fault-current, or in the case of switchgear, maximum fault making and breaking capacities. The impedance change must also occur rapidly, before the first peak of the fault current, so that fault making capacities are not exceeded.

## 3 FCL Types

### 3.1 Non-autonomous FCL technologies

It is possible to break an electric circuit, equivalent to inserting an infinite impedance, by embedding an explosive charge inside a locally weakened conductor and detonating the charge electrically if the fault current rises above a safe level, or if the rate-of-rise of the fault current indicates a subsequent excessive magnitude. The conductor is ruptured and the arc is extinguished by the blast. Devices using this approach have been available for a number of years from manufacturers in Europe and the USA, but they rely on measurement, decision-making and actuation systems which are deemed to be failure-prone by some authorities and any failure leaves a low impedance in circuit so the fault remains unlimited.

Power-electronic based FCLs have also been proposed; again these require active actuation systems, the failure of which would most likely result in the fault remaining unlimited.

### 3.2 Autonomous FCL technologies

There are currently two main approaches to providing autonomous FCL functionality whereby the impedance inserted is either primarily resistive or primarily inductive.

#### 3.2.1 Resistive Limiters

In a resistive limiter, load current supplying power to customers is passed through a conductor which becomes more resistive if the current exceeds a certain level. In current practice, this conductor comprises a length of superconducting material, maintained at a temperature below the critical temperature of the material. The superconductor is dimensioned to revert to a normal conducting state (quench) if the current exceeds a certain level. A series circuit-breaker operated by a rapid and reliable local protection system is required to interrupt the fault current through the FCL to protect the quenched superconducting circuit from overheating and to allow the superconductor to cool to below its critical temperature so that the series circuit-breaker can be re-closed, reconnecting the FCL. Cooling down may require a few minutes and to maintain the continuity of power distribution during the temperature recovery operation, conventional reactors may be connected in parallel with the FCL and its series circuit-breaker. Where high-temperature superconducting (HTS) material is used (typically Bi2212, Bi2223 or YBCO, all of which have critical temperatures of around 90K), cooling may be achieved by immersing the HTS circuit in liquid nitrogen. Today YBCO tapes having a high resistance in the normal state are used in state-of-the-art resistive FCLs. Any failure of the cooling system results in the FCL shifting to a high-impedance state, so the approach is inherently fail-safe.

#### 3.2.2 Inductive Limiters

In an inductive FCL, the fault limiting impedance takes the form of inductive reactance which can be inserted into the load current path in a number of ways, including using a resistive limiter connected in parallel with a conventional series reactor.
Another approach is to provide iron-cored reactors where the cores are driven into saturation by an applied magnetic field. Under normal





conditions, the cores remain saturated, but are driven out of saturation during a fault. In the implementation described here, two reactors are connected in series. During a fault, one of the reactor cores is driven out of saturation during each positive half-cycle of the fault current and the other during each negative half-cycle. This approach is illustrated in Fig. 1.

The saturating flux is produced by the dc solenoids (blue) and the load current passes through the ac coils (orange). The iron cores remain saturated whilst the ac coils carry load current (green). When a fault occurs, the fault-current (red) in the ac coils drives one of the cores out of saturation (coloured grey) during each half-cycle, causing the inductive reactance of the ac coil on the de-saturated core, to rise. The inductive reactance of a coil with a saturated core is rather low and when the core is de-saturated, the reactance rises by a large factor – in the case discussed here, it is around 6 times. This rise provides the current limiting functionality.

There is a perceived benefit of this approach in that series reactors, both air and iron-cored, have been used for many years and standards covering their design and qualification exist already.

The "closed-core" arrangement of Fig. 1 was developed initially in the 1960s at IRD in Newcastle (UK) by messrs. Raju, Parton and Bartram using low-temperature superconducting solenoids (frequently referred to as magnets) to provide the saturating flux.

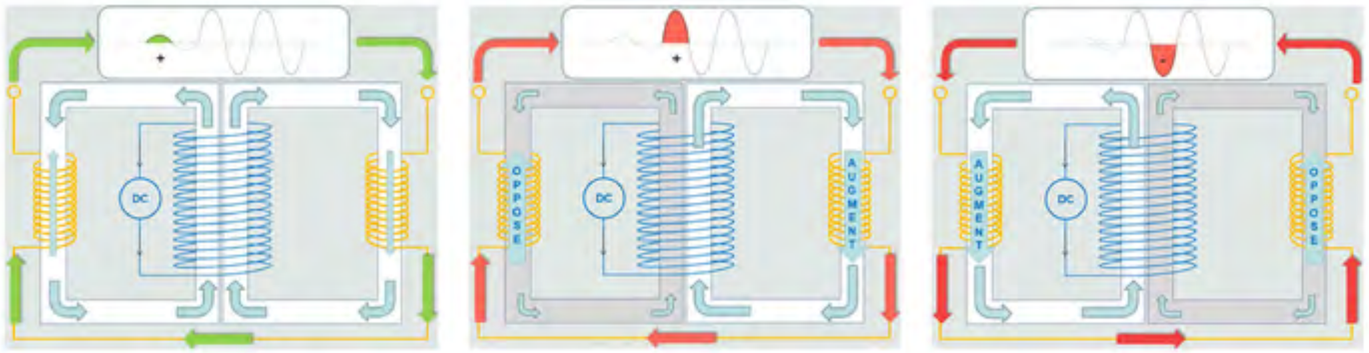

**Figure 1** Closed-core arrangement (left) under load current (centre & right) during a fault

The saturating solenoid is required to provide a high flux-density and to keep the size, mass and power requirements within practicable limits, superconducting tape or wire may be used. In a three-phase limiter, it is possible to use a single solenoid to saturate the cores of the six ac coils.

The ASG limiter has an "open-core" architecture and magnesium diboride wire has been used for the solenoids (magnets) which provide the saturating flux. The operating principle is identical to that of the closed-core arrangement. Any failure of the magnet cooling system or the magnet dc power supply results in the FCL shifting to a high-impedance state, so this approach is inherently fail-safe.

## 4 ASG FCL Design

The open-core arrangement is shown schematically in Fig. 2. The ac coils are wound onto straight triangular section core posts which are enclosed in an oil-filled stainless-steel tank.

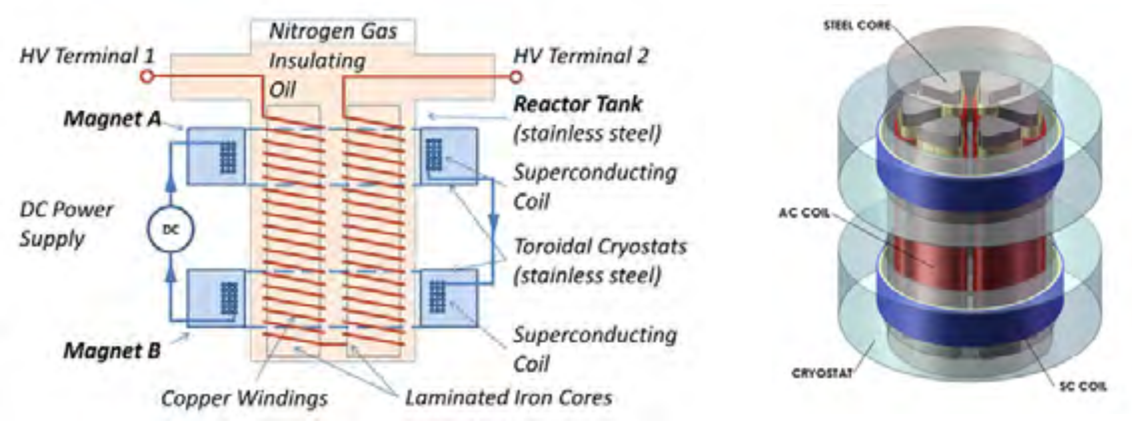


**Figure 2** Closed-core arrangement (left) under load current (centre & right) during a fault





The open-core arrangement has a number of advantages. The oil-filled tank can be fitted with radiators to provide ONAN or assisted cooling of the oil which provides electrical insulation facilitating up-scaling of the voltage rating to transmission-voltage levels. The installation of the superconducting magnets outside the oil tank allows access to the magnets for maintenance even while the FCL is operating. A 3-year trial of a limiter rated 11 kV; 1250 A using this technology was undertaken in 2012-2015 in northern England, during which at least 9 significant network faults occurred and were limited effectively by the device.

### 4.1 36kV; 800A FCL Development

The 11kV FCL mentioned previously was equipped with superconducting magnets manufactured using high-temperature superconducting (HTS) tape made from Bi2223. In response to a request for a 36 kV rated device, it was decided to investigate the possibility of using $MgB_2$ wire to reduce the cost of the magnets which would need to be much larger physically, both to accommodate the larger diameter oil tank and to provide the considerably higher saturating flux density needed to achieve the required current limiting capability of 40% - which is to say that the limiter would reduce the fault current magnitude by 40%.

#### 4.1.1 Selection of superconducting material for the DC coils

The selection of the superconducting material impacts the DC coil design and cost. Today three superconducting materials are available in sufficient quantity with high enough performance to be considered for power devices. Their main characteristics and costs are reported in Table 1. The first two are high-temperature superconducting (HTS) tapes made from Bi2223 and YBCO and are both commercially available. They are cooled using subcooled liquid nitrogen (65K), a cheap, abundant, and environmentally friendly fluid, which makes HTS tape an attractive solution for many superconducting devices. Their performance in magnetic field increases at lower temperatures. However, their costs remain high. Despite an industrialised process based on powder-in-tube (PIT) technology, Bi2223 tape requires a bulk silver matrix that represents more than 50% of the tape cross-section, which is costly. For YBCO tapes, the production processes remain costly and complex and result in low yields.

## Table 1. Main characteristics of superconducting wires and tapes

| | Shape | Width | Thickness | Performance of commercial tapes and wires | | |
|---|---|---|---|---|---|---|
| Bi2223 | Laminated powder-in-tube (PIT) tapes | 4.5 mm | 3-0.5 mm | $I_c$ @70 K, 0.5 T 350-400 $A.cm^{-1}$ | Length < 1500 m | 80-120 €/kA/m |
| YBCO | | 4-12 mm | | $I_c$ @70 K, 0.5 T 500-800 $A.cm^{-1}$ | Length < 500 m | |
| $MgB_2$ | Laminated PIT tapes | 4-8 mm | 0.5-0.7 mm | $I_c$ @20 K, 1T 300 -400 $A.mm^{-2}$ | Length < 3000 m | 3-5 €/kA/m |
| | Cylindrical PIT wires | Ø 0.8 -1.5 mm | | | | |

The third material is magnesium diboride ($MgB_2$) available in round wires or tapes. These benefit from the high-yield and low-cost PIT process. Multiple $MgB_2$ fibres, typically in a nickel matrix, are drawn to form the wire or tape.

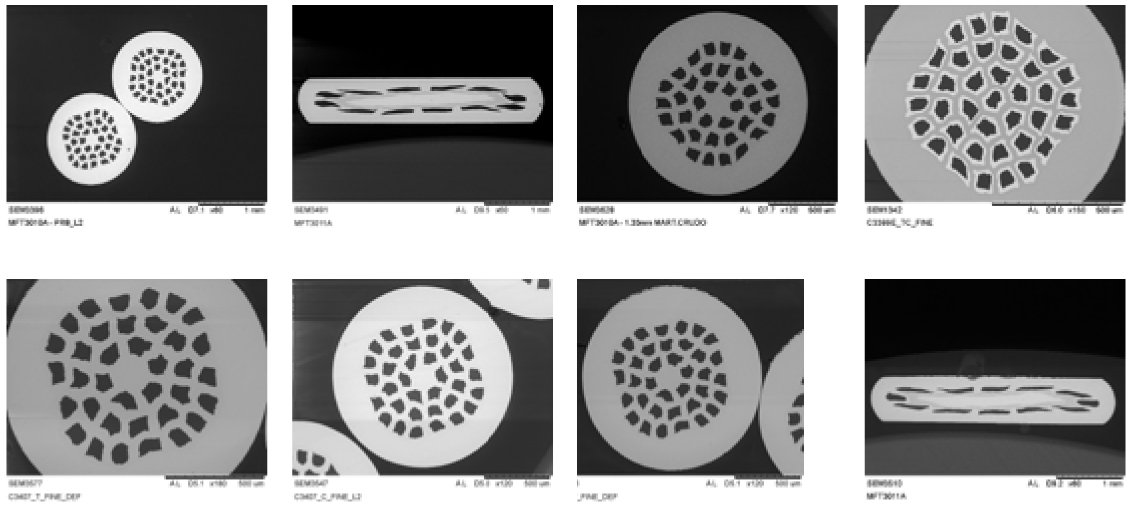

**Figure 3** Cross section of multifilamentary $MgB_2$ tapes and wires ($MgB_2$ filaments in black)

Magnesium diboride wires and tapes (Fig. 3) are available in long lengths and their cost is comparatively low, as indicated in Table 1. However, to be superconducting, this material must be kept below around 25 K requiring more sophisticated cooling systems than providing liquid N2. Consequently, the cost of the cooling system increases and its efficiency decreases. However, a DC superconducting magnet required for a saturated core inductive FCL can be designed with low cryogenic losses and with a cryogen-free cooling system. Based on this technology, the investment required for operation in the range 15-25K remains still affordable. This extra cost in comparison with HTS cooled in liquid N2 was found to be counterbalanced by the low cost of $MgB_2$ tapes especially when considering large FCL systems.

### 4.1.2 $MgB_2$ Magnets

The 36kV saturated core FCL comprises 6 (2 per phase) iron-cored reactors in which the iron cores are driven into saturation by the magnetic field produced by two superconducting magnets, arranged as a Helmholtz pair. The magnets comprise 3816 turns of multi-filament magnesium diboride wire arranged in 30 layers on a stainless-steel former, with a winding height of 410 mm and an internal diameter of 1.8 m. Each magnet contains about 23 km of $MgB_2$ wire.

The wire has been optimised for this application to allow small operation of the FCL up to a temperature of 28K.

The magnets have been designed to withstand the not insignificant mechanical and electrical stresses associated with this application. The two coils are connected to the power supply as shown in figure. In normal condition the two coils will operate in series. However when a fault occours the AC windings will induce a not neglible current on the superconducting magnets, this effect is limited by a copper shield.

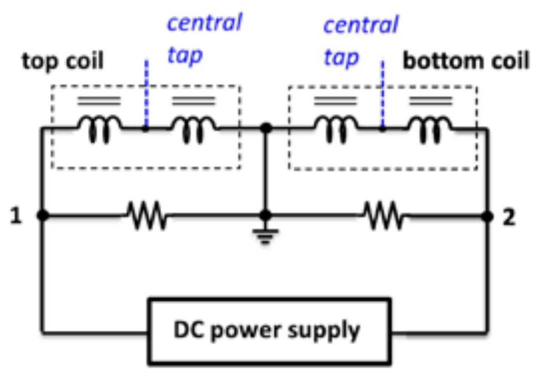

These conditions lead to the generation of a great force along the axis of the superconducting magnet; in the radial direction the force is more contained.

A voltage tap is made available from the middle of each of the two coils for quench detection purposes. A dump resistor is connected to each of the two coils in order to allow fast discharge during possible quench.
A quench analysis has been carried out in order verify if maximum temperature and voltages during quench meet the standard design criteria.
The total charging time, starting from zero current up to the nominal value In, is less than 30 minutes.
The main design parameters of the $MgB_2$ windings are shown in table:

| Parameter | Value | U.M. |
|---|---|---|
| Total length of conductor (one coil) | 22.1 | km |
| Inner radius of the cryostat | 841 | mm |
| Outer radius of the cryostat | 1097 | mm |
| Height of the cryostat | 785 | mm |

The superconducting magnets need to be cooled to below 20 Kelvin and this is accomplished by conduction of heat through copper components in contact with the epoxy-encapsulated magnesium diboride coils.
The magnets are cryogen-free and vacuum insulated. Heat is extracted from the copper cooling structure by means of Gifford-McMahon coldheads. The coldheads are supplied with high-pressure helium and contain a reciprocating mechanism which repeatedly lowers the pressure, removing heat. There is redundancy in this setup; three coldheads are sufficient to provide the required cooling for each magnet. The eight helium compressors are water-cooled by means of four chillers. The whole cooling system runs from a 400 volt 3-phase supply and consumes 80-100 kilowatts.





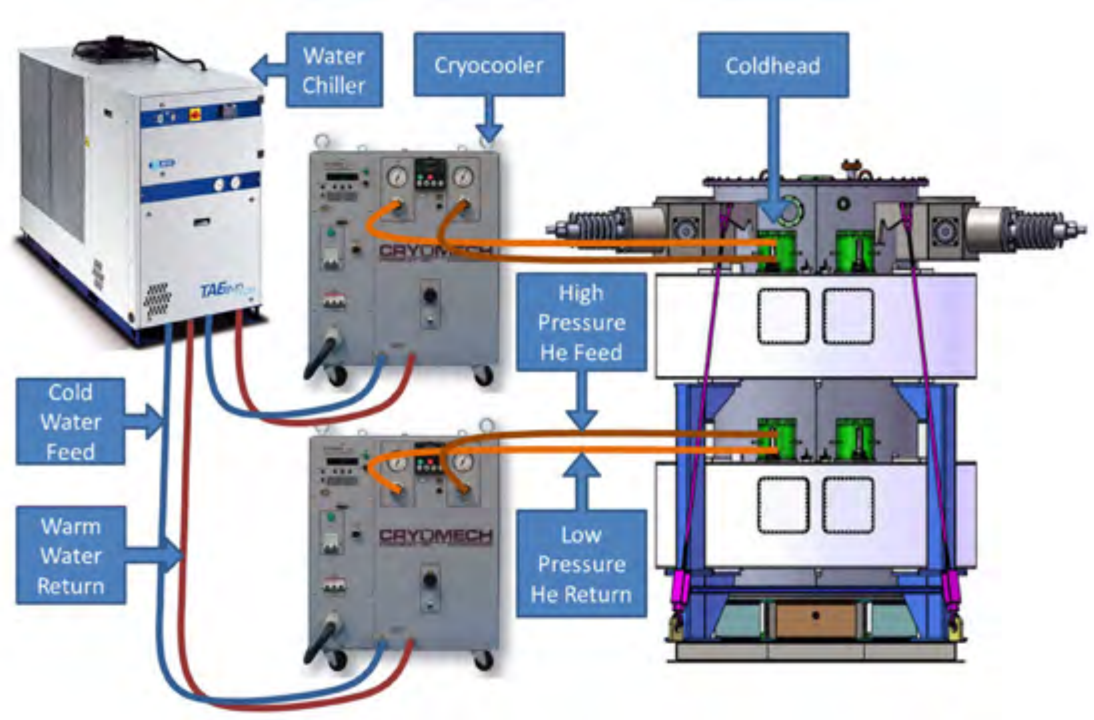


**Figure 4** Schematic layout of the FCL magnets cooling system

Each chiller is used to cool two helium compressors (see Fig. 4), each of which removes heat from a coldhead, one on the lower magnet and the other on the upper. This allows one chiller to be out of service, whilst maintaining three active coldheads on each magnet, which are able to provide sufficient cooling.

## 5 FCL Deployment and Operation

### 5.1 FCL Layout at site

The arrangement of the two magnets and the reactor tank, cores and coils is as shown in Fig. 2. The general arrangement of the magnets, reactor tank & radiators is shown in Fig. 5. The assembly is about 3.7 m high and weighs 36 tonnes.

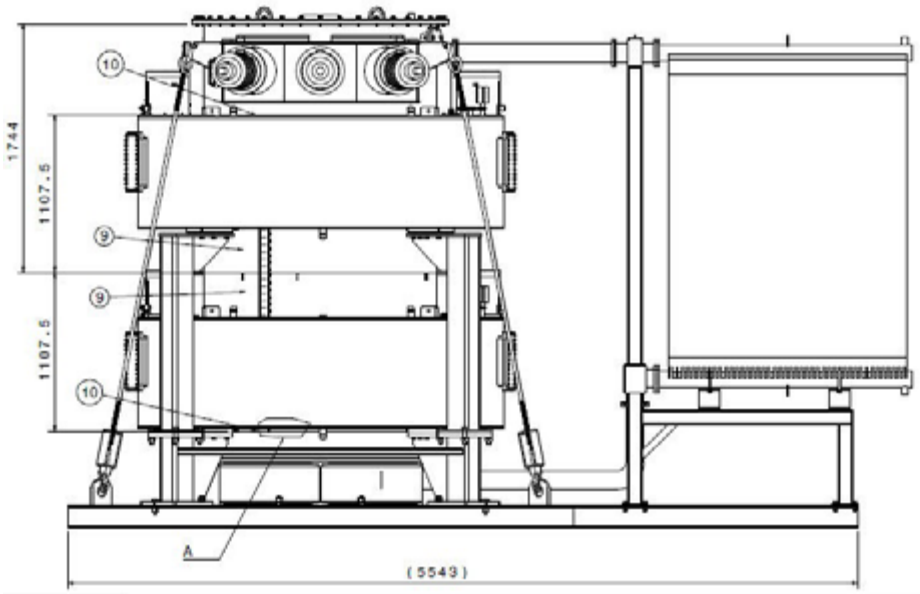


**Figure 5** General Arrangement of 36kV FCL Reactor tank, radiators & SC magnets

Fig. 6 shows a typical site layout. The FCL main assembly of the reactor tank, radiators and magnets is installed on a concrete plinth in an oil bund. The two 6-metre containers are mounted side-by-side on a second plinth, close to the main assembly.

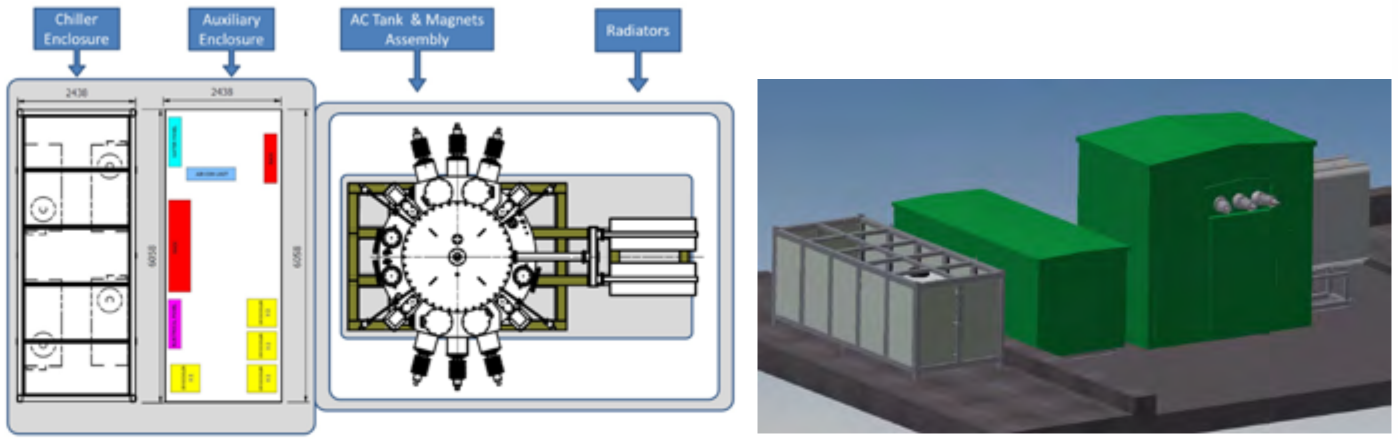


**Figure 6** GTypical layout of the three FCL enclosures





The left-hand enclosure, which is fitted with mesh floor and ceiling, contains water chillers to dump the heat, removed from the magnets by the cooling system, into the atmosphere. The right-hand (labelled "auxiliary" in Figs. 6 & 7) enclosure contains the helium compressors, each of which is connected to a chiller by a pair of water pipes. Each helium compressor is connected to a coldhead on one of the two superconducting magnets by means of a pair of vacuum-insulated helium pipes. The auxiliary enclosure also contains the PLC and SCADA systems which provide the control and HMI functions, an uninterruptible power supply for backup and three aircon units for controlling the humidity in the enclosure. Fig. 7 shows the actual components of the FCL in the Genoa factory.

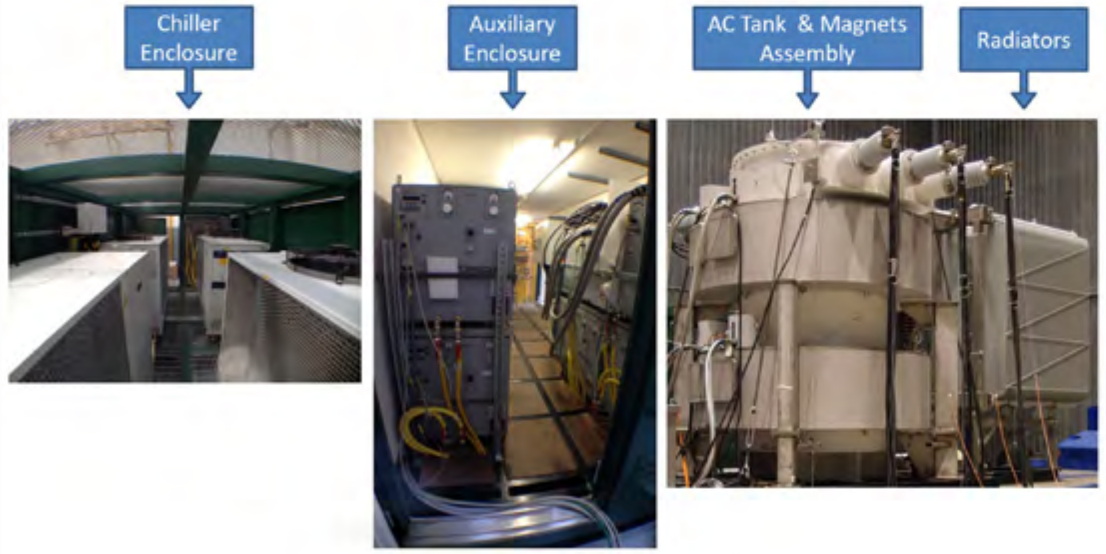


**Figure 6** L-R Chiller Enclosure, Auxiliary Enclosure & Reactor Tank/Magnets/Radiators Assy

### 5.2 Control System and SCADA

A sophisticated control system, developed over the course of several FCL projects, autonomously looks after the operation of the cooling systems, providing alarms via SMS messaging and allowing remote interrogation/control via 3G modems. The FCL control system is shown schematically in Fig. 8.

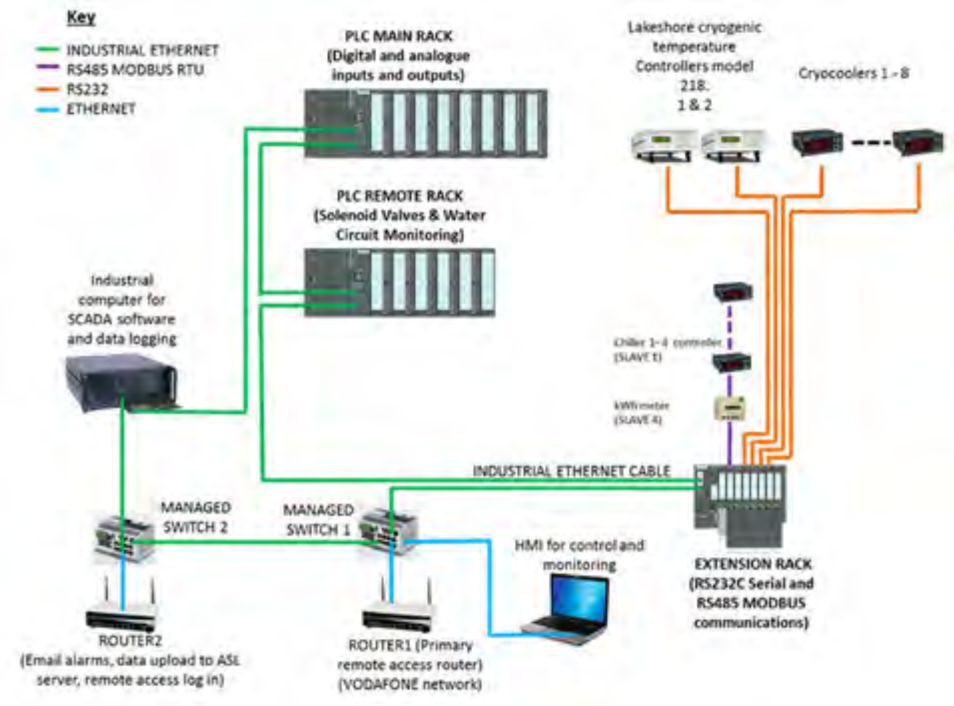


**Figure 8** FCL control & SCADA systems

The SCADA system is accessed locally by means of two industrial PCs in the auxiliary enclosure and can be accessed remotely via the internet. The main cooling system screen (Fig. 9) displays the temperatures and flow rates of the cooling water and the oil temperatures in the helium compressors. Further screens display details about the chillers, compressors, superconducting magnet internal temperatures, the external environment, etc.

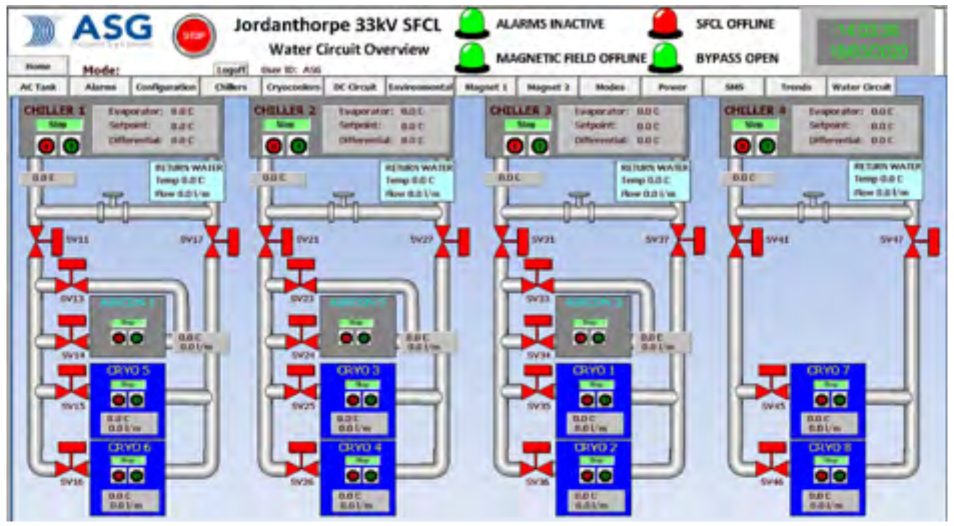


**Figure 9** Cooling water system SCADA screen





### 5.3 Connection into Network

A number of FCL demonstration/trial projects have been carried out successfully in the UK between 2009 and 2015 during which both resistive and saturated-core limiters were installed in distribution network substations. Fig. 10 shows two examples of how the FCLs were connected into the networks.

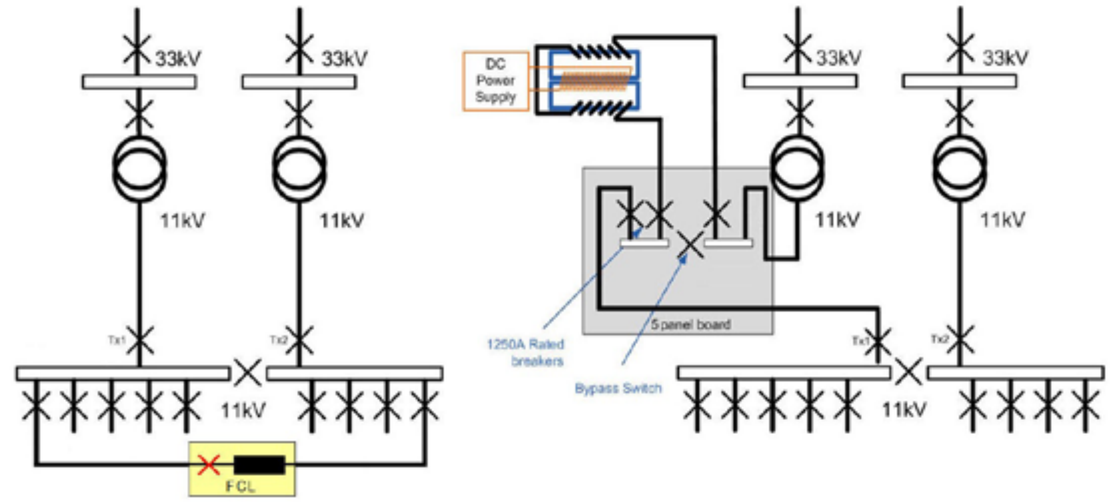


**Figure 10** Bus-section (left) and transformer tail (right) FCL deployments

FCLs in the UK trials were connected either as a bus-section connector (left), or in a transformer tail (right). The SFCLs were both added because the upstream (33kV) fault level had increased. Similar deployments may be used when a transformer is upgraded or a new transformer is added to an existing busbar, in all cases allowing the busbars to remain interconnected, maintaining the plant redundancy level. If a 33kV supply is lost, the other transformer must supply all of the load current. In the bus-section deployment, the SFCL only has to carry the load current to the other busbar, allowing a lower rated SFCL to be used. In the transformer tail deployment, which is simpler to implement as existing switchgear does not need to be modified, the SFCL must carry all of the load current if the Tx2 supply is lost, but it can be bypassed because the fault level is now ~ ½ of the previous level. For this reason, FCLs intended for transformer tail connection are designed to have a short-time overcurrent capacity to provide time during which the bypassing can be implemented. In the case of the 36kV FCL which is central to this article, the continuous current rating is 800A and the short-time rating is 1400A for 15minutes.

## 6 Performance and Testing

### 6.1 Thermal Testing

Fig. 11 shows the FCL assembly comprising the two superconducting magnets, reactor tank and radiators for cooling the reactor tank oil, undergoing thermal testing at 800A continuous current, during which the oil temperature rise remained below the limit of 60 K.

**Figure 11** FCL during Thermal Test at IPH, Berlin

### 6.2 Short-circuit performance

In order to investigate the performance of the FCL and its interaction with the power grid a numerical model of the device was developed and coupled with the circuit model of the power network. The model was developed for ASG at the University of Bologna. Results from the model were compared with the results of full-scale short-circuit tests with a prospective symmetrical rms fault level of 8kA and an initial peak of 21kA. The limiter reduced the fault current to 5kA rms symmetrical and 14kA peak – the calculated and measured results are shown in Fig. 12.

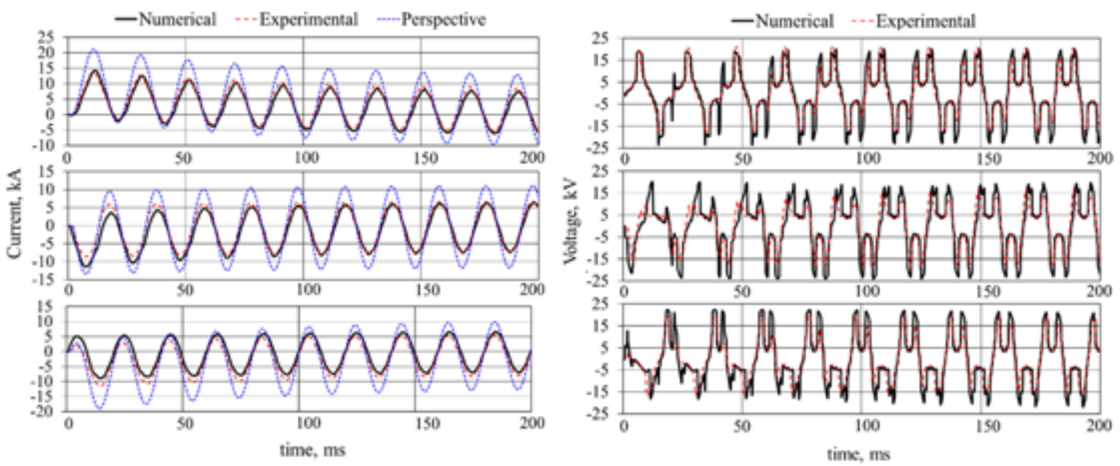


**Figure 12** Results of short-circuit tests showing prospective and limited (measured and calculated) currents (left) and (measured and calculated) voltage drops across the device (right)





These results show that the FCL performs according to its specification and that the model is able to reproduce the measured data from full-scale test results. Additionally, the model is sufficiently general in nature to allow variations on the FCL design to be evaluated and therefore the modelling methodology is applicable to a wide range of FCL designs.

## 7 Conclusions

Magnesium diboride wire, optimised for this application by the Columbus division of ASG Superconductors has been incorporated into dry-cooled superconducting magnet assemblies by ASG in Genoa. The magnets have been shown to effectively saturate the cores of a 36kV; 800A FCL and to withstand repeated fault currents without problems, including a fault of 3 seconds duration. The required performance of the FCL was achieved.

Plans for installation of the device have been delayed by the COVID19 epidemic – it is hoped that when some service experience has been gained, a further article will be published. The open-core architecture applied here at 36kV uses well-established design and manufacturing principles (developed over many years in transformers) and can readily be upscaled to accommodate higher voltages and currents. ASG Power Systems is able to offer FCLs for distribution and transmission applications.

# HI-LUMI D2 DIPOLE

MBRDP1 – Prototype





# HI-LUMI: THE SUPERCONDUCTING D2 DIPOLE PROTOTYPE

Nicolò Valle

The Large Hadron Collider (LHC) at CERN accelerates and collides beams of particles of various masses from single protons up to lead nucleii. It is installed in a 27 km circumference tunnel, about 100 m underground.

The High Luminosity LHC (HL-LHC) is exploring new beam configurations and the use of new advanced technologies in the domain of superconductivity.

In the HL-LHC an important role is played by the dipoles recombining and separating the particle of the two proton beams around the interaction regions.

ASG Superconductors is involved with INFN in the design and construction from the beginning of the project.

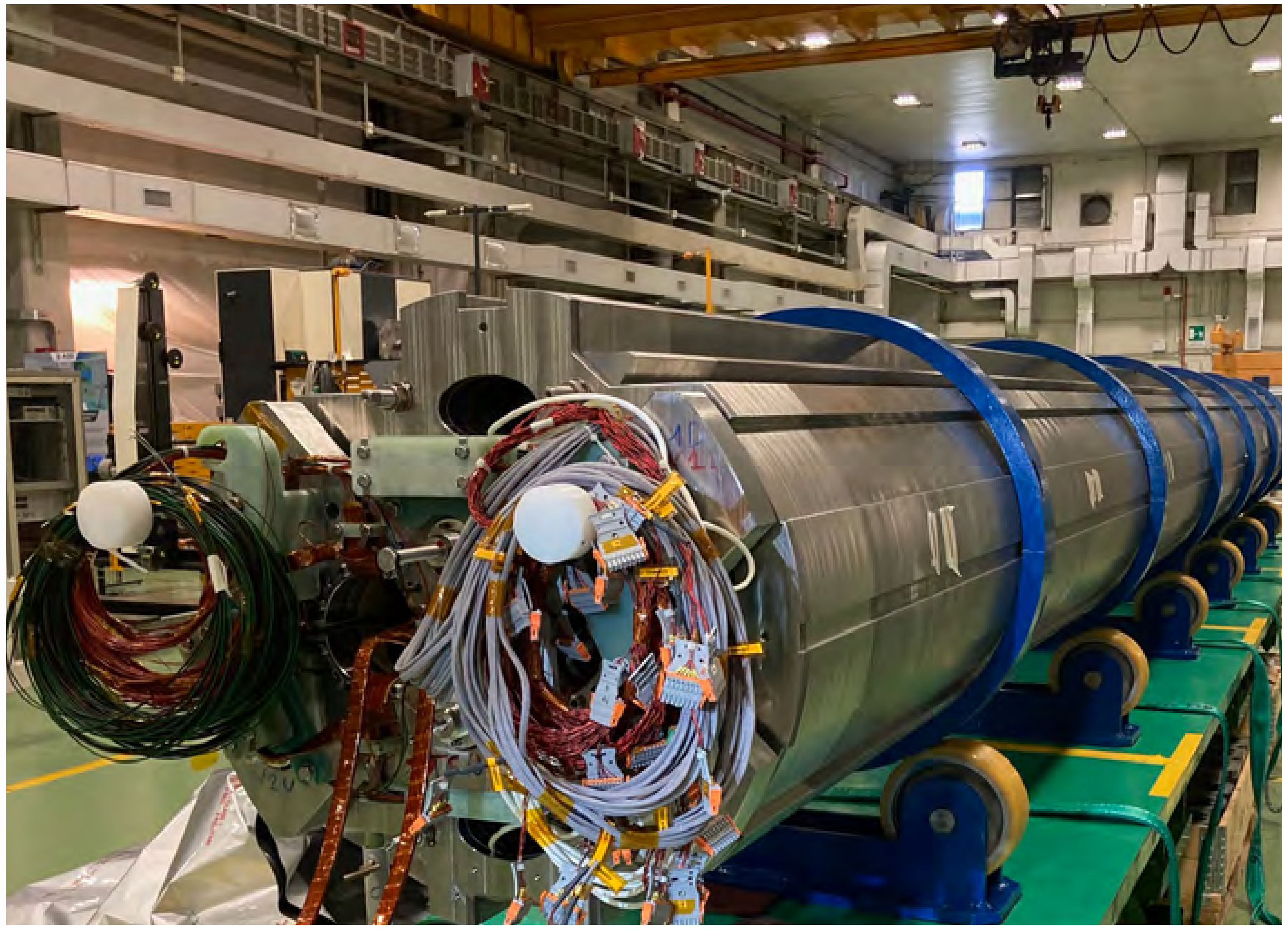

The High Luminosity LHC (HL-LHC) is a project aiming to upgrade the LHC collider after 2026 in order to maintain scientific progress and exploit its full capacity. The LHC is the most recent and powerful accelerator constructed on the CERN site. The LHC machine accelerates and collides proton beams but also heavier ions up to lead. It is installed in a 27 km circumference tunnel, about 100m underground. The LHC design is based on superconductive twin-aperture magnets which operate in superfluid helium at 1.9K (-271°C). By increasing its peak luminosity by a factor of five over the nominal value, it will be able to reach a higher level of integrated luminosity, nearly ten times the initial LHC design target. To this aim, HL-LHC is exploring new beam configurations and new advanced technologies in the domains of superconductivity, cryogenics, radiation hard materials, electronics and remote handling.

The project also requires a new technical structure with a cavern and a 300m long tunnel along the insertion region of IP1 (ATLAS) and IP5 (CMS). The cold-masses of these two magnets (ATLAS and CMS) have been realized by ASG Superconductors in Genoa as well as 450 (one third) of the LHC cold masses. The project began in 2011 as the European Commission FP7 Design study called "HiLumi LHC" and the main installation in the LHC tunnel will take place during the Long Shutdown 3 (LS3) in 2024-2026.

CERN and INFN (Italian Institute for Nuclear Physics) are developing a collaboration activity for HL-LHC for the procurement of models, prototypes and magnets. In the frame of the first Contract, ASG realized the MBRDP1 Short Model during 2019 that has been successfully tested at 1,9K at the CERN Lab during 2020. At present (October 2021) the Prototype Full Scale Magnet has been completed and delivered to CERN and the construction phase of six series magnets awarded to ASG in 2020 has been started.

**The Magnet**

In the HL-LHC an important role is played by the dipoles recombining and separating the particles of the two proton beams around the interaction regions. In particular the MBRDP1 realized by ASG is an 8 meters long twin aperture (Φ 105 mm) magnet with a separation between apertures at 1,9K of 188 mm, generating in both apertures an integrated magnetic dipolar field of 35 Tm with the same polarity. The cross-section of the dipole, which contains all the components cooled by superfluid helium, is shown below. Each dipole consists of the so-called active part, made of two coils with 105 mm diameter apertures in a mechanical structure of stainless steel collars and an aluminium sleeve, with an outer magnetic steel structure (the iron yoke). The dipole cold mass has a quasi-elliptic cross section with an overall length of 8010 mm, a maximum diameter of 614 mm and an overall weight of 14,2 tons.

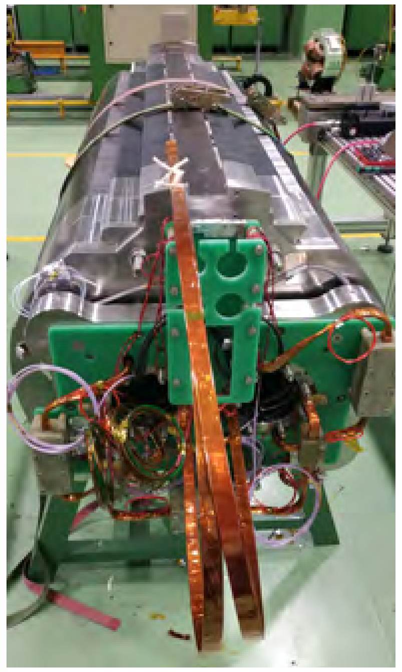

**Figure 2** MBRDP1 – Short Model.

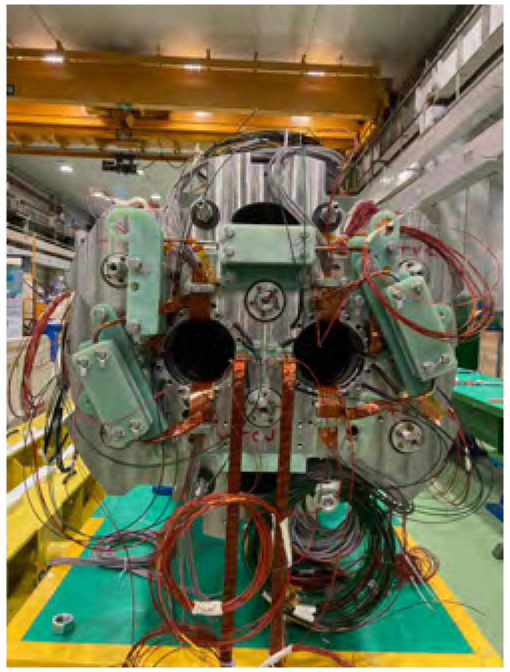

**Figure 3** MBRDP1 – Detail of the LC Side Head.

Here below are reported the MBRDP1 – Prototype main parameters:

| MBRDP1 Prototype Main Parameters | Unit | Value |
|---|---|---|
| Aperture diameter | mm | 105 |
| Number of apertures per magnet | No. | 2 |
| Distance between the two apertures (cold/warm) | mm | 188,0/188,7 |
| Cold mass outer diameter (min/max of the iron yoke) | mm | 550/614 |
| Coil Length | mm | 8010 |
| Magnetic length | mm | 7778 |
| Bore Field | T | 4,5 |
| Peak Field | T | 5,2 |
| Operating Current | kA | 12,340 |
| Operating Temperature | K | 1,9 |
| Overall current density | A/mm2 | 478 |
| Stored Energy | MJ | 220 |
| Superconductor Type | - | NbTi Rutherford |
| Strand Diameter | mm | 0,825 |
| Number of strands per cable | No. | 36 |
| Coil Turns | No. | 31 |
| Cold-mass overall weight | Tons | 14,2 |






**Figure 4** D2 dipole ready for shipment in ASG premises.

For High Luminosity LHC, the future configuration of the Large Hadron Collider at CERN several new magnets are needed to have the proper acceptance to cope with the high intensity beams emittances.
The recombination dipoles (D2) are one of the magnet that will be replaced. ASG is involved with INFN in the design and construction from the beginning of the project.

Many thanks to INFN and all our colleagues at ASG for this important achievement. This milestone is a further step towards the accomplishment of CERN's HI-Lumi LHC project, whereas our magnets are a testimony to the ASG's legacy of partnership and service to the needs of the research Institutions. A legacy that has proven conducive, in the past, to have contributed to reaching important scientific goals, like – for example – the discovery of the Higgs Boson in 2012.

# SEA-TITAN WAVE ENERGY

# SEA-TITAN: A FIRST STEP TOWARDS THE SUPERCONDUCTING WAVE ENERGY PRODUCTION

Martina Neri

By 2050 the 10% of Europe's electricity demand would be produced by ocean energy (100 GW of ocean energy capacity – 350 TWh of electricity).

The ocean energy is based on the use of Wave Energy Converters which produce energy from waves. The core of a WEC is the power Take-Off, which transforms mechanical movements into electrical energy.

Superconductivity can help to meet the energetic goals enhancing the power generated by electrical machines without increasing volumes.
The best choice is to work with a high temperature superconductor as $MgB_2$: thanks to the stability and the relative high Tc of the material , maintenance costs and efforts could be significantly reduced.

www.seatitan.eu

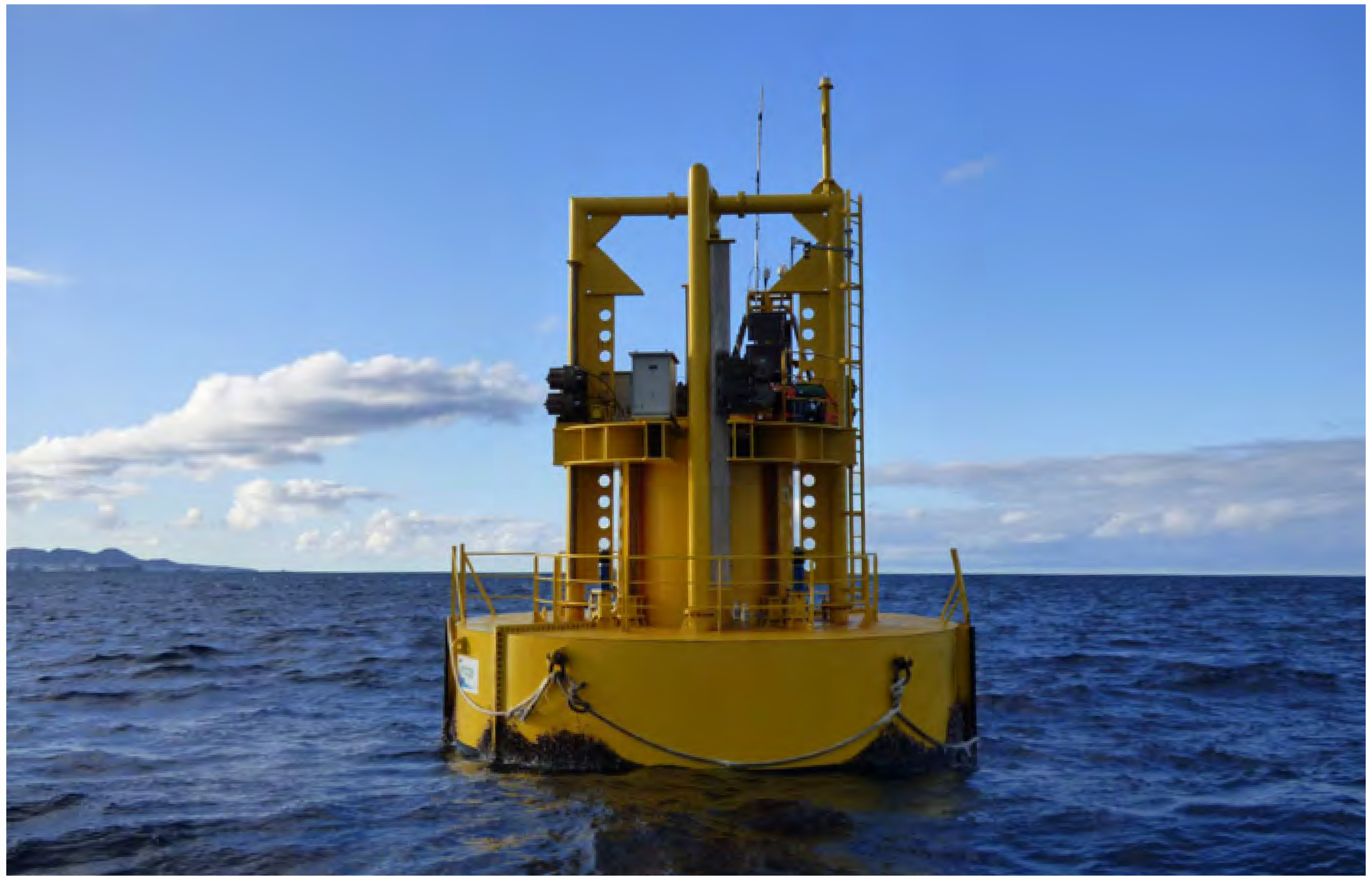

## Introduction

Europe's 2050 Energy Strategy has established a target to reduce greenhouse gas emissions by 80%-95% compared to 1990 levels and renewable energy accounting for at least 64% and up to 97% of the electricity consumed.
In particular, ocean energy could sustain up to 10% of Europe's demand by 2050. The Ocean Energy Strategic Roadmap has estimated that 100GW of ocean energy could be deployed in Europe by 2050, producing around 350TWh of electricity.
Superconductivity can help to meet the energetic goals enhancing the power generated by electrical machines without increasing volumes. Nowadays different alternatives to develop superconducting machines have been proposed, basically in the sector of wind energy, where several rotary generators have been developed in order, basically, to alleviate the weight and to increase the efficiency.
Two critical points can get difficult the realization of a superconducting machine: how to keep cold the coils (temperature lower than 50 K) and how to reduce ac losses.
The first problem can be solved considering a switched reluctance machine: this machine requests coils in only one side, the stationary one. This fact simplifies enormously the design of the machine.
Ac losses are a wasted power that is generated in a superconductor when it is in a magnetic field varying in time. These losses produce heat that must be extracted increasing the complexity of the facility. Since they depend on the field variation with the time, they are very sensitive to the frequency. This fact implies that for standard commercial frequencies (50 Hz), ac losses are simply inadmissible with the present status of the technology. For this reason, most of the superconducting electrical machines use superconductivity only on the dc side. Nevertheless, the interest of finding solutions for using superconductivity also in the ac side of the machine is increasing, since it would represent a big reduction in the sizes and efficiency of the machine.
Implementing a superconductive solution in the ocean energy conversion process is one of the goals of the SeaTitan project. In particular, it had the purpose to study the possibility to implement a superconducting linear machine that could work in ac.
The project, born in 2018, has received funding from the European union's Horizon 2020 research and innovation programme and brings together 11 partners from 7 European countries.
Thanks to its expertise, ASG was involved in this project; in particular in the definition of the wire and in the estimation of ac losses.





## Power Take-Off: the core of the ocean energy conversion

The ocean energy is based on the use of Wave Energy Converters (WECs) which produce electricity from waves. The core of a WEC is the Power Take Off (PTO), which transforms the mechanical movement of the waves in electrical energy.
Several configurations of PTO exixts, the SeaTitan project focused its work on the so-called Direct-Drive System.
All the Direct-Drive machines are based on a Translator/Stator configuration that balances transverse forces.
The force in ocean energy is given by waves. In order to maximize the energy production, the system must work close to the resonance.
In this configuration, the Stroke, the maximum amplitude of the translator motion, can be high even if the waves are small.

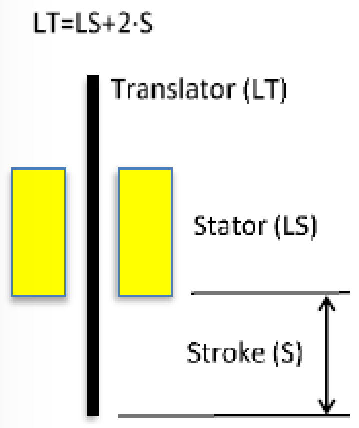


**Figure 1** Direct-Drive machine scheme.

Any electrical machine is defined by the Shear Stress, the force produced by unit surface of its airgap. This parameter is proportional to the product of the electric load of the machine (expressed in kA/m) times the magnetic load of the machine (expressed in Tesla).
In general, this magnetic field can be generated by permanent magnets or coils. In marine applications, permanent magnets are not appropriate because they are very delicate components, prone to corrosion. In this case the coils can be resistive or superconducting.
The core of the Sea-Titan project is to develop a new PTO. One way to achieve this goal is based on using superconducting coils.
In particular, the Sea-Titan project tried to convert a resistive PTO, based on a Switched Reluctance Machine (SRM), in a superconducting one.
In this kind of electrical machine there are an Active side (coils generating the magnetic field) and a Passive side (iron); only one of the side is moving.

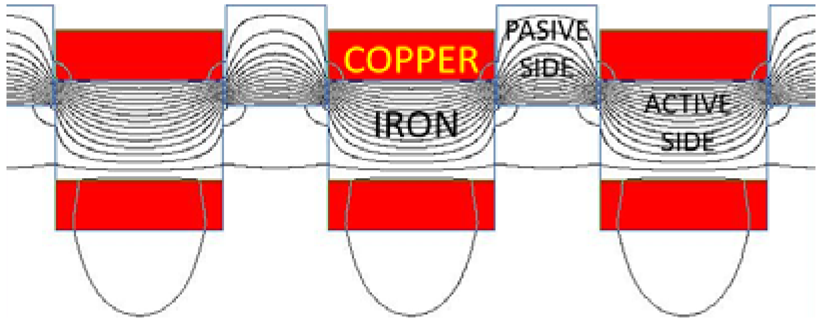


**Figure 2** A Switched Reluctance Machine has an Active side (copper and iron pole) and a Passive side (iron) moving one respect of the other.

While in the resitive configuration the moving side is the Active one, in the superconducting study the coils are designed to be fixed and the iron is moving. In this way the problem related to the cooling of a moving component is solved. As previously reported, to enhance the efficiency of an electrical machine it is necessary to increase the product between the current and the magnetic field density.
In a non-superconducting coil, there is a strict limit to the current that the coil can transport but in a superconducting one that limit is much higher and this means that very big currents can be transported in small volumes. The difference between a non-superconducting machine and a superconducting one, both with iron in their magnetic circuit, is that although they work at similar magnetic flux density levels (little bigger for the superconducting one), this small variation in the field (in the range of 10% to 20%) implies a tremendous variation of the current and consequently on the force.

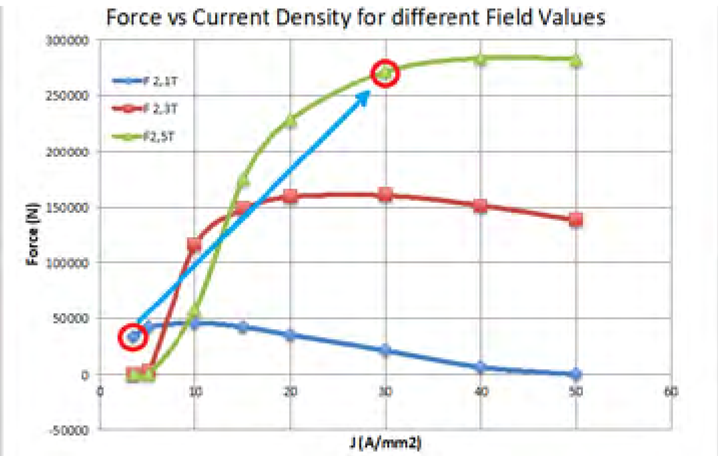


**Figure 3** Force vs Current Density for 3 values of B. For a normal conductor, working above 3-4 A/mm$^2$ is not possible (the best option is the blue curve). For a superconducting machine it is possible to achieve 30 A/mm$^2$, jumping to the green curve.





## A superconducting PTO: the wire definition

Since the goal of this kind of machines is to generate power, it is basic to reduce the power necessary to keep cold the system. In order to reach this goal, the best choice is to work with a high temperature superconductor as $MgB_2$.
Magnesium diboride, $MgB_2$, has been regarded as a very promising candidate for alternatively commercial superconducting materials since the discovery of its superconductive properties in 2001. Together with its simple crystalline structure and low material cost, the transition temperature around 40 K enabling a cryogen-free operation is definitely attractive for engineering applications allowing to drastically decrease capex and opex with respect to superconductors which need liquid refrigeration fluids.
Superconducting PTOs and, in general, superconducting machines as well as cables for current transport represent ideal application for this material, thanks to their relatively low operational magnetic field. Moreover, thanks to the stability and the relatively high Tc of the material, maintenance costs and efforts could be significantly reduced.
ASG, in its Columbus Wire BU, has been involved in the Sea-Titan project thanks to its expertise in the production of $MgB_2$ wires. The $MgB_2$ wire fabrication starts using ˜ a Powder-in Tube (PIT), ex-situ approach, allowing a better control over powder performances with respect to an *in-situ* approach.
Powder is inserted into a metal tube, which then is cold-worked by drawing. This tube, called "monofilament", is the base unit for multifilamentary wires which are made of multiple monofilaments, stacked together inside a larger metal tube and then deformed to produce a wire.

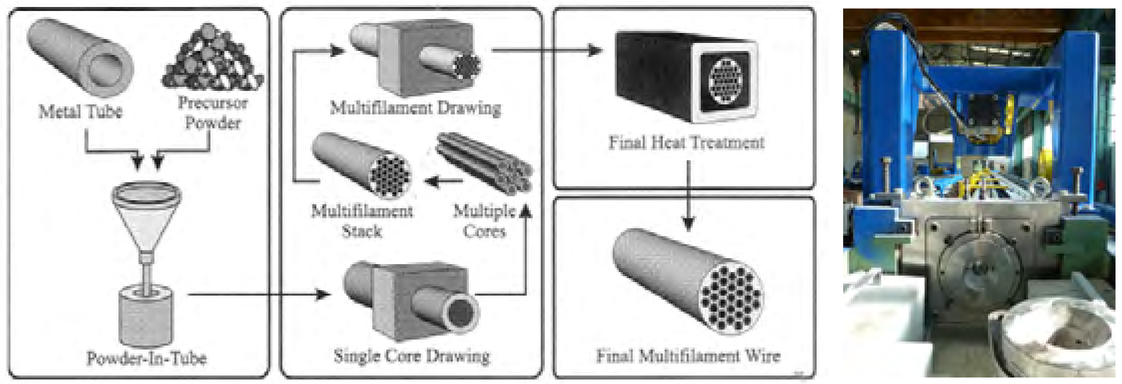


**Figure 4** $MgB_2$ wire manufacturing process.

The full in-house-developed process is able to realize an elongation factor of 2000, having as a result kilometres of continue and uniform spools. The process ends with the final heat treatment, where the wire is given its final superconducting and mechanical properties.
Wire architecture, materials and heat treatment are carefully selected to meet the magnet design and requirements, in a cost and quality driven approach. Besides the actual portfolio of standard product, custom wire shall be designed to cover specific needing.
One of the suitable wires for the application is a standard production round wire usually made for high-current transport purposes. The wire has a round shape having ~1mm of overall diameter and a multifilamentary architecture made of 37 monofilaments. The powder is a standard undoped $MgB_2$ with optimized performance at low magnetic field and high temperature. After more than 1Mm of total wire length production, requisites are met and homogeneous over a length which is nowadays > 3500m (single piece).

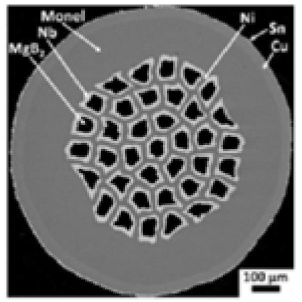


Figure 5 $MgB_2$ round wire.

| Material | Composition [%] |
|---|---|
| MgB2 | 12 |
| Nb | 13 |
| Ni | 15 |
| Monel | 46 |
| Cu | 14 |





## A superconducting PTO: ac losses

Superconducting materials are characterized by zero resistance below a critical temperature. This means that in a superconducting coil there is no power dissipation for Joule's effect (described by the following equation)

$$P_{Joule}=RI^2$$

This is true if the coil is powered by a dc current. If a superconductor sees a field variation with the time, as in an a.c current situation, a wasted power is generated inside the superconductor. This power warms the coils, so a higher cooling power is required to keep the coils cold.
Since the electrical machine needs to generate power, a positive balance between generated and used power is necessary.
ASG, in its Magnet BU, was involved in the Sea-Titan project to study how the ac losses affect the superconducting PTO behaviour and to find how to reduce their impact.
Superconductors subjected to varying magnetic fields see multiple heat sources that can impact on the conductor performance and stability.
The first heat source is called Hysteretic loss and it is due to the magnetization cycle of the superconductor. This kind of loss is proportional to the the magnetic field variation rate and to the wire properties (number and diameter of filaments and critical current). If the wire transports current, the loss is enhanced.
The second kind of loss is present only in multifilamentary wires and it is due to the intrafilamentary currents. It is possible to demonstrate that a superconducting wire subjected to an external varying magnetic field induces an electrical field, and consequently a current in to the resistive wire stabilisation matrix. These losses are called Coupling Losses and they are proportional to the magnetic field variation rate and to the matrix electrical conductivity.
Lastly, if in the conductor there are ferromagnetic materials, another kind of Hysteresis Losses can develop inside these materials. The calculation of this component is always related to the area of the ferromagnetic material magnetization cycle.
ASG, in its study, implemented Wilson's formulation for ac losses in a Matlab code. Considering the temporal magnetic field trend on each single wire inside the coil, the ac losses generated on each wire were calculated. This study showed that the main loss factor in the superconducting PTO is due the Coupling Losses. The low resistivity of the stabilizer matrix and the high magnetic field variation rate generate high Coupling Losses. In order to reduce this dissipation, it is necessary to act on both the wire characterization and on the profile of the current flowing inside the coils.
These results could be the starting point for another project.

## Conclusions

Superconductivity could give a great improvement to the power generation. Nowadays some superconducting solutions have been implemented in wind energy, but also the ocean energy could be interested in a superconducting conversion.
The Sea-Titan project has started to work in this direction. A goal of the project was the feasibility study for a superconducting Power Take-Off. ASG had a main role within this specific target thanks to its expertise. Two topics were in charge of ASG: the $MgB_2$ wire definition and the study of ac losses.
The result of the study showed that the ac losses could be a critical point because they are too high. Other studies are necessary to implement a superconducting solution for the ocean energy production but they are an investment for the future.

# $MGB_2$ SUPERCONDUCTING LINKS

# SUPERCONDUCTING LINKS FOR VERY HIGH-POWER TRANSMISSION BASED ON $MgB_2$ WIRES

Christian-Eric Bruzek (ASG)
Adela Marian (IASS)

This paper presents the main technological achievements of the first 3-gigawatt-class HVDC superconducting cable system, which was manufactured and successfully tested in the European project Best Paths.
The technical focus is set on the cable conductor, the electrical insulation, and the high-voltage terminations. Furthermore, the implementation challenges of long-length systems are briefly outlined, along with environmental benefits and next steps for this new technology.

This work was supported in part by the European Commission within the Seventh Research Framework Programme under Grant 612748.

## Introduction

Within the European project Best Paths that ran from 2014 until 2018 [1], one demonstration task investigated, built and qualified a high-voltage direct-current (HVDC) superconducting system operating at the multi-gigawatt level. The high transmission powers were motivated by recent studies demonstrating the need for additional pan-European corridors extending over several hundred kilometers and having capacities up to 20 gigawatts (GW) [2].
More specifically, a full-size 3-gigawatt-class superconducting DC cable system operating at 320 kV and 10 kA was demonstrated for the first time in Best Paths [3]. The cable is based on the magnesium diboride ($MgB_2$) superconductor, which is very economical to produce and is already commercially available in kilometric lengths. This is in contrast to ceramic-based superconductors that are based on more costly rare-earth components and have a complex manufacturing process.
The cable includes a fault-tolerant cable conductor, a high-voltage insulation layer and a cryogenic envelope. Apart from the cable itself, the complete system includes the cooling machine maintaining the temperature and the pressure of the cryogenic fluids, and two terminations to connect to the electricity grid. All these key components were specified, designed, developed and optimized for an industrial production during the project, providing manufacturing and assembling solutions that ensure feasibility, robustness, and practical usefulness. Although no joints were included in the project, an appropriate conceptual design already exists.
An important feature of the project was the consideration of the actual needs of the transmission system operators, in particular in the initial design phase. For instance, the input data provided by the French transmission system operator RTE was essential for the design of the cable conductor, as it specified the expected performance and behavior in the electricity grid, particularly under transient conditions.

[1] Best Paths project websites. www.bestpaths-project.eu and https://www.iass-potsdam.de/en/research/beyond-state-art-technologies-repowering-ac-corridors-and-multi-terminal-hvdc-systems-best.

[2] e-HighWay2050 project results, "Europe's future secure and sustainable electricity infrastructure". https://docs.entsoe.eu/baltic-conf/bites/www.e-highway2050.eu/e-highway2050/.

[3] A. Marian, S. Holé, N. Lallouet, E. Marzahn, and C. E. Bruzek, "Demonstration tests of a 320-kV-class DC superconducting cable for transmission of high powers", IEEE Elec. Insul. Mag., vol. 36, no. 1, pp. 30–40, January 2020.

This work was supported in part by the European Commission within the Seventh Research Framework Programme under Grant 612748.
The most important specifications of the cable system are summarized in Table 1.

**Table 1.** Specification of the $MgB_2$-based HVDC cable in best paths

| Parameters | Value |
|---|---|
| Power | 3.2 GW |
| Voltage | 320 kV |
| Operating DC current | 10 kA |
| Cooling medium | He gas for $MgB_2$ |
| | $LN_2$ for insulation and thermal shield |
| Cryogenic losses | < 0.2 W/m at 20 K in He gas |
| | < 2 W/m at 70 K in $LN_2$ |
| Current ripple | 1% amplitude at 50 Hz |
| Fault current | 35 kA during 100 ms |
| Power reversal ramp | 100 MW/s to 10 GW/s |

The following sections are focused on the main technological achievements of the project, namely design of the cable conductor and high-voltage insulation (Section II), concept of the electrical terminations (Section III) and testing of the demonstrator (Section IV). The last two sections are dedicated to long-length systems and environmental benefits, respectively.

## 2. Cable design

The different design options for a superconducting cable system are discussed in detail in reference [4], which also presents the decision-making process carried out in Best Paths. The chosen cable design is schematically shown in Fig. 1, with the main components indicated accordingly.

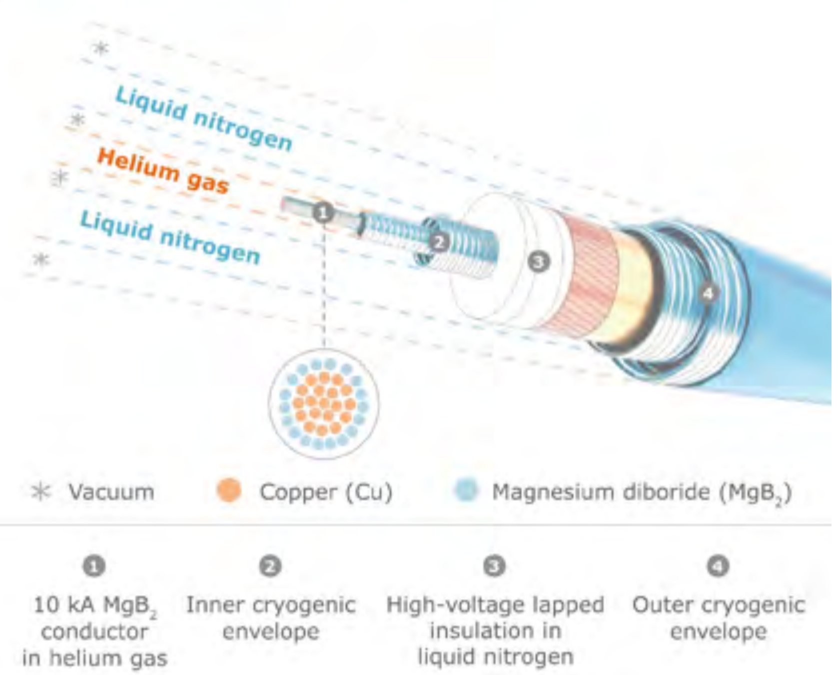


**Figure 1.** Sketch of the 3.2 GW $MgB_2$ cable system showing the key components. The electrical terminations are not represented here.

### A. Cable conductor

To ensure the superconducting properties of the $MgB_2$ material, its operating temperature needs to be maintained in the range of 15 to 25 K (~ -250°C). This temperature range can be reached by using gaseous helium or liquid hydrogen. In the project, gaseous helium was selected as a coolant for the cable conductor, as the Nexans test platform is not equipped for testing in an explosive environment. A commercial cryogenic line was used for circulating the cooling fluids. These cryogenic envelopes have already been in use on industrial and large-scale scientific sites for several decades. They are flexible and can be produced in kilometric piece lengths. Their performance and characteristics are detailed in [5].
As shown in Fig. 1, the cryogenic line includes an external thermal shield actively cooled by liquid nitrogen ($LN_2$) in the temperature range of 70 to 80 K, and two vacuum thermal insulation chambers to reduce the heat

[4] J. Muñoz-Antón, A. Marian, F. Lesur, and C.-E. Bruzek, "Dichotomic decision optimization for the design of HVDC superconducting links", Entropy, vol. 22, Art. no. 1413, December 2020.

[5] S. Klöppel, A, Marian, C, Haberstroh, and C.-E. Bruzek, "Thermo-hydraulic and economic aspects of long-length high-power $MgB_2$ superconducting cables", Cryogenics, vol. 113, Art. no. 103211, January 2021.





inleak into the cable. The $MgB_2$ conductor is itself housed in the innermost helium-cooled cryogenic envelope whose outer wall is lapped with high-voltage insulation.
The cable conductor is assembled by helically winding 18 $MgB_2$ wires around a flexible copper core. Its bare diameter is around 9.5 mm. Fig. 2 shows the conductor cross section and details of one of the $MgB_2$ wires developed for the project. A critical current of up to 14 kA at 20 K in self-field has been found, which is in accordance with the expected behavior.

[6] C. E. Bruzek et al., "Cable conductor design for the high-power $MgB_2$ DC superconducting cable project of BEST PATHS," IEEE Trans. Appl. Supercond., vol. 27, no. 4, Art. no. 4801405, June 2017.

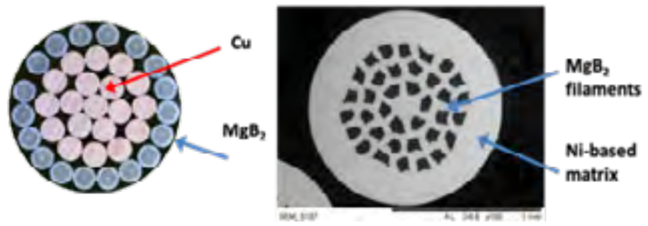


**Figure 2.** Picture of the 10 kA cable conductor consisting of 18 $MgB_2$ wires wound around a copper core (left) and one $MgB_2$ wire composed of 36 superconducting filaments embedded in a matrix of nickel and monel (right).

Analytical and finite-element modeling were used to design, enhance, and validate the cable structure under the transient grid conditions listed in Table I. For instance, modeling is used to check that the losses generated by ripples can be considered as negligible and that during the power reversal ramp the cable does not present any risk of quenching for ramp values lower than 5 GW/s which cover most of the specification range [6].
Numerical simulations were also employed to optimize the amount of copper required for efficient protection of the cable conductor during a fault. The copper core acts as a low-resistance electrical shunt protecting the superconducting wires. Thus, the resistive wires transport the inrush current in excess of the superconducting critical current during the fault clearance. Since the copper core has a very low resistance at 20 K (RRR >150), it can accept high fault currents (35 kA). However, during such a fault, the Joule effect causes an increase in temperature and the cable must be rapidly disconnected to prevent any damage. A typical fault clearance requires less than 100 ms, and the acceptable temperature rise during and after fault was shown to be maximum 100 K.

As soon as the fault is cleared, the cooling system returns the operating temperature to 20 K. This cooldown operation can take several minutes.
Apart from the conceptual design, specific work has been carried out at ASG Superconductors and Nexans concerning the $MgB_2$ wires and cables, which are now ready for large-scale deployment. As the cable is very compact, the operating current level is easily adjustable to grid requirements by simply adding or removing one or several wires.
For the future electricity grids, hundreds of kilometers of HVDC cables are envisioned, which will require a large quantity of superconducting wires. $MgB_2$ wires are based on abundant and low-cost materials and a fully industrial manufacturing process, making them a good candidate for bulk production. The length of a single piece was optimized to 2 km, with a highly reproducible level of the critical current and wire diameter. ASG is now able to produce several hundreds of kilometers of such a wire. A 2 km piece is well suited both for the industrial cabling process and for the grid installation requirements that permit a limited number of cable joints. Beside the industrialized strand production, the cable itself was manufactured on standard industrial cabling machines, as illustrated in Fig. 3. After adjustment of the cabling tooling, no critical current degradation was detected on the wires extracted from the cable.

**Fig. 3.** Planetary cabling machine from Nexans used to manufacture the cable conductor for Best Paths (courtesy of Nexans).

At the end of the project, several hundreds of meters of cable conductor have been produced, demonstrating the high reliability of the $MgB_2$ wire and cable manufacturing processes.

## B. High-voltage insulation

The HVDC system requires a simultaneous operation at both high current and high voltage. A thick dielectric material is necessary for the voltage insulation between the pole and ground. This insulation should present a high voltage breakdown strength and could be similar to the dielectrics used for resistive cables, made out of polyethylene or polypropylene layers.
If the dielectric is located outside the cable cryostat, the insulation will operate at room temperature in a so-called "warm dielectric" design [7]. Another option is to place the high-voltage insulation as close as possible to the cable conductor at cryogenic temperature, in a so-called "cold dielectric" design [8]. This second option was selected for the Best Paths demonstrator because it presents some advantages for cryogenic management and installation.

[7] A. Morandi, M. Marzinotto, and G. Mazzanti, "Feasibility of high voltage DC superconducting cables with extruded warm dielectric", in Proceedings of the 2014 IEEE Conference on Electrical Insulation and Dielectric Phenomena (CEIDP), Des Moines, IA, USA, 19–22 October 2014, pp. 796–799, DOI: 10.1109/CEIDP.2014.6995878.

[8] A. Marian, S. Holé, F. Lesur, M. Tropeano, and C. E. Bruzek, "Validation of the superconducting and insulating components of a high-power HVDC cable", IEEE Elec. Insul. Mag., vol. 34, no. 1, pp. 26–36, January 2018.

**Fig. 4.** Picture of the demonstrator successfully tested in Best Paths.

As illustrated in Fig. 1 and Fig. 4, the insulating material is placed just outside the inner cryogenic envelope and housed inside the outer cryogenic envelope. The dielectric material is a lapped insulation that operates in $LN_2$ at 70 K. Paper lapped insulation is a standard material for the cable industry and has been used in very long submarine cables impregnated with oil. In our cold dielectric design, $LN_2$ replaces the oil. In addition to its efficient cooling properties, $LN_2$ also has good dielectric strength properties. To benefit from these properties, a Kraft paper lapping maintains a porous space that is impregnated by $LN_2$ during the cable cooldown.
A thorough analysis of DC breakdown mechanisms and space charge characterization have been carried out in the project [3, 8]. It has been found that Kraft paper impregnated with pure $LN_2$ (no gas bubbles) shows high dielectric performance (electric field breakdown > 30 kV/mm measured on thick layer). Kraft paper is also tolerant to the presence of internal defects such as holes. For limited damages, thanks to the high dielectric strength of $LN_2$, the insulation recovers its initial dielectric properties after a breakdown when "fresh" $LN_2$ refills again the damaged space. Furthermore, it was also shown that no trapped space charge can migrate or accumulate within this material, which gives good confidence in its long-term reliability.
Therefore, a high-voltage insulation based on Kraft paper impregnated with $LN_2$ is robust and is recommended as a dielectric material for super-conducting HVDC systems, as soon as no $N_2$ gas bubbles are generated.





### 3. Terminations

The main target in the development of HVDC terminations was to demonstrate the 320 kV voltage class in DC while accommodating the $MgB_2$ superconductor at 20 K. Generally, terminations need to fulfil two main functions: (I) secure the injection of the high current and high voltage from the grid to the superconducting cable, and (II) transfer the pressurized cryogenic fluids from the cooling system to the cable. The termination includes a special current lead providing a transition zone between resistive and superconducting materials. This transition zone is optimized to maintain low thermal conduction losses in the cryogenic fluids of the system despite the significant Joule losses from high current flow in the resistive part. The termination also manages the electric field stress between the high voltage at its top and the ground potential at its bottom.

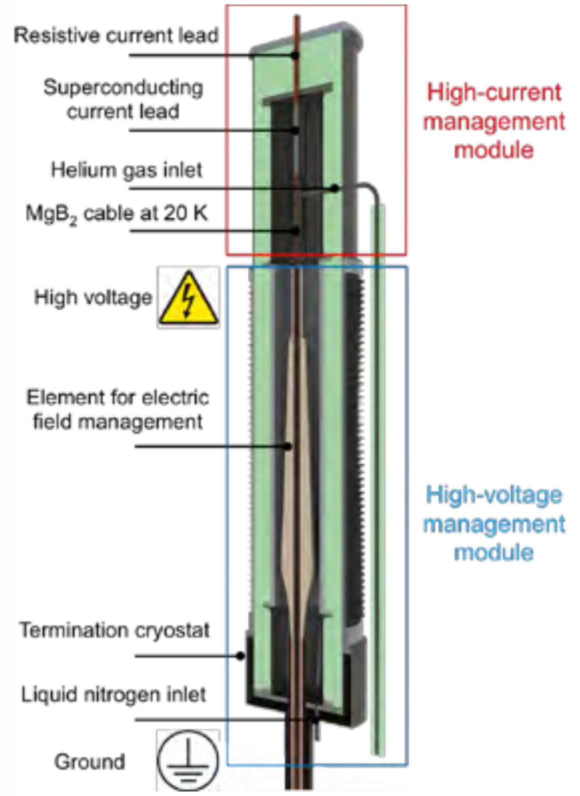


**Fig. 5.** Sketch of the HVDC termination developed for Best Paths, highlighting its modular design.

The design of the termination is innovative, as it effectively separates the current and voltage functionalities, resulting in a strong modularity of this accessory. As shown in Fig. 5, the termination is split into two fully independent parts: in the upper part the current is injected through the special current lead connected to the cable conductor, while the high-voltage gradient is attended to in the lower part. This design is evolutive and can easily be adapted to different voltage and current values. For instance, if the operating current of the system changes, only the upper part of the termination has to be modified, whereas the lower part remains unaffected, and vice versa.

[9] Cigré working group B1.31 convened by D. Lindsay, "Recommendations for testing of superconducting cables," Cigré Technical Brochure 538, June 2013.

[10] Cigré working group B1.32 convened by B. Sanden, "Recommendations for testing DC extruded cable systems for power transmission at a rated voltage up to 500 kV," Cigré Technical Brochure 496, April 2012.

## 4. HVDC Testing

No standard has been yet established for testing HVDC superconducting cables. Some useful recommendations are given by the Cigré brochures [9; 10]. The combination of these two sets of good practices constituted a basis for proposing a testing methodology for the Best Paths superconducting demonstrator. Moreover, the resulting protocol for the HVDC tests was shared with and accepted by the transmission system operators who were partners of the Best Paths project. Along with the testing protocol, the measurements and results obtained within Best Paths hence constitute a significant step toward preparing a new standard for testing superconducting HVDC cables prior to their installation in the electricity grid. The high-voltage testing was carried out at an industrial test platform on a 30-meter superconducting loop connected to two terminations. It was conducted at up to 592 kV, which is the testing voltage required to qualify 320-kV-class systems. The test platform arrangement is presented in Fig. 6, and an in-depth description of the testing protocol and results is reported in [3].


**Fig. 6.** Testing loop shown together with the 800 kV DC generator on the Nexans testing platform (courtesy of Nexans).

Note that the small cooling systems that provided overcooled $LN_2$ and helium gas were specifically designed for the testing loop. The cold power and mass flow were therefore adjusted according to the hydraulic parameters of the loop. In the future, the specification of these machines should be reexamined according to the length of the link under consideration. The loop elements of the manufactured cable system successfully passed the testing program for the 320 kV class without any breakdown. This confirms the availability of the superconducting HVDC cable technology for transmitting bulk power higher than 6 GW (for bipolar systems). These innovations also open new possibilities to design superconducting DC links for the future.

## 5. Implementation toward long-length HVDC cable systems

Best Paths has demonstrated operation of gigawatt-scale systems on industrial test platform using a "type test" strategy. However, in practice, an HVDC link can be several hundreds of kilometers long, built with several segments connected in series. This requires field joints to extend the electrical and the hydraulic circuits. These elements have already been conceptualized but should be prepared and experimentally tested with the same testing protocol as the loop.

In addition, several large cooling and pressurization stations are required to maintain the cryogenic conditions for the superconducting link. They should be distributed along the link to keep the cooling fluids in the temperature/pressure ranges of 15-20 K / 10-20 bar and 70-100 K / 3-15 bar for helium and $LN_2$, respectively. As a superconducting cable does not generate Joule losses, the energy cost required for these devices is the only operating cost of the system.

The span between two cooling stations depends on the available space for installation and the local elevation of the link. To install long links, adjustments of the cryogenic envelope diameter are also required. Different scenarios are presented and discussed in [5]. With the existing cryogenic machines and lines, a span between two cooling stations of up to 50 km is achievable. However, investment costs are reduced if the distance is reduced to the range of 10-20 km.

All required technologies and equipment are commercially available at this point. As an example, the AmpaCity cable system in Essen [11] has been operating in the electricity grid since 2014 with 100% availability, energizing a full district close to the city center. Furthermore, large cryogenic machines and circulation pumps have proven their reliability and robustness during several decades of operation in high-energy applications [12], at even lower temperatures (1.8 K) than the one needed for $MgB_2$.

[12] S. Claudet, P. Gayet, P. Lebrun, L. Tavian, and U. Wagner, "Economics of large helium cryogenic systems: Experience from recent projects at CERN", in Advances in Cryogenic Engineering, Q.-S. Shu, Ed., Springer: Boston, MA, USA, 2000, pp. 1301–1308.

[13] A. Marian et al., "An $MgB_2$ HVDC superconducting cable for power transmission with a reduced carbon footprint", in Eco-design in Electrical Engineering: Lecture Notes in Electrical Engineering, J.-L. Bessède, Ed., Springer: Cham, 2018, pp. 129-135

[11] M. Stemmle, F. Merschel, M. Noe, and A. Hobl, "AmpaCity project—Worldwide first superconducting cable and fault current limiter installation in a German city center", in Proceedings of the 22nd International Conference and Exhibition on Electricity Distribution (CIRED 2013), Stockholm, Sweden, 10–13 June 2013, DOI: 10.1049/cp.2013.0905.

Conservative economical models proposed in [5] indicate that the proposed superconducting link is economically viable both in terms of investment and operation costs for transmitted powers higher than 3 GW, when compared to a resistive link. For the concrete case of a 6.4 GW link with a length of 500 km, a comparison of the capital costs can be seen in Fig. 7. The $MgB_2$-based superconducting link is overall 27% less expensive than the resistive solution. This is primarily due to the small footprint of the superconducting link, which leads to a reduction in the expenditure on civil engineering and right-of-way by a factor of 2.6. The capital cost is very similar for both links, whereby the superconducting system also includes the cooling stations. Furthermore, the technology and cost of the converters that deliver 320 kV and 10 kA is identical for both solutions.

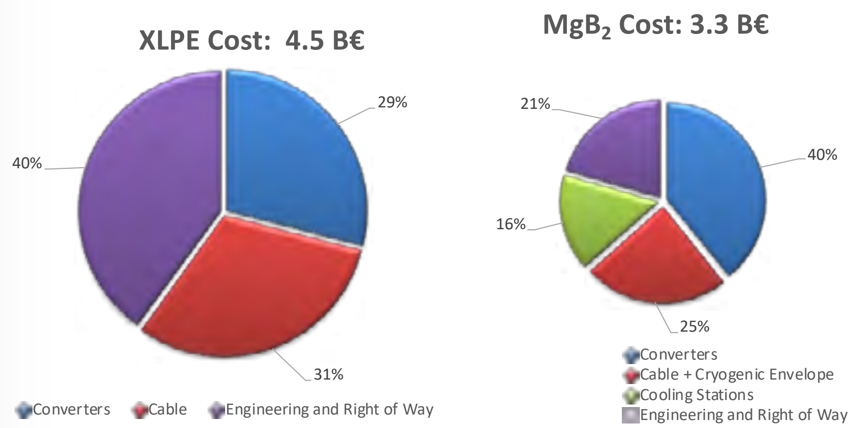


**Fig. 7.** Capital costs of resistive XLPE cables and $MgB_2$ superconducting cables for a 6.4 GW DC power link with a length of 500 km.

## 6. Environmental and neighborhood benefits

A life-cycle assessment (LCA) of the environmental impact of the HVDC superconducting cable system determined a strong reduction of most the considered indicators [13].
As the cryogenic envelope completely eliminates thermal dissipation to the surrounding area, superconducting power links can be laid underground in a confined environment. By contrast, the current rating of resistive cables is decreased by mutual heating between adjacent circuits.
The absence of heat dissipation and the compact design offer a significant advantage for superconducting cables in areas with high ambient temperature, or when crossing busy urban districts, or within forested or pristine areas.
In addition, their compact size and reduced footprint are clearly highlighted in Fig. 8, which shows that one pair of high-power superconducting cables has the same transmission capacity as eight resistive cables. This leads to a reduction of the footprint by a factor of 10 and expedites the permitting process.


Fig. 8. Comparison of the environmental footprint of resistive XLPE cables and $MgB_2$ superconducting cables for a 6.4 GW DC power link.

## 7. Conclusion and next steps

A gigawatt-scale HVDC superconducting cable system was designed and tested in Best Paths. Based on $MgB_2$ superconducting wires, this system was shown to be technologically mature and cost competitive for bulk power transmission.
With their high efficiency, compactness and reduced environmental impact, superconducting cables offer several technological advantages that are likely to find high public acceptance. An important next step will be to develop testing guidelines for HVDC superconducting cables to guarantee safety and quality standards.
Only the operation of such a high-power cable in real-life grid conditions will confirm the full potential of this technology in a definitive manner.
In this respect, the involved partners recommended at the end of the project that appropriate de-risking instruments for the transmission system operators be put in place within the framework of European energy-climate policies.
The Best Paths demonstrator was designed to operate in gaseous helium as a cooling medium. Based on the developed design, the coolant can be replaced by liquid hydrogen in future prototypes. In addition to electricity transmission, such a superconducting cable system would also offer a smart and safe option for storing and distributing large amounts of hydrogen under low pressure. Pending issues involve the necessary risk management associated with the use of hydrogen along with the testing and certification of the relevant equipment by authorized bodies. Lastly, an experimental investigation of the dual transport of these energy carriers – hydrogen and electricity – would support the European Green Deal agenda.

**Acknowledgment**
We are very grateful to all the DEMO 5 partners who contributed over the years to the success of the project. The Institute for Advanced Sustainability Studies is funded by the German Federal Ministry of Education and Research (BMBF) and the Brandenburg State Ministry of Science, Research and Culture (MWFK).

# POWER TAKE-OFF TECHNOLOGY

# SEA-TITAN: A REVOLUTIONARY POWER TAKE-OFF TECHNOLOGY

Martina Neri

Europe's 2050 Energy Strategy targets a reduction of greenhouse gas emissions by 80%-95% compared to 1990 levels with renewable energy accounting for at least 64% and up to 97% of the electricity consumed.

The Ocean Energy Forum produced the Ocean Energy Strategic Roadmap which has estimated that 100GW of ocean energy capacity could be deployed, producing around 350TWh of electricity meeting up to 10 % of Europe's demand by 2050.

The ocean energy is based on the use of Wave Energy Converters (WECs) which produce electricity from waves. The core of a WEC is the Power Take Off (PTO), which transforms mechanical movements into electrical energy.

www.seatitan.eu

## Introduction

On 12 December 2019 the European Council, taking note of the Communication of the European Commission on the European Green Deal, endorsed the objective of achieving a climate-neutral EU by 2050, in line with the objectives of the Paris Agreement and in the light of the latest available science and of the need to step up global climate action. In crude numbers, the Europe's 2050 Energy Strategy targets a reduction of greenhouse gas emissions by 80%-95% compared to 1990 levels with renewable energy accounting for at least 64% and up to 97% of the electricity consumed.
To achieve a reliable increase of the proportion of energy consumed to be coming from renewable energy sources, a well assorted mix of natural energy sources is needed. Today, photovoltaics, wind and hydroelectric power represent the vast majority of the available renewable energy.

In addition, the Ocean Energy Forum (OEF) produced the Ocean Energy Strategic Roadmap (November 2016) which has estimated that 100GW of ocean energy capacity could be deployed in Europe by 2050, producing around 350TWh of electricity meeting up to 10 % of Europe's demand by 2050. The achievement of this target would contribute significantly to the diversification of the renewable energy sources.

This ocean energy is based on the use of so-called Wave Energy Converters (WECs) which produce electricity from waves. The core of a WEC is the Power Take Off (PTO), which transforms mechanical movements into electrical energy.

The Sea-Titan project aims at developing a simpler, more robust and cost effective multi-technology compatible PTO.

The project, born in 2018, has received funding from the European union's Horizon 2020 research and innovation programme and brings together 11 partners from 7 European countries.

The main goal of the project is to design, build and test a prototype of a new configuration of PTO, but in parallel with this goal, it aims at exploring the possibility of developing a PTO based on a superconducting machine.

The efficiency of a PTO can be described by a parameter: the force density (Force to Mass Ratio Capacity). Increasing this parameter is the primary objective for the ocean energy industry. A superconducting PTO can significantly increase the force density whilst also reducing the size.

A superconducting solution is studied by ASG Superconductors in collaboration with CIEMAT. In particular, ASG has been involved in the definition of the superconducting wire and in the estimation of the amount of ac losses in the wire during operation of the PTO.

## Wave Energy Converters

Wave ocean energy is acquired using Wave Energy Converters (WECs). Presently, there are a significant number of competing Wave Energy Converter (WEC) technologies using different concepts and designs.

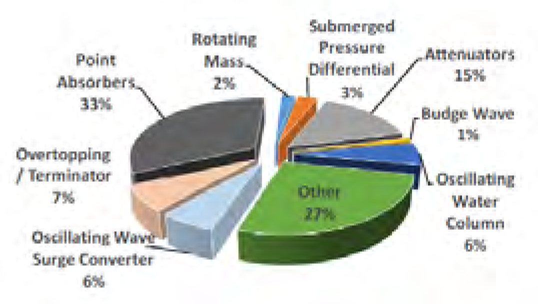


**Figure 1** Different WEC typologies and their distribution rate.

They can be classified based on their location (Onshore – Nearshore – Offshore) and on their orientation with respect to the wave (Attenuator – Terminator – Point Absorber).

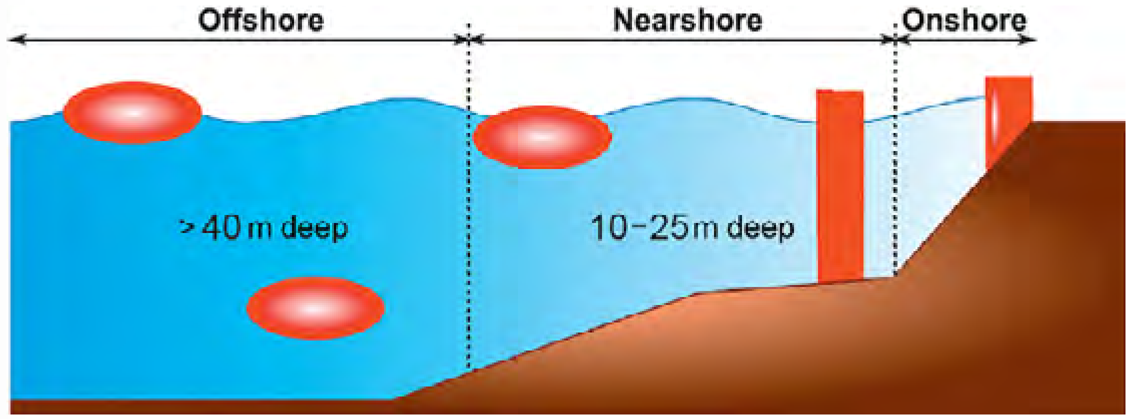


**Figure 2** Classification of the WEC typologies based on location.

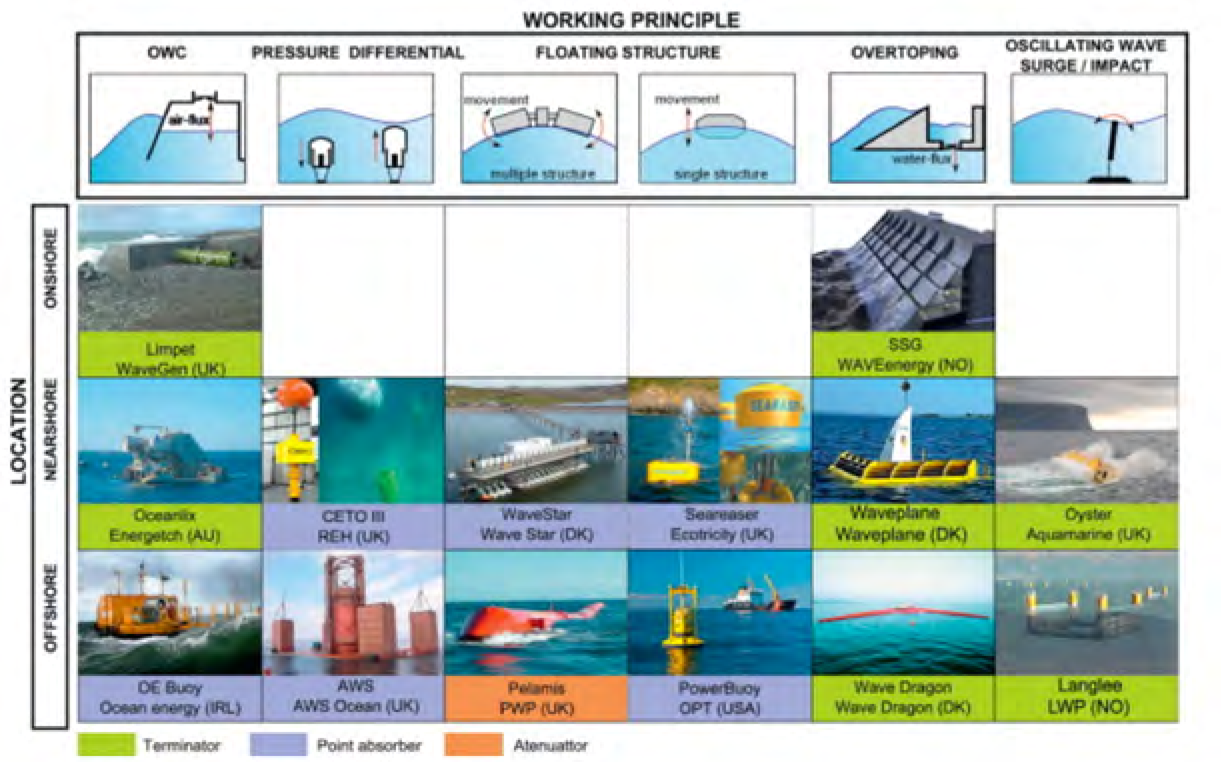


Figure 3 Classification of WEC typologies based on location and working priciple.

The Point Absorber type WECs are the most numerous; they are simple, omni-directional and easy to deploy.
Among these WEC topologies, a Heaving Point Absorber (HPA) is a two body WEC based on the relative movement of two bodies: one is stationary or pseudo-stationary and it is called the Spar, while the other is a moving body and it is called the Float, floating at the sea surface and excited by wave force.

The working principle of an HPA is quantified by means of an equivalent model, based on a quite simple concept. There are two forces acting on the Float of the WEC, one produced by the wave and the other by the PTO, both acting upon a mechanical system characterized by its impedance. Alternatively, the problem can be seen as two generators (corresponding to each force; wave and PTO) which are coupled through an impedance and the question is to adjust the value of the PTO force to extract the maximum amount of energy from the wave.





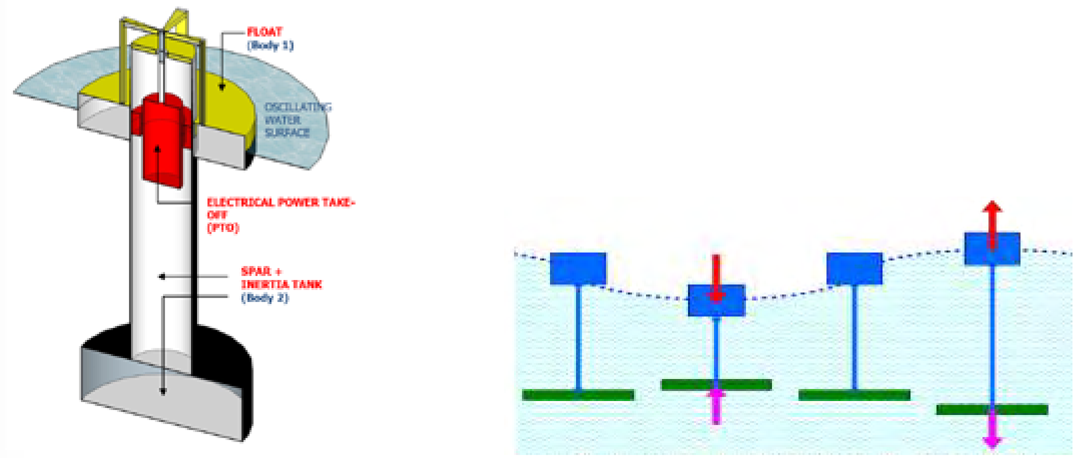


Figure 4 Configuration of a Heaving Point Absorber.

## Power Take Off

The PTO is the device which converts the mechanical energy from the wave into electricity. The conversion can be done in several steps or in a single step by using a linear electricity generator. In this latter configuration the PTO is known as a Direct-Drive system.

Direct-Drive machines are all based on a Translator/Stator configuration which balances the transverse forces.
The forces in ocean energy are produced by the waves. In order to maximize energy production, the system must work close to resonance.
In this configuration, the Stroke, the maximum amplitude of the translator motion, can be high even if the waves are small.

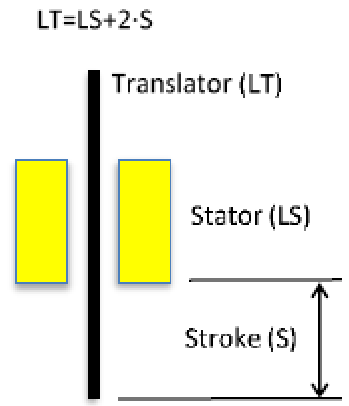


Figure 5 Direct-Drive machine scheme.

Any electrical machine is defined by the Shear Stress, the force produced per unit surface of its airgap. This parameter is proportional to the product of the electric load of the machine (expressed in kA/m) times the magnetic load of the machine (expressed in Tesla).
There are several topologies of linear machines, differing primarily in the way the magnetic field is generated: by means of permanent magnets or electromagnetic coils.
In marine applications, permanent magnets are not appropriate because they are very delicate components, prone to corrosion.

Given all these considerations, the Sea-Titan project has focused its work on the development of a new PTO for a Heaving Point Absorber WEC, based on a Switched Reluctance Machine (SRM).
In this machine configuration there is an Active side (coils generating the magnetic field) and a Passive side (iron). The two sides move with respect to each other. At a given amount of total current, the force increases according to the reluctance of the iron path.

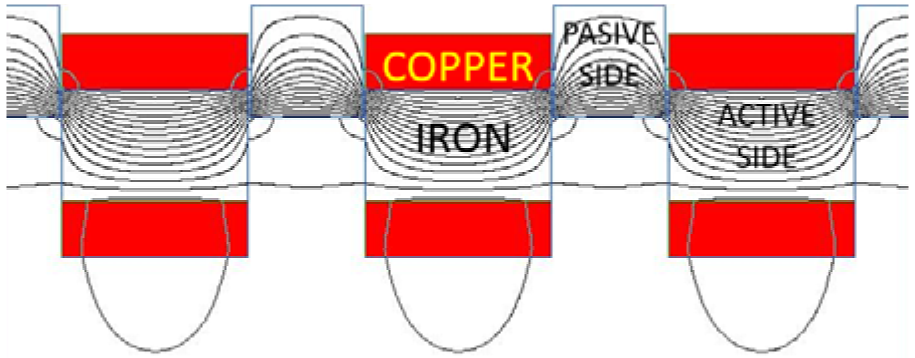


**Figure 6** A Switched Reluctance Machine has an Active side (copper and iron pole) and a Passive side (iron) moving one respect of the other.

The goal of the project is to enhance the force density with reduced impact on the volume of the machine.
Two different approaches have been identified. The first approach is to design, built and test a new configuration of a machine using conventional wire.
The second approach is to consider using superconductivity to increase the electrical output of the machine, eliminating in practice the losses while improving the shear stress significantly. This will be considered as a long-term option for a future generation of Direct Drive PTOs.





Superconducting PTO

Superconducting coils in a linear machine can tolerate higher current densities which generate higher forces, without increasing the volume of the machine.
Indeed, the advantage of using a superconducting machine as a PTO in general and a superconducting SRM machine in particular can be easily explained considering that the produced force is proportional to the product of the magnetic flux density times the total current in the coil phase. In a non-superconducting coil, there is a strict limit to the current that the coil can transport but in a superconducting one that limit is much higher and this means that very big currents can be transported in small volumes. The difference between a non-superconducting machine and a superconducting one, both with iron in their magnetic circuit, is that although they work at similar magnetic flux density levels (slightly higher in the superconducting case), this small variation in the field (in the range of 10% to 20%) implies a tremendous variation of the current and consequently of the force.

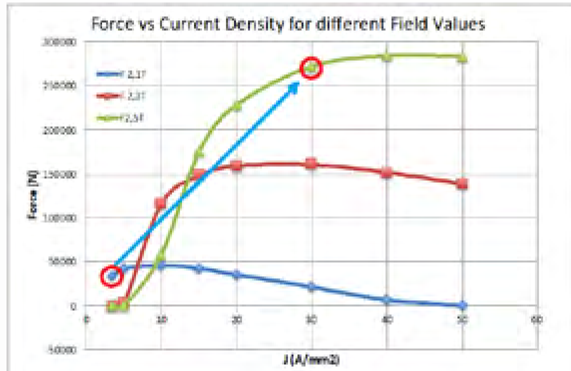


**Figure 7** Force vs Current Density for 3 values of B. For a normal conductor, working above 3-4 A/mm$^2$ is not possible (the best option is the blue curve). For a superconducting machine it is possible to achieve 30 A/mm$^2$, jumping to the green curve.

Using superconductivity in PTOs provides a fine example of the paradigm of superconductivity: on the one hand, the reduction of space and the increase of efficiency and force which are very useful advantages for this application but, on the other, the increased complexity, particularly in such a difficult environment as operating in the ocean.
Nowadays, various types of superconducting machines have been proposed, most of them in the sector of wind energy. Some solutions are based on High Temperature Superconductors (HTS), but there is at least one based on magnesium diboride ($MgB_2$).

Focusing on Superconducting Linear Machines, the number of developments is small. The most well-known machine is the Japanese Maglev which uses a Long Stator Synchronous Motor with superconducting excitation.
Most of the other proposals are based on using Synchronous Linear Motors with a normal conducting Long Stator and a superconducting Translator based on bulk HTC permanent magnets to avoid superconducting coils in the moving parts.

In the wave energy sector there has until now been only one superconducting solution, based on a Linear Synchronous Machine with superconducting excitation and normal conducting stator.
There are different critical issues with superconducting machines.
The first issue is related to alternating current (ac) losses.
Superconducting materials are characterized by zero resistance below a critical temperature. This means that in a superconducting coil there is no power dissipation producing joulean heating.

$$P_{Joule}=RI^2$$

If the coil is powered by direct current (dc), R is zero and no power is generated, so there are no losses. However, if a superconductor is exposed to a time-varying field, as is the case with an alternating current (ac) source, power is generated inside the superconductor. This wasted power, called ac loss, produces heat which must be extracted, increasing the complexity of the arrangement. Superconductors are very sensitive to the frequency of the time variation: for standard frequencies (50 Hz) the ac losses are simply inadmissible. Indeed, all the previously mentioned PTO proposals only use superconductivity on the dc side.
Nevertheless, using superconductivity in both ac and dc sides of the machine is becoming increasingly attractive, providing a big reduction in the size and efficiency of the machine.
The second issue is related to cooling. Superconducting coils must be installed in a cryostat to keep them at cryogenic temperatures. Related to this point a big challenge is how to move cold coils inside cryostats.

In the SEA-TITAN project, the conceptual design of a Superconducting PTO was based on two considerations:

→ It must be simple and robust within the constraints imposed by the limitations of operating at cryogenic temperatures.

→ All the machine windings (ac and dc) must be superconducting in order to increase the efficiency and to reduce the weight.

The proposed superconducting switched reluctance machine has coils only in one side, the stationary one. In this way the superconducting coils do not move, simplifying enormously the execution of the machine.

## ASG Superconductors Contribution

ASG, thanks to the experience in superconductivity and wire production, is one of the partners of the Sea-Titan project, especially for the work package related to the development of a superconducting PTO.
Two Business Units have been involved in this project: the Columbus $MgB_2$ Unit and the ww.

$MgB_2$ is the best material for a superconducting PTO thanks to its relatively low operational magnetic field. It can carry high currents without needing to be maintained at liquid helium temperature, reducing the cooling power. Moreover, thanks to the stability and the relatively high Tc of the material, the need for maintenance of the cryogenic systems is reduced, along with operating costs.

With the greater flexibility of the unique MgB2 wire ex-situ process, Columbus $MgB_2$ Unit has succeeded in designing and developing improved solutions for products ranging from power cables to magnets for the medical and energy sectors. The manufacturing process provides $MgB_2$ wires with the electrical performance, mechanical properties and single piece lengths required to allow the use of react & wind technology. This minimizes the number of joints and brings HTS device manufacture one step closer to the well-established NbTi technology, while keeping the advantage of the higher operating temperature.
Within the Sea-Titan project, the Columbus $MgB_2$ Unit was appointed to define and optimize the wire for the superconducting coils in the PTO. In order to reach this goal, its experience in $MgB_2$ wire fabrication has been fundamental.

The most suitable wire for this application is a standard production round wire usually made for high-current transport purposes. The wire has a round shape with an overall diameter of ~1mm and a multifilamentary architecture comprising 37 monofilaments. The wire is made using a standard undoped $MgB_2$ powder providing optimized performance at low magnetic field and high temperature. More than a million metres of wire have now been produced and the required operating characteristics can be achieved and maintained homogeneously over a length which is nowadays > 3500m (single piece).

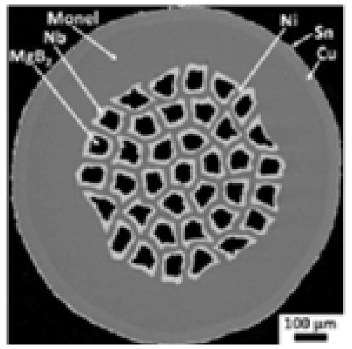


**Figure 8** $MgB_2$ round wire.

The Magnets & Systems Unit has acquired industry-leading know-how in the design, development, production, installation and testing of superconductive and resistive magnets, cryogenic systems, resonance cavities, superconducting solenoids and coils, magnets for cyclotrons and components for made-to-measure applications.
The Unit has been involved in the Sea-Titan project with the goal of handling the ac losses. Thanks to its experience it has had the right skills to face this critical aspect of the design of a superconducting PTO.

## Perspectives

Diversifying the available sources of renewable energy is crucial to achieving a climate neutral EU by 2050. Wave energy converters are expected to contribute to this goal, but significant R&D is still needed to identify the best technical solutions to achieve high power conversion efficiency and a reasonable cost per kW. Superconductivity will play a role, provided that low ac loss conductors and winding solutions would be applicable. The Sea-Titan project outcomes will contribute to clarifying these aspects and helping wave energy to approach these targets.

# ITER PFC MANUFACTURING

Poloidal field coil #6
— the located at the bottom of the ITER machine
and the first in line for installation —
has completed all testing on site in the factory
of Fusion for Energy. (Courtesy of ITER)





# IT'S COLD TEST TIME FOR THE POLOIDAL FIELD COILS OF THE ITER FUSION DEVICE BY THE ASG TEAM!

Alberto Amaduzzi, Eugenio Cavanna, Fabio Fichera, Giulio Pizzigoni (ASG) with the collaboration of Sandro Bonito Oliva, Monica Martinez Lopez (F4E)

Six poloidal field coils positioned horizontally around the ITER vacuum vessel and D-shaped toroidal field coils will help with the shape of the plasma and keep it in suspension away from the walls.

ASG is deeply involved in the manufacturing and testing of the poloidal field coils at the Fusion for Energy (F4E) Poloidal Field coils factory, located at the ITER site.

If results of the preliminary tests are positive, the coil is cooled down to a temperature of 80 K, where the following additional tests are performed and/or repeated: pressure drop test and vacuum leak test of the helium circuit, high voltage DC test and current test.

Six poloidal field coils positioned horizontally around the ITER vacuum vessel and D-shaped toroidal field coils will help with the shape of the plasma and keep it in suspension away from the walls. The top poloidal field coil (PF1) will be supplied by Russia; the five lower ring coils are under the procurement responsibility of Fusion for Energy which is the European domestic agency in-charge of the procurement of the European in-kind contribution to ITER. Four of these will be produced on site. (PF6 has been produced by Europe and China.) ASG is involved in the supply of the ITER Poloidal Field Coils PF2, PF3, PF4 and PF5 and the cold testing of PF6, the provision of both the engineering integration services and Project management for the supply of the Poloidal Fields Coils PF2, PF3, PF4 and PF5. This includes definition, description and management of the interfaces between the various contractors participating in the Project.

The Poloidal Field Coils are fundamental components of the ITER experimental fusion device. Together with the toroidal field coils of which we have produced 10 of 19 at our La Spezia workshop, the poloidal field coils shape the plasma and contribute to its stability. Six poloidal field coils are installed in the ITER machine: PF1 to PF6. Four of them, the PF2, PF3, PF4 and PF5 are so large that they have to be manufactured in the ITER site at Cadarache, in France; the remaining two, PF1 and PF6, are comparably smaller and they are manufactured respectively in Russia and in China. The largest coil has a diameter of 24 m, while the heaviest weighs as much as 400 tons. These coils are manufactured using NbTi superconducting cables, due to the lower magnetic field to which they are exposed in comparison with the toroidal field coils which require the higher performing Nb3Sn material. In all cases, supercritical helium is needed in order to reach the operating temperature of both sets of coils. ASG is deeply involved in the manufacturing and testing of the poloidal field coils at the F4E factory, Cadarache. Despite the difficult times due to the covid-19 pandemic, we have not stopped our activities, while taking all safety precautions.

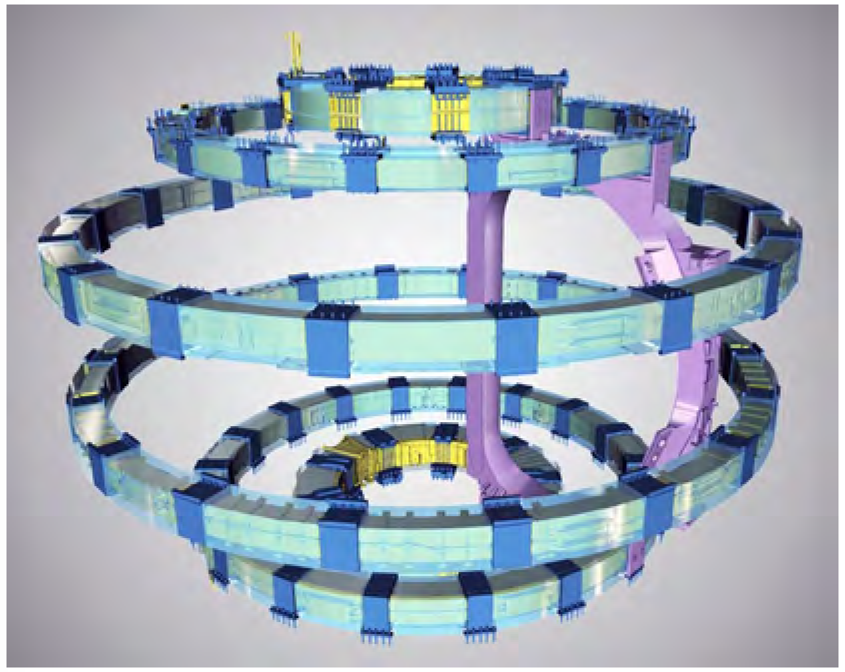

**Figure 1** Poloidal field coils of ITER with one toroidal field coil.

Once the manufacturing process is completed, each PF coil undergoes a test campaign inside a cryostat designed and produced for this purpose. While such tests are not performed at the final operating temperature, they nevertheless provide valuable information both to the manufacturing team and to the quality inspectors, and largely increase the general confidence in assembling the tested coils in its final position in the tokamak
Initially, before cooldown, a vacuum leak test and a pressure drop test of the helium cooling circuit are performed, together with an electrical DC current test and an electrical insulation (or Paschen) test of the ground insulation at room temperature.
If results of the preliminary tests are positive, the coil is cooled down to a temperature of 80 K, accordingly to the technical specifacation requirements where the following additional tests are performed and/or repeated: pressure drop test and vacuum leak test of the helium circuit, high voltage DC test and current test. Scope of the cold tests is to detect any possible malfunction that may appear after cooldown, that could originate e.g., from the different thermal contraction of materials.
At the end of the tests at low temperature, the coil is warmed up and the previous tests at room temperature are repeated.
All the PF coils will be tested in Cadarache by ASG Superconductors, inside the above-mentioned facility, following the technical specification issued by ASG.
To date, both PF6 and PF5 coils have been fully and successfully tested.

## The Cold Test Facility

The Cold Test Facility provides the set of equipment and machinery to perform the cold test of the PF coils at the target temperature of 80K. The facility has been designed to cool down the magnet while minimizing the risk of insulation breakage due to thermal contraction/expansion: for this purpose, the machine is able to decrease the temperature of the magnet with a maximum cooling rate of 1 K/h and can maintain the maximum instantaneous temperature difference between any parts of the coil to less than 50 K at all times during the cool-down and warm-up phases.
The Cold Test Facility (CTF) is composed of two main systems: the cryogenic plant and three cryostats to host the different size of the PF coils.
The cryogenic plant creates the pressurized cold helium gas flow that will circulate through the PF coils. The 80 K temperature regime is reached by passing helium gas through a heat exchanger in direct contact with liquid nitrogen at 77 K.
The cryogenic plant is also able to supervise the cooldown and acquire additional information by interfacing with auxiliary devices installed on both the cryostat and on the PF coil during the whole thermal cycle. An acquisition system monitors the data of temperatures, pressures, flows, etc..; a video recording system of 40 vacuum video-cameras monitors the coil under Paschen conditions; a leak detector performs leak testing of the coil at room and cold temperature and a power supply and electronics are used to measure the coil resistance by applying an electrical current of 500 A at low temperature.
The cryostats are stainless-steel vacuum chambers designed to host the coil and to reduce thermal losses during the test by conduction, convection and radiation. To mitigate these effects, the chambers employ thermal shields, superinsulation material, fiberglass supports and provide a vacuum level of 10^-5 mbar.
From a geometrical point of view, the dimensions of the cryostats have been determined by the size of the different PF coils, their diameter ranging from 12 m for the smallest PFs to 27 m for the largest ones Each cryostat is designed to withstand the coil weight (up to nearly 400 tons) and it is constructed out of modules of stainless-steel. The modules are joined together and welded, creating the complete donut-shape vacuum chamber that contains the coil during the tests.





**Figure 2** The dedicated area for the cryostats: On the right, the smaller cryostat is assembled and cold testing of the PF6 coil is in progress. On the left, the medium sized cryostat is about to be assembled for the final cold test of PF5.

## Cool down of the coils

As explained in the previous section, through the CTF we control the cooling rate and the temperature gradient along the coil. The coil is instrumented with Cernox and Pt100 thermometers and the electrical resistance of each double pancake is measured and converted into an average value of temperature.
The coils are cooled by a flow of He gas that is circulating along the cooling circuit of the coil, by means of temporary piping that connects the inlet and outlet of the coil to the valve box.
Two other circuits, in parallel with the main one, provide the He gas for cooling down the coil clamps and the thermal shield of the cryostat.

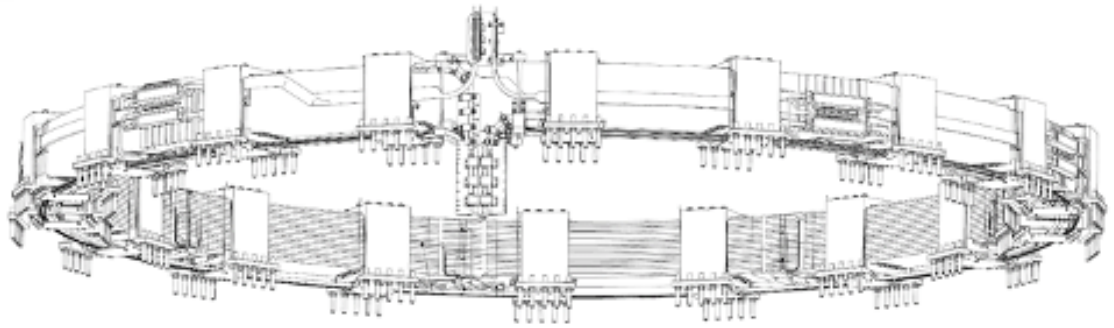

**Figure 3** PF5 isometric view.

The cooldown is controlled by the mass flow of helium which circulates in the circuits, and the nominal cooling rate stays between 0.8 and 1 K/h. Thus, for a cooldown of a coil to 80 K, about 13 days are needed, including an initial transient time and time for the final stabilization of the temperature.

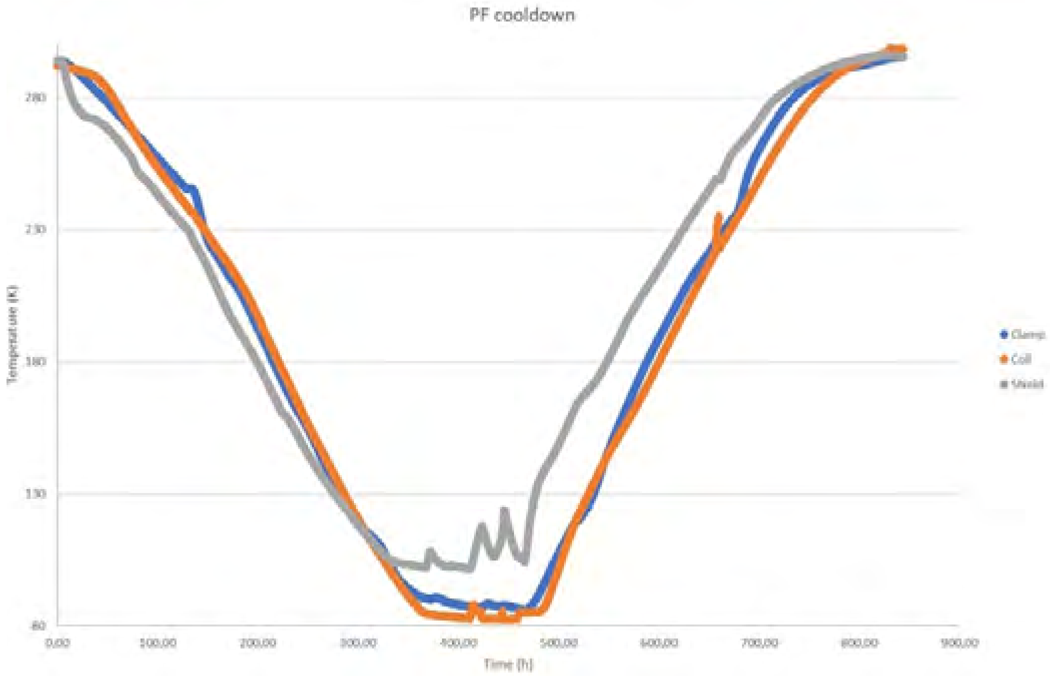


**Figure 4** Cooldown and warm up of PF6.

At the end of the tests at cold temperature, the coil is warmed up again controlled by the flow of He gas.





## Tests performed on the PF coils

Several tests are performed on each coil. The following tests are carried out at room temperature before and after the cooldown: pressure drop test, leak test, high voltage DC test and Paschen test.
The following tests are performed at 80K: pressure drop test, leak test, high voltage DC test and current test.

### Pressure drop test

The pressure drop test confirms the performance of the hydraulic circuit that is used to refrigerate the coil at cryogenic temperatures. Any leak, bottleneck, or increased friction against the cold helium flow would result in an increase in pressure drop. As the pressure drop is compensated by the cooling system, it cannot exceed certain values otherwise the coil will not be able to maintain the appropriate operating temperature.
In this experiment, a dry helium gas mass flow (g/s), which is circulated in the coil by a compressor, is set at different values so that the flow rate can be correlated to the difference between the measured inlet and outlet pressures (pressure drop). Indeed, the magnet offers a hydraulic impedance, an "opposition" to the helium flow and the higher the gas mass flow, the higher the pressure loss that will arise. This test is performed controlling the helium gas mass flow and monitoring the pressure of the gas which enters and exits the magnet through dedicated pipes. It is successfully passed when the results are compliant with research studies that can be found in literature, along with the results of previous tests performed on ITER superconducting magnets.

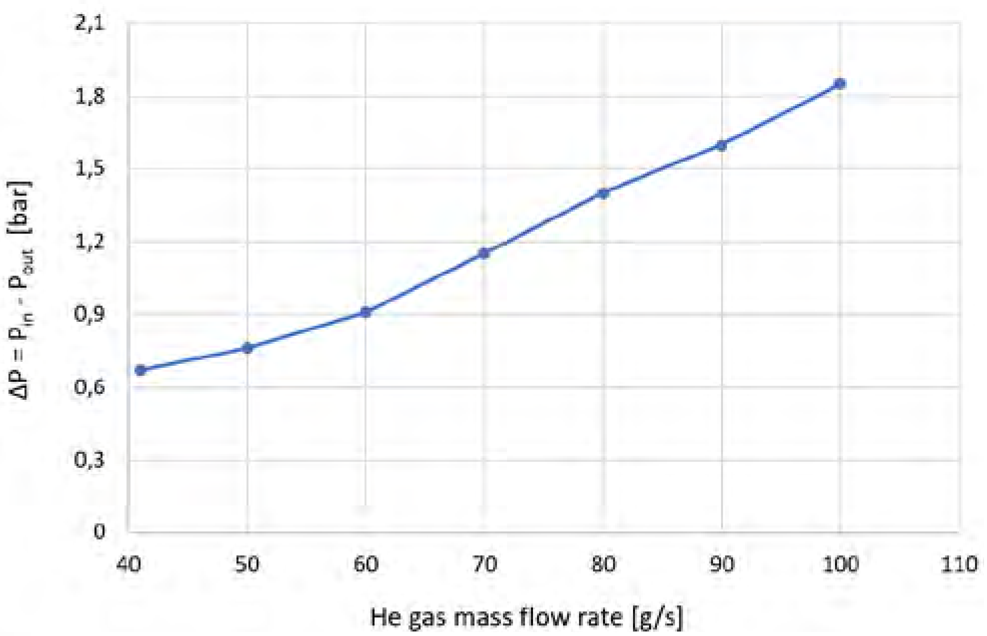


**Figure 5** Pressure drop test on PF6 after cool-down at 80 K.

## High voltage DC test

When the current in a superconducting magnet is ramping up and down, and in an unlikely case of a quench, a voltage appears on the superconducting coil. A high voltage DC test is therefore required to be sure that no significant leakage current appears through the electrical insulation material.
In this experiment, a maximum voltage of 15 kV is applied across the magnet, reaching this value after a ramp of about 17 V/s, and is held constant for 5 minutes. The test is passed if the insulation resistance at 15 kV is higher or at least equal to 500 MΩ, which corresponds to a leakage current lower than 30 µA.

## Leak test

The cooling process down to cryogenic temperature can produce considerable thermal stresses which can cause the formation of leaks. Therefore, it is necessary to perform a leak test before and after this process. First of all, the helium flow rate in the magnet is set to zero and its pressure is set to 15 bar. The leak rate measured at this pressure is then recorded by means of a helium leak detector which is connected to the cryostat. Given a certain volume, the helium leak rate provides a measurement of the change of pressure over time, due to the flow of some amount of the noble gas. Should a leak be present, helium would flow out of the magnet and its circuit and into the cryostat and would be measured by the leak detector.
Then, a calibrated leak into the cryostat is opened in order to check if a leak of known magnitude can be detected and correctly measured. Subsequently, the calibrated leak is closed and the helium inside the coil is pressurized at 30 bar. After waiting for one hour in this configuration, the leak rate is measured again, and then the calibrated leak is opened. The helium leak rate measured at 15 bar is then subtracted from the rate at 30 bar and if the result is lower than $10^{-6}$ mbar*l/s the test is passed successfully.





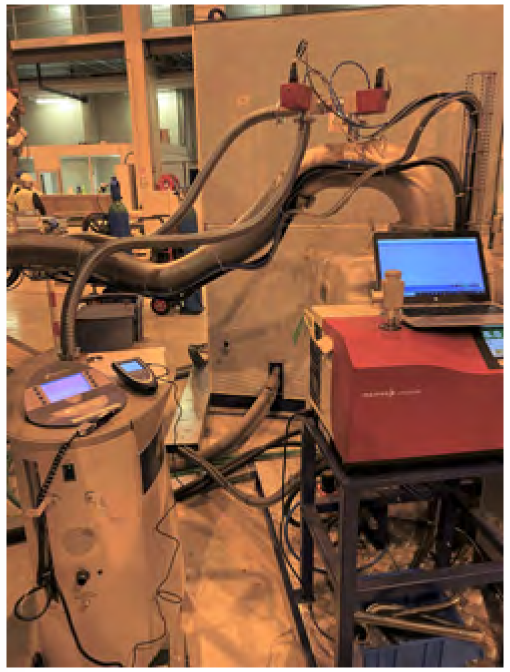

**Figure 6** Leak detector, on left side, and vacuum pumping system connected to PF5 cryostat.

## Current test

The current test is undertaken to ascertain the homogeneity of the electromagnetic architecture of the superconducting coil.
This test, performed only at low temperature, consists of feeding the coil with 500 A and recording, from the voltage taps that are installed on the coil, the voltage drops across each double pancake. The voltage drop across a shunt resistor is also measured in order to calculate the actual current flow in the coil. All these signals are then acquired using a fast acquisition measurement device at a sample rate of around 100k sample/s. The results are analysed and the test is considered successful if the modulus of the difference between the resistances of each double pancake is lower than 5%.

## Paschen Test

In order to minimize the probability of an electrical breakdown at operating voltage, for example in case of an accidental pressure-rise, the electrical equipment has to be Paschen-tight, meaning that no breakdown may occur across a range of pressures.  Figure 7 shows the heavy dependance of the breakdown voltages of various gases on the product of the gas pressure and the distance between two electrodes at different electric potential.

The Paschen test is performed at room temperature before and after cooldown.
A DC high voltage is applied to the coil at different levels of nitrogen gas pressure from 10-2 mbar to 100 mbar in the cryostat. At each pressure step, a voltage of 15 kV is applied for 1 minute. An electrical breakdown would cause an increase in the leakage current, detected by the high voltage generator and a flash, hopefully located by the cameras in the cryostat. The criteria for passing the test are having a leakage current lower than 20 µA and not observing any discharge.
Once this last test is passed after the cooldown and warm-up, the cold testing of the coil is completed and the magnet is ready for the final operations before being delivered to ITER for assembly in the tokamak.

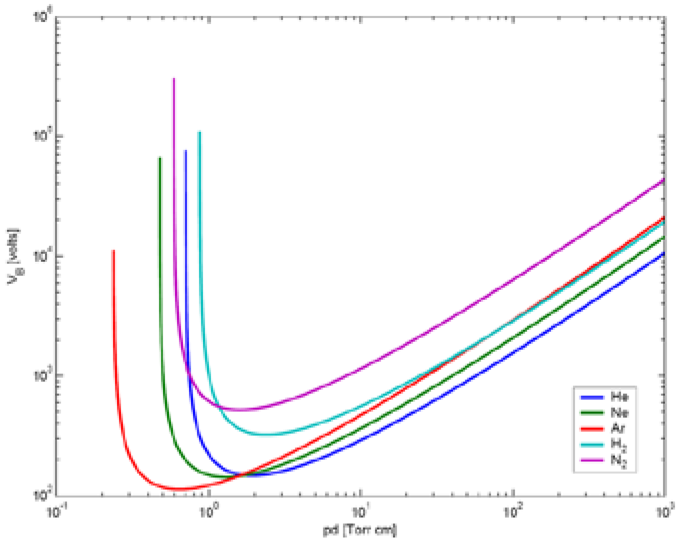


**Figure 7** Paschen curves for different gases. He and N2 plots are relevant f or the tests on ITER superconducting magnets.

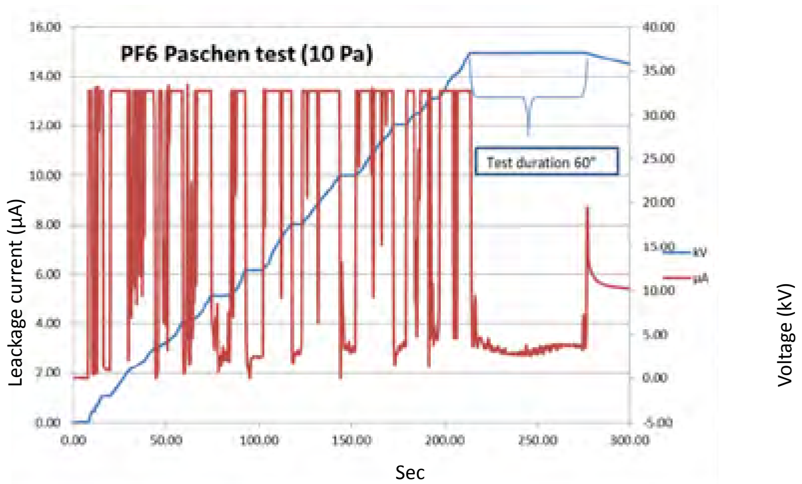


**Figure 8** : Paschen tests on PF6.





## Conclusions

The poloidal field coil cold test represents an exciting moment for the ASG team to verify that the lengthy manufacturing work of the huge superconducting systems was carried out successfully.
The cold tests on the PF6 confirmed the integrity of the coil, which passed all the tests carried out. The tests performed so far on the PF5 have also been successfully passed. The Cold Test Facility operated correctly during all the phases of the activity, with no noteworthy problems. The activities have been supervised 24 hours a day by the ASG team, both on-site and remotely, with support from Fusion for Energy and other personnel.
This activity was made possible by a remarkable effort of coordination and teamwork between different entities from all around the world with a common goal: to build the ITER device.

# JT-60SA TOROIDAL FIELD COILS

# JT-60SA TOROIDAL FIELD COILS (TFC) MANUFACTURE

Giovanni Drago

The assembly of the tokamak was completed in 2020 and at the end of the same year also the cooldown was executed; on 02/03/2021 the complete toroidal system was fed up to the nominal current of 25.7 KA.

JT-60SA is a superconducting tokamak machine designed to contribute to the early realization of fusion energy by supporting the exploitation of ITER and research toward DEMO by addressing key physics issues, installed at Naka site in Japan.

The Italian Atomic Energy Agency ENEA awarded the contract for the manufacture of 10 Toroidal Field Coils (9+1 spare) for the JT-60SA project to ASG Superconductors.

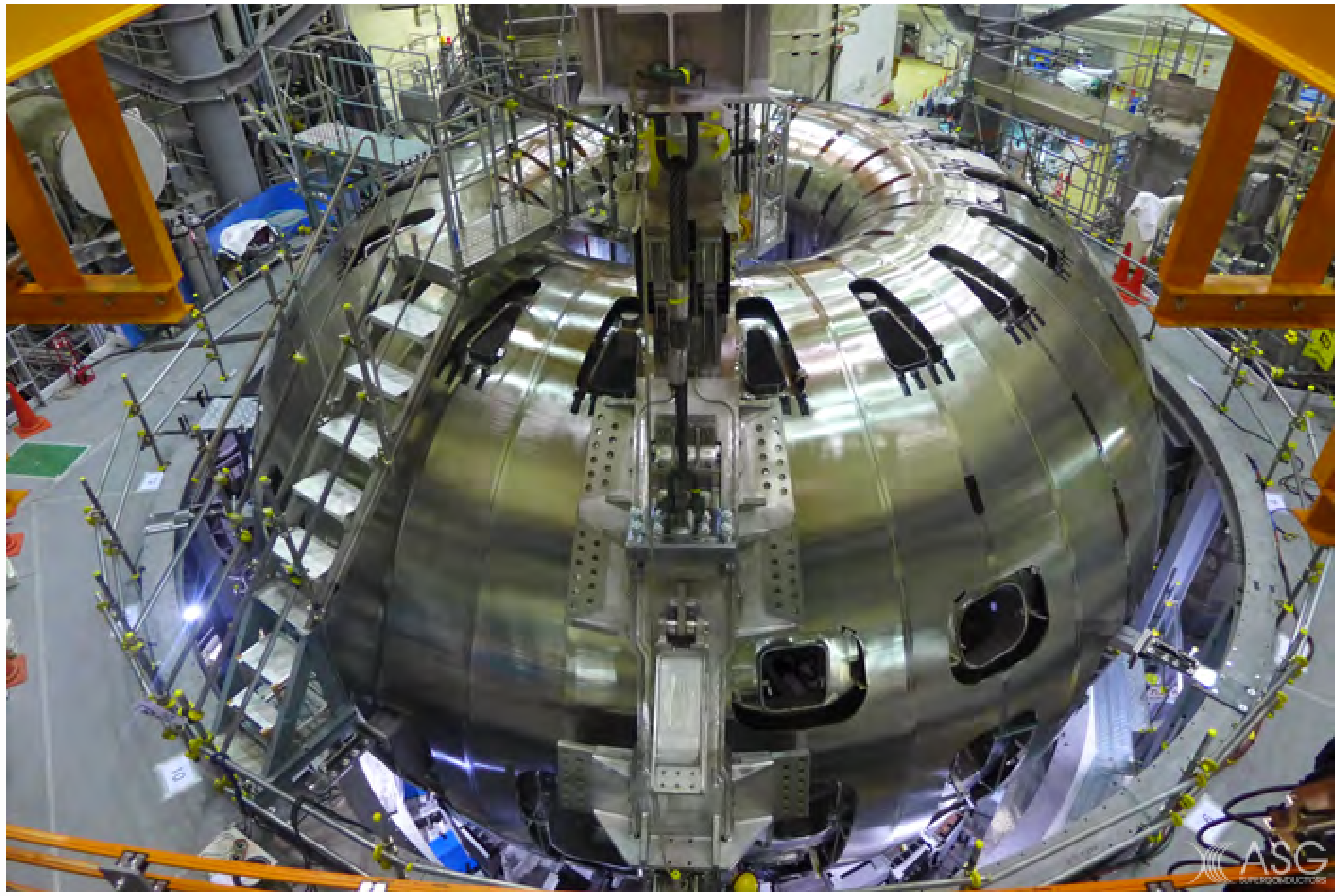

Insertion of the last coils in the machine (Courtesy of JAEA)

## Introduction

In 2011 under the framework of the Broader Approach Agreement between the European Atomic Energy Community and the Government of Japan, the Italian Atomic Energy Agency ENEA awarded the contract for the manufacture of 10 Toroidal Field Coils (9+1 spare) for the JT-60SA project to ASG Superconductors. The manufacture of the remaining 10 TF coils necessary for the project was managed by the French Atomic Energy Authority.
The superconducting tokamak machine at the Naka site in Japan is designed to contribute to the early realization of fusion energy by supporting the exploitation of ITER and research toward DEMO by addressing key physics issues.
To achieve this, JT-60SA is designed to be completely superconducting and thus able to produce 100 s long shots with a plasma current IP of about 5.5 MA.
The toroidal magnetic system is composed of eighteen D-shaped coils, wound using NbTi conductor, capable of generating a maximum field of 2.25 T on the central axis of the plasma and a maximum field of 5.65 T at the innermost equatorial plane of the coil straight leg. The modules are operated at a temperature of 4.4 K with a theoretical temperature margin of 1 K. They are energised by a current of 25.7 kA.





## Coil description

Each coil is manufactured starting from a CIC (Cable in Conduit conductor consisting of a Cu-NbTi strands rope (strand diameter Ø=0.81 mm) wrapped with a thin stainless-steel band and inserted in an AISI 316L stainless steel jacket 2 mm thick. The overall conductor dimensions are 22.0 × 26.0 mm with a void fraction of 32%.

**Figure 1, 2, 3** Details of the JT-60SA conductor

The conductor is wound in D-shaped Double Pancakes (DP) consisting of two layers of 6 turns each, insulated by means of two wrappings of half-overlapped fiberglass tape.
After winding, 6 DPs are stacked together to form the Winding Pack (WP) of each coil. The WP cross-section dimensions are 150 × 347 mm with overall width of ~5 m and length of ~8.2 m including the electrical joints between DPs and terminations.
Once the WP has been assembled and ground insulated using fiberglass tape, it is impregnated with epoxy resin inside a vacuum tight case assembled and welded all around the winding.
Then the WP is inserted into a thick stainless-steel casing able to contain all the magnetic forces acting on the conductor during operation. The total weight of the coil is ~16 tons.

Process qualification and manufacturing tooling procurement
During the first year of the project activities were focused on the following three different tasks:

a) Definition of the detailed manufacturing plan and preparation of detail drawings of the relevant components.
b) Conceptual design and development of the tooling for the WP and TFC manufacturing.
c) Preparation of samples and mock-up for the validation of the design and process qualification to verify that the envisaged procedure meets the main design requirements.

Design Validation
The most important process to be qualified is the turns insulation, consisting of fiberglass tape impregnated with epoxy resin, required to meet stringent requirements in terms of shear strength derived from the calculated mechanical forces acting between the turns.
The performance of the insulation in terms of ultimate shear strength and capability to withstand the cyclic loading has been evaluated on standard samples, comprising two stainless-steel plates separated by fiberglass epoxy resin, simulating the inter-turn insulation. The sample were tested both at room temperature and at 4 K as well as under fatigue conditions and were shown to meet the following requirements:

— minimum shear strength capacity after impregnation of 55 MPa at 4 K, corresponding to 40 MPa at 300 K
— minimum shear strength capacity after 36,000 cycles of 20 MPa at 300 K

The following show the shear strength sample under test:

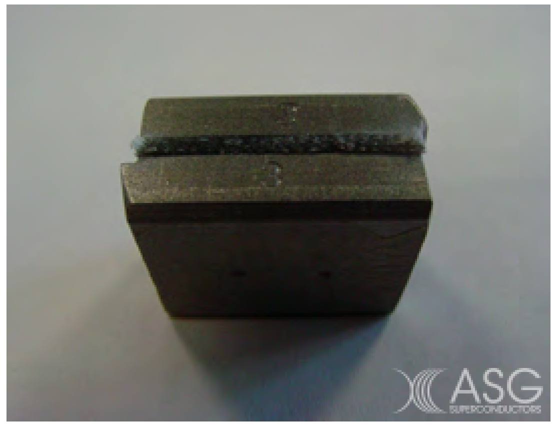

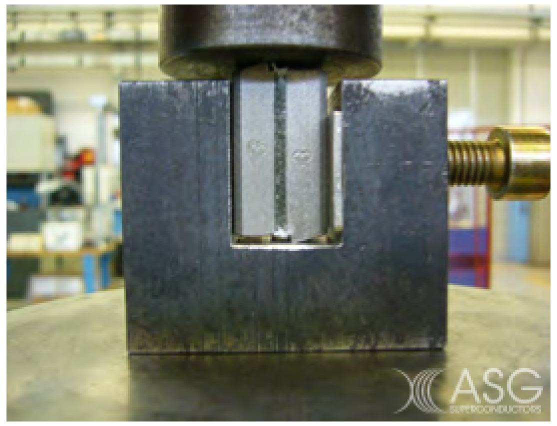


**Figure 4, 5** Shear Test Sample / Shear test sample during testing

The insulation and impregnation processes were also validated by the manufacture of a 1 m impregnation beam, using straight stainless steel bars to represent the WP cross section. The beam was assembled, insulated and VPI impregnated and then submitted to electrical test to verify that all the requirements for the insulation were satisfied.
The ground insulation was successfully tested up to 15 kV, while the turns insulation reached 10 kV. In both cases, no faults were detected.
The following show the impregnation beam already painted with conductive varnish for grounding:

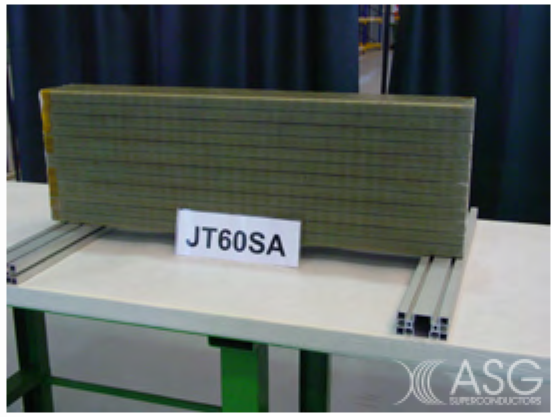

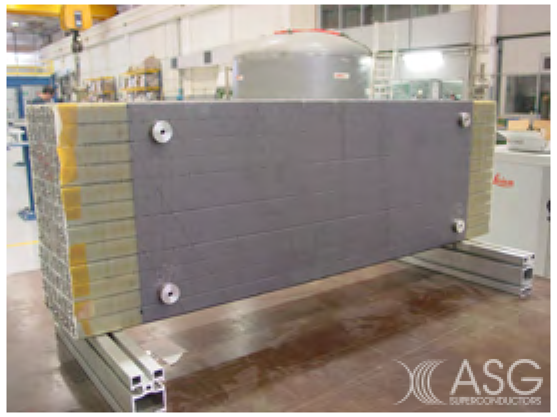


**Figure 6, 7** Impregnation Beam / Impregnation Beam with grounding paint and reference markers

The impregnation beam was used also for the qualification of other processes: as a first step it was instrumented with thermocouples and inserted into the coil casing mock-up to verify that the temperature increase during the casing welding was not high enough to damage the resin of the impregnated WP.
Then, after welding, the mock-up was submitted to a second impregnation cycle in order to simulate the embedding impregnation.
The mock-up cut after the impregnation is shown in the following images:


**Figure 8, 9** Impregnation Beam inside casing mock-up / Casing mock-up cut after embedding impregnation

Another important process to be qualified was the manufacture of the internal joints which provide the electrical junction between different DPs of the coil. The joints are realized following the "praying hands" concept based on the configuration where the two conductors forming the joint are coming from the same side of the coil. The conductors are inserted into a pre-machined junction box made from a three-layer (stainless steel – copper – stainless steel) explosion bonded plate, pressed against the low resistance copper intermediate plate and compressed by the stainless-steel covers which are welded to the main body of the box.
The electrical resistance of the joint at 4 K had to be less than 5 nΩ.
To guarantee the low resistance of the joint, silvering of the inner surface of the box as well as the end portion of the conductor rope is necessary and several trials and mock-ups were required to define the silvering process parameters. The joint sample shown in the following figure was tested by ENEA with positive results:

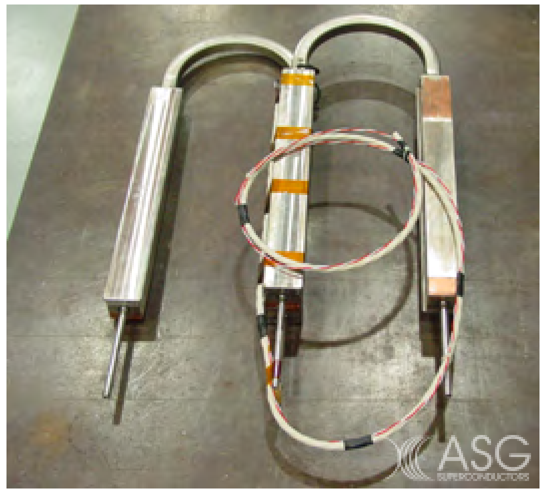

**Figure 10** Full size joint sample tested by ENEA

## Manufacturing tooling

In parallel with the mock-ups and process qualification work, the conceptual design of the main tooling was performed followed by the procurement and installation of the main tooling for the manufacture of the coils.
The most critical item was the winding line which is composed of different units assembled and synchronized to perform the DP winding. In detail the line is equipped with an unwinding spool which supplies the conductor necessary for the winding, a straightening unit to remove any residual bending present on the conductor, a cleaning unit, a calendaring unit to bend the conductor to the required radii, a sandblasting unit, a taping unit and finally a winding table which hosts the bent conductor.





The unwinding spool and the winding table are shown below:

**Figure 11, 12** Winding Line-Unwinding spool / Winding Line-Winding Table

Another important tool necessary for manufacturing the WPs is the impregnation station which consists of a steel framework equipped with several modules able to allow the thermal expansion of the WP during the impregnation cycle. The framework can be tilted along the longitudinal side to ease the resin flow during impregnation. Each module is equipped with frames to transfer to the WP the force to compact the insulation and with heating elements to regulate the temperature of the coil during the process.

**Figure 13** Impregnation station

The integration of the WP inside the casing required the design of a specific tool able to support the WP during the assembly of the casing parts and to tilt the final assembly to a vertical position in which to perform the casing welding to achieve annular containment of the whole surface of the WP. A challenging aspect of the design of this tool was the small gap between the WP and the casing, being only 5 mm, which strongly influenced the design of the WP supports. The dimensions and loads of the tilting toll required verification of the floor capacity.

**Figure 14** Assembly and tilting tool

## Manufacturing plan

The Toroidal Field Coil (TFC) manufacturing was divided into two steps – one for each of the main components supplied by ENEA: the conductor for the winding and the stainless-steel casing for the final assembly of the coil. At the end of each manufacturing step, a complete acceptance test was performed.

### WP manufacturing

The first step is the WP manufacturing which starts with the conductor acceptance test to assess the conductor tightness. The conductor supplied as a single layer solenoid was inserted into the vacuum chamber to perform the pressure/leak test, evacuating the chamber and pressurizing the conductor. All the conductor lengths tested showed a leak rate lower than $2 \times 10^{-9}$ mbar*l/s as required by the specification. After the test, the conductor is transferred to the winding line for the DP winding operations: the conductor is first straightened to remove the previous bending deformations, then it passes through the cleaning unit to clean the jacket surface by means of detergent and ultrasound bath.

The next equipment of the line is the bending unit which, by means of plastic deformation, gives to the conductor the required curvature radii for the DP. Once the conductor is bent, the sandblasting unit gives to the conductor surface the roughness necessary to ensure good adhesion of the insulation (fiberglass and resin). This unit represented the most challenging set up, due to the need to operate on a low curvature radius of the turns in the transition region from the straight part to the outer region of the coil. The next unit is the taping machine which applies to the sandblasted conductor the fiberglass tape to realize the turn insulation. Finally, the wound turns are transferred to the winding table.

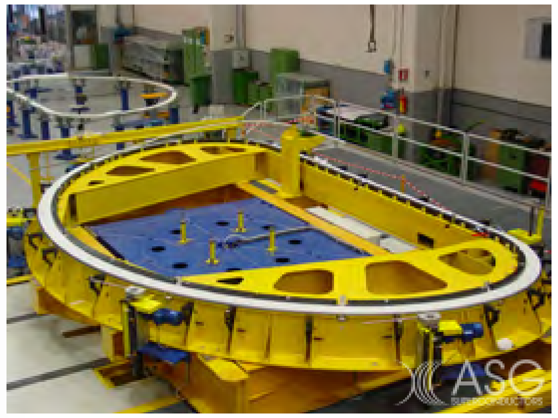

**Figure 15, 16** DP winding completed / Winding of DP 2nd layer

Once the winding operations have been completed the DP is moved by means of the lifting tool to the DP insulation station where several operations are completed: bending the DP leads, removing the jacket and silvering the superconducting rope for the next joints, and applying the DP insulation.
The completed DP is then moved to the stacking station where six DPs forming the WP are stacked together; in this phase, checking and adjustment of the alignment is performed. After stacking, the ground insulation is manually applied by wrapping the WP with several tapings up to the final thickness of 3 mm. A further check on shape and dimensions is performed prior to moving the WP to the impregnation station. The requirements in terms of tolerances were quite demanding especially in terms of the overall dimensions of the WP: on the cross-section of the coil the tolerances are ±3 mm on the width and ±5 mm on the height and referred to the coil dimensions (4370 × 7330 mm) these represent 0.04 & 0.06 %. In addition, the most stringent requirement is set on the centerline of the WP straight part which has to stay inside a cylinder of Ø2 mm.

**Figure 17** DP stacking

After application of the ground insulation the WP is moved to the impregnation station where it is inserted inside the impregnation mold which consists of a thin stainless-steel casing split into two halves which are welded all around the WP to realize the resin containment. During this operation the shape of the WP is checked by means of the Laser Tracker to control the alignment within the prescribed tolerances.
Moreover, after the welding and prior to starting the process cycle, the tightness of the casing is verified to ensure that the the maximum leak rate is not exceeded. The ground insulation of the WP is checked and the mold is used as a vacuum vessel to check the leak rate on the conductor and internal joints/terminations.
Once the mold has been checked, the VPI impregnation cycle can be executed performing all the different phases controlling the temperature vs. time as well as all the other parameters. The whole impregnation cycle, including the preliminary heating, the ramping up and down to the different temperatures and the final cool down to room temperature (RT) lasts about 12 days.
After the VPI cycle the WP impregnation casing is dismantled and the WP is cleaned before the application of the conductive varnish to realize the electrical grounding.

**Figure 18, 19** WP VPI impregnated / WP after grounding varnish application





On the completed WP the intermediate acceptance tests are performed, executing a complete dimensional survey and referring the results, especially the centerline position, to the reference points (12 in total) glued on the inner surface of the WP. These reference points are used for the next assembly operation and for the final interface machining.
In addition, hydraulic tests on the conductor circuit are performed inside a dedicated vacuum chamber: pressure/leak test is performed by pressurizing the conductor up to 30 bar and measuring the leak rate with respect to the chamber, then a flow test is carried out to verify that during the impregnation no obstruction of the conductor circuit occurred.
While the WP is inside the vacuum chamber, Paschen tests comprising consisting of High Voltage tests in a gas atmosphere at different vacuum/pressure conditions are also performed. These are executed in N2 gas at different pressure steps from vacuum (10-3 mbar) to 100 mbar. At each step a voltage of 3.8 kV is applied to the conductor to test the electrical tightness of the insulation.
Finally, the standard electrical test (inter-turn and ground insulation) and measurements (Resistance and Inductance) are executed.
This test campaign releases the WP for the next manufacturing stages.

**Figure 20** WP introduction into Vacuum chamber for testing

## TFC manufacturing

The second step is the TFC manufacturing which starts with the insertion of the WP inside the stainless-steel casing which consists of two main "C" shaped parts 50 mm thick to be assembled and welded to provide containment around the outer surface of the WP. The inner closure is ensured by 20 mm covers that have later to be welded to the "C" shaped parts. For the insertion of the WP inside the casing, only a small clearance is provided: this small 5 mm gap requires that the dimensions and tolerances both of the WP and the casing are well respected to allow the assembly. Due to the precision achievable on the WP following resin impregnation being lower than the precision of the casing components obtained by mechanical machining, the gap is not constant all around the WP surface. For this reason a fiberglass cloth to be further impregnated has been chosen as the filling material, the thickness of which was determined by means of a full geometrical survey both of the coil and the casing. Firstly, the two parts of the casing are installed on the carriages while the WP is positioned on the inner core of the tilting tool. Secondly, the assembly of all the components is performed. Finally the assembly is tilted into a vertical position to allow the execution of the welding between the two parts of the casing. Once the transversal welding has been completed, the coil is tilted again into a horizontal position and moved onto supports for the installation and welding of the inner covers.


**Figure 21, 22** WP and coil casing onto the assembly tooling / Assembly tilted in vertical position for welding execution

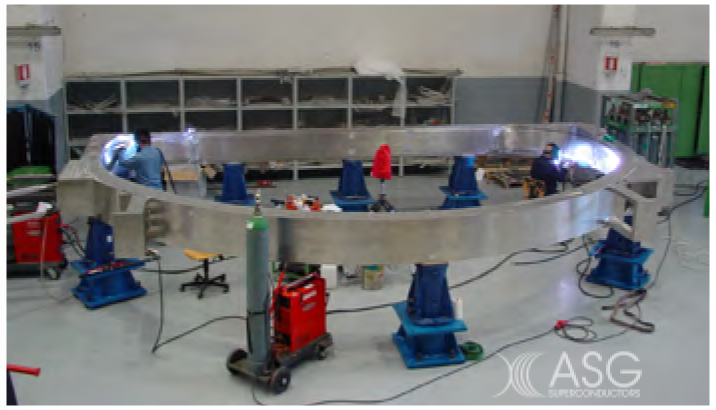

**Figure 23** Cover welding

After the casing welding, the coil is ready for the embedding impregnation of the fiberglass in between the WP and the casing to secure the WP position with respect to the casing. For this VPI impregnation the casing acts as a mold ensuring the tightness for the resin injection and only the blanking of some openings, for example the reference point on the inner surface, is necessary.
A complete dimensional survey follows the embedding impregnation to define the reference planes to be used for the final interface machining. These reference planes are defined by the position of the centerline of the straight leg and are characterized with respect to the reference point of the WP. During the machining other references on the outer surface of the coil are added to allow the final installation. The final machining operations have been commissioned to an external company which performed the activity under ASG responsibility and supervision.

**Figure 24** TFC interface machining (courtesy of Officine CLP)

After machining the coils were returned to the ASG premises for completion, comprising the routing, welding and insulation of the cooling circuit as well as the installation and routing of instrumentation. Once the coil has been completed all the acceptance tests were performed and attended by ENEA and the leak/pressure test was also attended by a certified third party.

**Figure 25** TFC completed





## Coil testing and installation

All the JT60-SA TF coils were successfully tested at the CEA site (near Paris). The test was carried out at cold condition feeding each coil up to the full current of 25.7 kA, including an induced quench obtained by reducing the LHe flow. After the testing, before the shipment to Japan, the OIS (Outer Interface Structure) which represents the mechanical interface between two adjacent coils inside the machine was assembled. Both the testing and OIS assembling activities were in charge to Fusion For Energy. Performed under responsibility and supervision of the European Agency for Fusion (F4E-Fusion for Energy)

The assembly of the tokamak was completed in 2020 and at the end of the same year also the cooldown was executed; on 02/03/2021 the complete toroidal system was fed up to the nominal current of 25.7 KA.

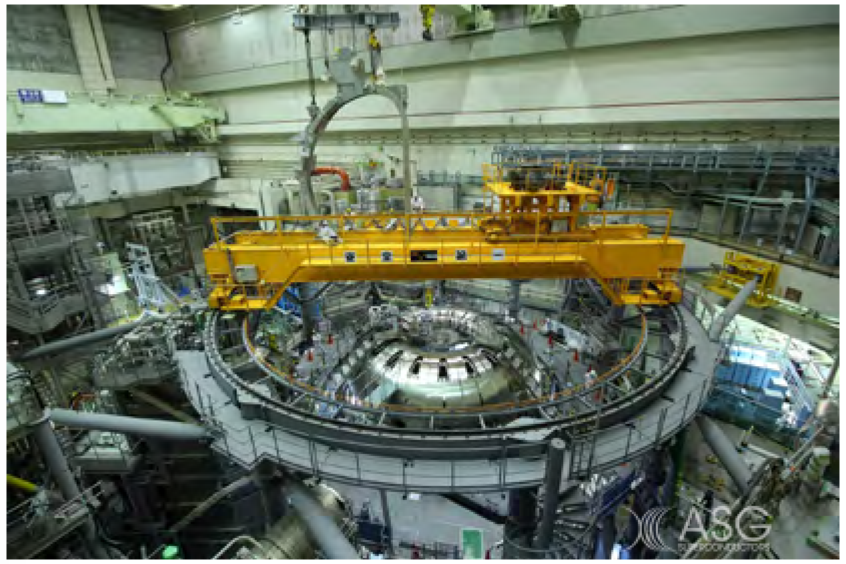

**Figure 26** TFC assembling on the machine (Courtesy of JAEA)

**Special thanks to ENEA, Fusion For Energy and all ASG Superconductors team who made it possible to complete this important project.**

# ITER PF6 COLD TEST

All pictures courtesy of ITER





# PF6 COLD TESTED AT TEMPERATURES SIMILAR TO PLUTO

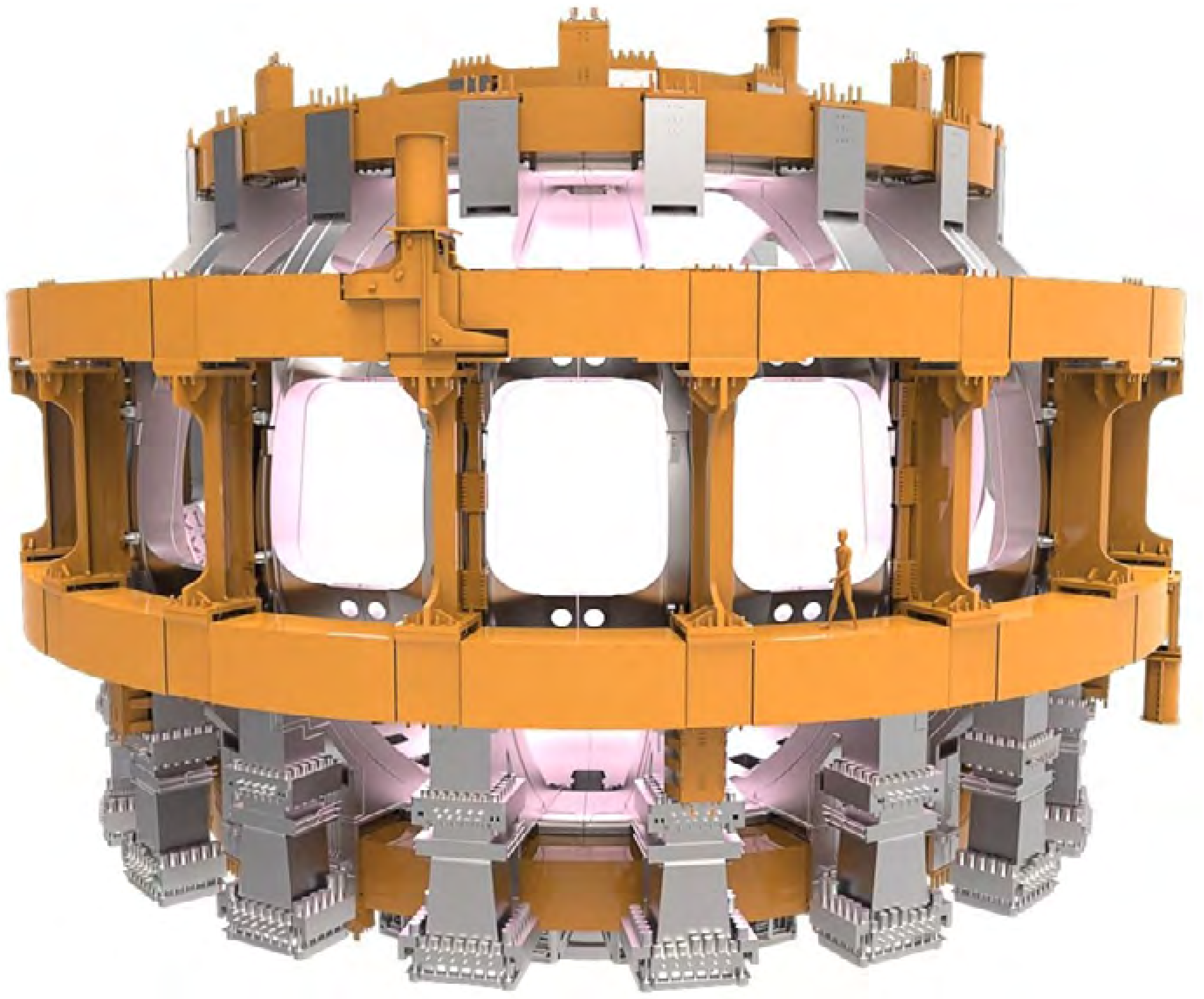

In the coming months ASG Superconductors will celebrate several important milestones for the production of the poloidal field coils that will be part of the biggest fusion device - ITER.
Seven parties are building the biggest Tokamak machine to test fusion energy through magnetic confinement.
This experiment will allow scientists to study a "burning plasma" that will produce a greater thermal output (500 MW).
Due to their large sizes, i.e. 17 and 24 m diametre, four of the six PF coils are manufactured on-site (Cadarache), in a dedicated workshop under the supervision of Fusion For Energy. Once ready they will be handed over to ITER Organization for their assembly.
The PF coils will be positioned horizontally around the ITER vacuum vessel, and the 18 D-shaped toroidal field coils, to control the shape and stability of the plasma.

At the end of January, the sixth poloidal field coil left the factory and was put into storage until assembly. It was manufactured jointly by F4E and ASIPP (China). Then, it was cold-tested at 80 K by ASG and F4E. A temperature similar to Pluto - the furthest and smallest planet in our Solar system.





In April, the fifth poloidal field coil will be completed. It's the first to be entirely manufactured on-site.
The first part of its production has been performed by CNIM following ASG Superconductors manufacturing procedures and drawings, constantly under our and F4E's supervision.

The insertion into the tokamak pit of the sixth and fifth coils, will pave the way for an important ITER milestone: the start of TF (Toroidal Field) coil assembly inside the Tokamak building, where the machine will be housed.

This year the second poloidal field coil will be delivered.
Its diameter is around 17 m.
In the meantime, the fourth poloidal field coil is in progress, with a diameter of around 24 m.

Together with Fusion for Energy and the other companies, we continue to work every day for fusion energy.
We will keep you informed on the progress of the biggest international partnership that will bring the power of the Sun to Earth.

#ITER #magnets #pfcoils #tokamak #coldtest #f4e #manufacturing #innovation #fusionenergy

# FERMILAB MU2E TS

TS Overall layout (assembly at Fermilab premises)
Photo Courtesy of Fermilab)





# TRANSPORT SOLENOID (TS) MAGNET SYSTEM FOR THE Mu2e EXPERIMENT AT FERMILAB

Alberto Barutti, Simone Meneghetti, Adriano Parodi, Luca Pastorino,
Alessandro Scimone, Franco Terzi, Nicolò Valle

The Fermilab Mu2e experiment seeks to measure the rare process of direct muon to electron conversion in the field of a nucleus. The magnet system for this experiment is made of three warm-bore solenoids: the Production Solenoid (PS), the Transport Solenoid (TS – the one provided by ASG), and the Detector Solenoid (DS). The Transport Solenoid is a "S-shaped" solenoid Magnet System placed in between the other bigger solenoids (DS & PS). It has a warm-bore aperture of 0.5m and produces a field varying in between 2.0 and 2.5 Tesla. The strong coupling with the adjacent solenoids poses several challenges to the design and operation of the Transport Solenoid. The main goal of the Transport Solenoid is to transport the muons created by a proton beam hitting a target inside the PS, selecting the muons by charge and momentum and carrying the required slow muons to the detector after some time delay.

These goals are achieved by the S-shape of the Transport Solenoid, a set of field characteristics including negative gradients in the straight sections, and collimators set in the warm bore, which is the muon beam line. The Transport Solenoid is made of three straight sections (TS1, TS3 and TS5) housing the collimators and two toroidal sections (TS2 and TS4) making 90° bends in opposite directions. The half-coils of TS3, together with the TS1 and TS2 coils are set in a single cryostat (TSu). Similarly, all other coils are set in the TSd cryostat.

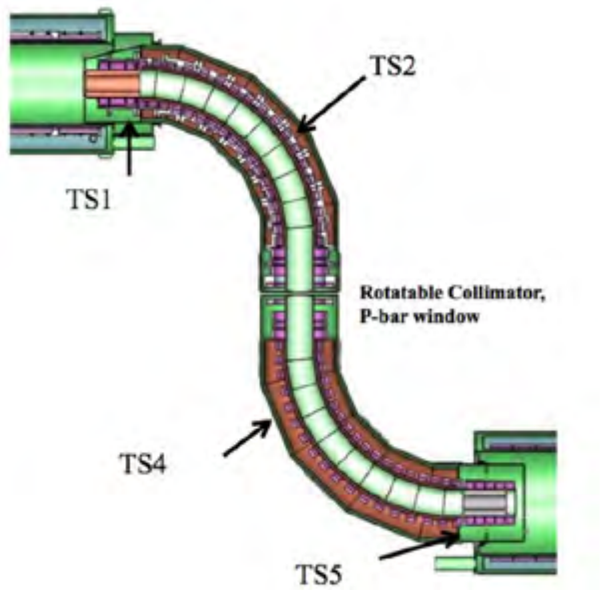


**Figure 2.** TSu & TSd detailed layout

The Transport Solenoid system consists of 52 superconducting solenoid coils integrated into 27 Modules that form 14 Units. The entire assembly composes the so-called "S-shaped" structure. The TSu cryostat contains the TS1, TS2 and TS3u coils while the TSd cryostat contains the TS3d, TS4 and TS5 coils.

**Table 1** below summarizes the Modules and Coils for the two TSu and TSd sub-assemblies:

| TS | Test Unit | Module | Coil # | Layers | Turns/layer | Turns |
|---|---|---|---|---|---|---|
| TSu | TSUN-6 | TSMD-1 | TSCL01 | 5 | 16 | 80 |
| | | | TSCL02 | 8 | 25 | 200 |
| | | TSMD-2 | TSCL03 | 11 | 15 | 165 |
| | TSUN-4 | TSMD-3 | TSCL04 | 12 | 17 | 204 |
| | | | TSCL05 | 12 | 17 | 204 |
| | | TSMD-4 | TSCL06 | 12 | 17 | 204 |
| | | | TSCL07 | 16 | 17 | 272 |
| | TSUN-3 | TSMD-5 | TSCL08 | 16 | 17 | 272 |
| | | | TSCL09 | 16 | 17 | 272 |
| | | TSMD-6 | TSCL10 | 16 | 17 | 272 |
| | | | TSCL11 | 17 | 17 | 289 |
| | TSUN-1 | TSMD-7 | TSCL12 | 17 | 17 | 289 |
| | | | TSCL13 | 17 | 17 | 289 |
| | TSUN-2 | TSMD-8 | TSCL15 | 17 | 17 | 289 |
| | | | TSCL14 | 18 | 17 | 306 |
| | | TSMD-9 | TSCL16 | 18 | 17 | 306 |
| | | | TSCL17 | 18 | 17 | 306 |
| | TSUN-5 | TSMD-10 | TSCL18 | 18 | 17 | 306 |
| | | | TSCL19 | 18 | 17 | 306 |
| | | TSMD-11 | TSCL20 | 20 | 17 | 340 |
| | | | TSCL21 | 12 | 17 | 204 |
| | TSUN-7 | TSMD-12 | TSCL22 | 16 | 17 | 272 |
| | | | TSCL23 | 13 | 8 | 104 |
| | | TSMD-13 | TSCL24 | 15 | 17 | 255 |
| | | | TSCL25 | 43 | 8 | 344 |
| TSd | TSUN-13 | TSMD-14 | TSCL26 | 42 | 8 | 336 |
| | | | TSCL27 | 13 | 17 | 221 |
| | | TSMD-15 | TSCL28 | 14 | 8 | 112 |
| | | | TSCL29 | 14 | 17 | 238 |
| | TSUN-12 | TSMD-16 | TSCL30 | 10 | 17 | 170 |
| | | | TSCL31 | 12 | 17 | 204 |
| | | TSMD-17 | TSCL32 | 12 | 17 | 204 |
| | | | TSCL33 | 15 | 17 | 255 |

| TS | Test Unit | Module | Coil # | Layers | Turns/layer | Turns |
|---|---|---|---|---|---|---|
| TSd | TSUN-9 | TSMD-18 | TSCL34 | 15 | 17 | 255 |
| | | | TSCL35 | 15 | 17 | 255 |
| | | TSMD-19 | TSCL36 | 15 | 17 | 255 |
| | | | TSCL37 | 16 | 17 | 272 |
| | TSUN-8 | TSMD-20 | TSCL38 | 16 | 17 | 272 |
| | | | TSCL39 | 16 | 17 | 272 |
| | TSUN-10 | TSMD-21 | TSCL40 | 16 | 17 | 272 |
| | | | TSCL41 | 16 | 17 | 272 |
| | | TSMD-22 | TSCL42 | 16 | 17 | 272 |
| | | | TSCL43 | 16 | 17 | 272 |
| | TSUN-11 | TSMD-23 | TSCL44 | 16 | 17 | 272 |
| | | | TSCL45 | 14 | 17 | 238 |
| | | TSMD-24 | TSCL46 | 14 | 17 | 238 |
| | | | TSCL47 | 11 | 17 | 187 |
| | TSUN-14 | TSMD-25 | TSCL48b | 9 | 14 | 126 |
| | | | TSCL49b | 8 | 14 | 112 |
| | | TSMD-26 | TSCL50b | 5 | 14 | 70 |
| | | TSMD-27 | TSCL51 | 3 | 14 | 42 |
| | | | TSCL52 | 3 | 14 | 42 |

All the TSu/TSd coils are powered in series, thereby minimizing the number of leads and the complexity of the powering and protection systems.
The coils are pre-assembled as modules and tested at 4K in order to reduce the complexity and the time of the assembly.
The support system is optimized to facilitate control of the interfaces and to reduce the stresses during cooldown and warm-up.





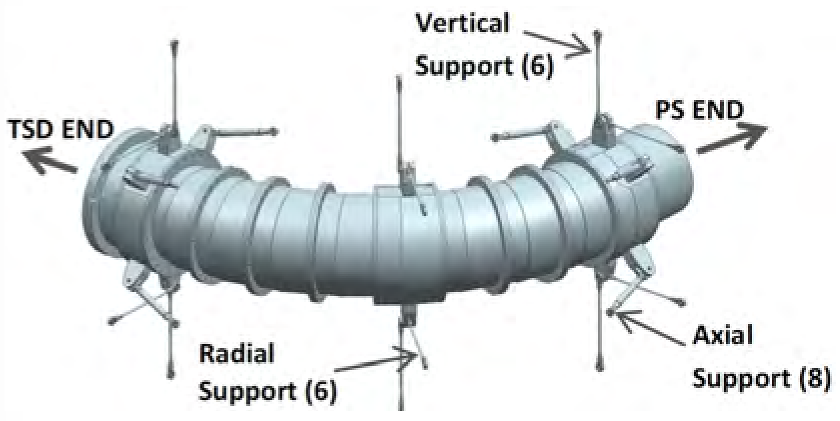


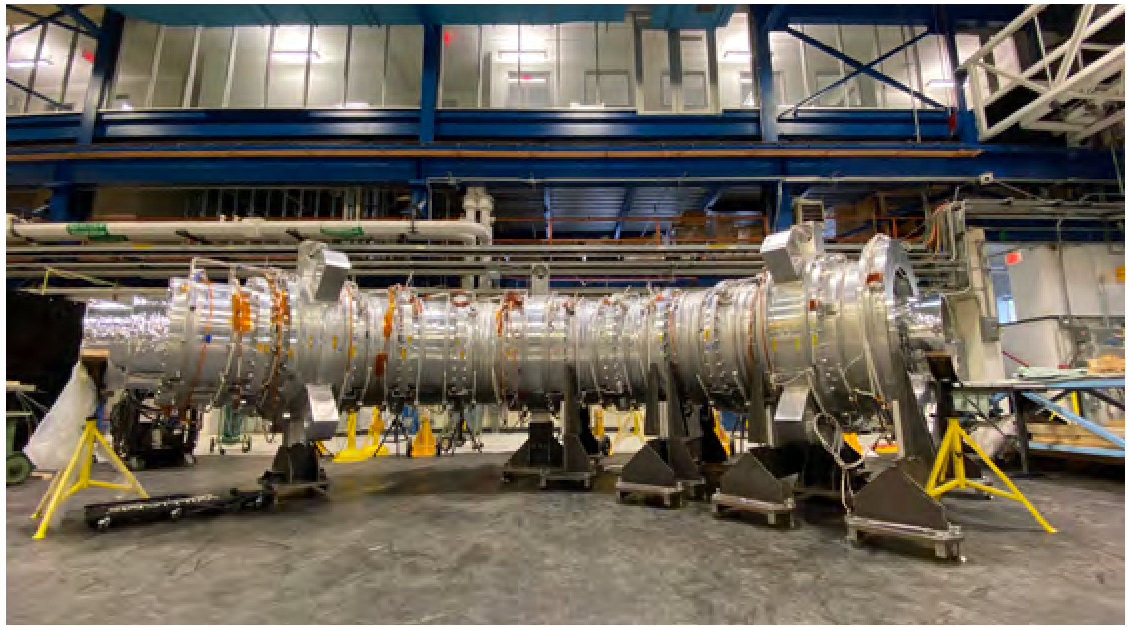

Figure 3. TSu assembled at Fermilab premises (Photo Courtesy of Fermilab)

The conductor is an aluminium stabilized NbTi Rutherford cable.
This kind of conductor is typically used for detector magnets in particle accelerators and colliders.
The conductor parameters are shown in Table 2. The conductor is wrapped by fiberglass tape, wound with 50% overlap, with a resulting thickness of 0.15mm per side.
VPI Epoxy impregnation is used to complete the insulation.
Each TSu and TSd subassembly is powered by a dedicated power supply.
The operating current is 1730A and the operating current density is 47A/mm2.
The peak field on TS coils is 3.4T.

**Table 2** Below are the main parameters of the TSU Conductor:

| Symbol | Unit | Value |
|---|---|---|
| Strand diameter | mm | 0,67 |
| Number of strands | | 14 |
| Cu/non Cu ratio in the strand | | 1 |
| Initial RRR of Cu matrix/Al stabilizer | | 150/800 |
| Al-stabilized cable width | mm | 9,85 |
| Al-stabilized cable thickness | mm | 3,11 |
| Cable critical current at 5T, 4.2K | A | 5.900 |
| Operating current | A | 1.730 |
| Test current | A | 2.100 |
| Peak field along the magnet central axis | T | 2,5 |
| Peak coil field ($B_{peak}$) | T | 3,4 |
| Thermal margin at $B_{peak}$, $T_{peak}$ | K | 1,87 |

## The Coils

The “S shaped” Transport Solenoid (TS) consists of 52 solenoids which select and transport the selected muons towards a collection target.
At the end, the Detector Solenoid has an axially graded solenoid at the upstream end to focus transported muons onto a collection target, and a spectrometer solenoid at the downstream end to accurately measure the momentum of the outgoing elections produced by the conversion process.

The main steps of the fabrication of each component of the TS system are the following:
— Winding on a collapsible inner mandrel. A cooling thermal sheet made of aluminium alloy is integrated in the inner diameter before the first layer is wound.
— Vacuum potted impregnation phase.
— Resin excess removal.
— Coil is turned to obtain a perfect cylindrical outer surface in order to allow proper shrink fitting into the Al-housing.

Each coil is fabricated using a continuous unit length of superconductor: no internal joints are present.
The Splice joints between the coils are realized on the outer surface of the housing.
During the final testing of the Units at the Fermilab premises, every unit is powered up to 120% of the operating current in order to gain acceptance.

## The Coil module

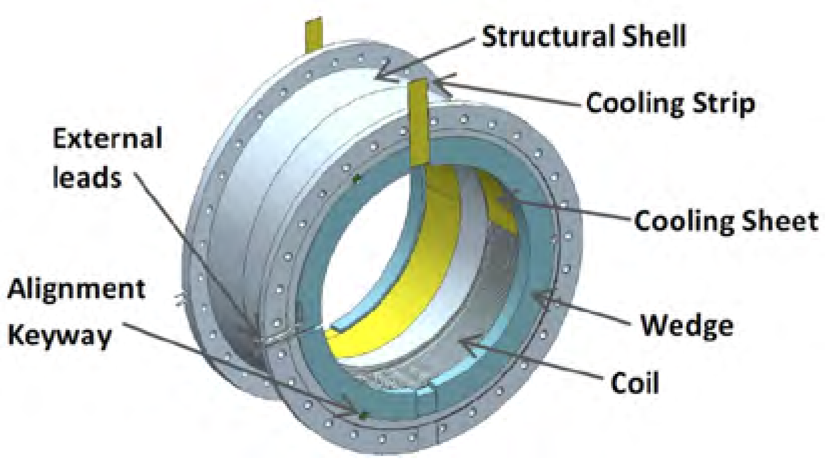


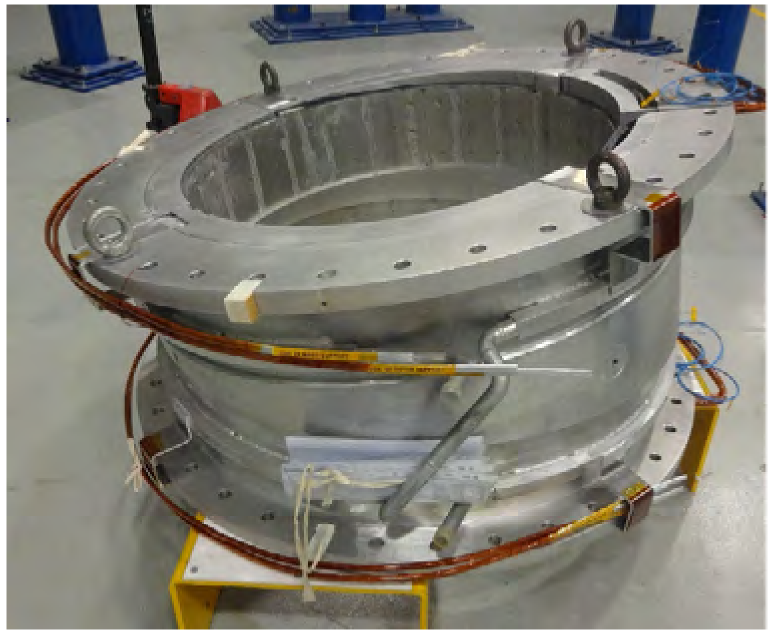

**Figure 4.** TS Module





## The Coils

Each module can house two coils, which are inserted from each end. Each housing is warmed up, allowing sufficient clearance for coil insertion followed by a shrink fit process.
The coil outer diameter interference with respect to the housing inner surface is 0,5mm at room temperature.

The Module consists of:

→ A housing shell
This is a huge structure that surrounds one or two solenoids. The shrink fitting operation applies sufficient prestress to the coils for withstanding the Lorentz Forces generated during energization. The shell is fabricated using a 5-axis industrial milling machine and a CNC lathe.

→ A cooling circuit
This is an aluminium alloy hollow square pipe that surrounds the shell. Inside, liquid helium flows at 4.2K. By thermal conduction it cools down the module itself.
The cooling circuit is welded to the shell's outer surface. Heat is conducted from the coil to the cooling system by conduction and by strips of pure aluminium connected to the coil inner surface.

→ Two or more splice boxes
These boxes contain the electrical joints between the coils of the same module and between two adjacent modules.

→ Wedges & spacers
The coils are retained by the wedges to give each coil the required axial pre-compression while the spacers are realized by thin Al shims used to compensate the different coil heights.

→ Flanges
These are used to bolt the modules to each other. This is necessary to form the "S shaped" structure.

→ One or two coils

The main steps of the Module assembly process are the following:

### Coil fabbrication

The coils are designed and fabricated with sufficient insulation on the outer diameter to ensure a minimum insulation thickness (after machining) of 4mm.
The total conductor length used for realizing the 52 coils was about 36km with a single length varying from 200m to 1.200m.

### Shell fabrication

Each shell is produced following these steps:
1) The outer surface is machined to the final dimensions.
The inner surfaces where the coils are going to be housed are rough machined only.
2) After step 1) the pipes for the cooling circuit are welded to the shell outer surface and tested in order to be pressure and leak proof.
In parallel each coil is wound, impregnated and machined.
3) The inner surfaces ID where the coils were going to be housed are fine machined to the dimension resulting from the coil turning operation.
The interference at room temperature is specified by the Customer to be 0,5mm on the diameter at room temperature.
The shell ID fine machining is performed at constant temperature.

### Coils shrink fitting into the housing

This operation consists of heating up the housing to a temperature of 110°C and then performing the shrink fitting operation on both sides.
The operation is carried out using special tooling to centre the position of each coil and to allow the flipping of the structure in order to repeat the operation on the opposite side.

**Figure 5.** Shrink-fitting operation at ASG premises





## The Unit

The fourteen units have been assembled at ASG's premises between the end of September 2018 and October 2020.
The assembly consists of bolting by high strength Al-alloy screws the flanges and then welding the "crossover pipe" that connects the two modules hydraulically. A pressurization test followed by LN2 thermal cycles and the final leak test completes the test campaign carried out on each module.

**Figure 6.** Last Unit (Unit 14) assembled at ASG premises in October 2020

# HIGH PERFORMANCE MAGNET RAMPING

# $MgB_2$ OPENS THE DOOR TO HIGH PERFORMANCE MAGNET RAMPING

## Energy Storage, intraoperative MRI and particle therapy applications: empirical evidence shows $MgB_2$ confirms all theoretical expectations in carrying rapidly varying currents at 20K.

Alessio Capelluto, Lorenzo Mauro

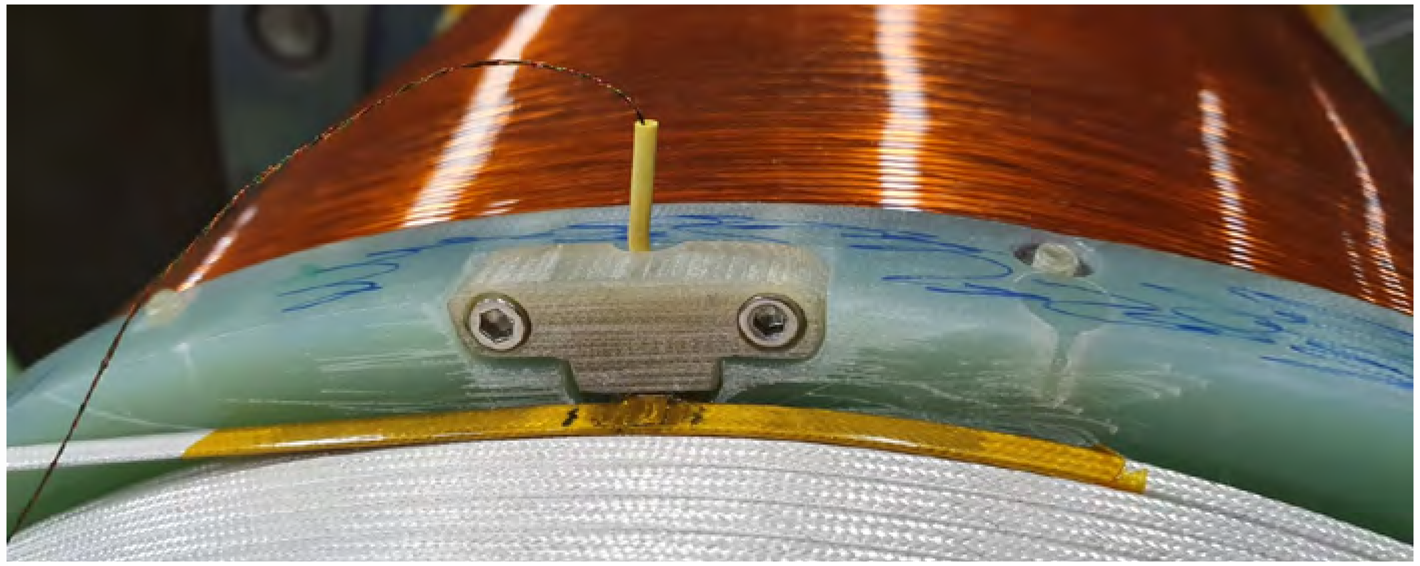

As is well known all types of superconductors are affected by AC losses.
Those losses occur when a time varying current flows in a superconductor or when it's subjected to a variable magnetic field. The main effect of these losses on the conductor is temperature rise due to the energy dissipation within the superconductor. Many methods were previously studied in order to reduce the magnitude of this loss. The main task of superconductor manufacturers is to optimize the design of the wire in order to reduce AC losses according to the magnet requirements.
This paper presents experiemental results of an empiric experiment designed to demonstrate the theoretical benefit of $MgB_2$, with respect to standard NbTi, in low-field/fast-ramped applications.

## 1 Introduction

### 1.1 AC losses

During current ramps the magnet wires are subjected to a variation of magnetic field. Superconductors subjected to varying magnetic fields see multiple heat sources that can impact on the conductor performance and stability. All the energy loss terms can be expressed as an equivalent magnetization loss induced in the conductor [1].
The superconductor $\mathrm{M}-\mathrm{H}$ cycle defines losses associated with magnetization: the area enclosed in a loop is lost as heat.
This loss can be evaluated as

$$Q = \int \bar{M} \cdot d\bar{H} = \int \bar{H} \cdot d\bar{M} \tag{1}$$

Two major contributions are taken in account: hysteresis losses and coupling losses. Using the simplest model [1] the equivalent magnetization linked to the first contribution is equal to:

$$M = \frac{2}{3\pi} J_c d_f \lambda \tag{2}$$

Where $J_c$ is the critical current of the superconductor, $d_f$ is the diameter of the filaments that compose the wire and $\lambda$ is the ratio of the cross section areas of superconducting and resistive parts of the wire.
It is possible to demonstrate that a superconducting wire subjected to an external varying magnetic field experiences an induced electric field which causes current to flow in the resistive wire stabilisation matrix.
These induced currents are called inter-filament coupling current.
In order to compare these losses to the hysteresis ones we can express the coupling losses as a magnetization contribution equal to [1]:

$$M = 2\dot{B}_i \tau \lambda_f \tag{3}$$

where $\dot{B}_i$ is the time derivative of the internal magnetic field, $\tau$ is the raise time of the coupling currents and $\lambda_f$ is the fraction of the surface occupied by the superconducting filaments over the section of the entire wire.
In conclusion, using this model, the power density generated during field variation is equal to:

$$P = \underbrace{\frac{2}{3\pi} J_c d_f \lambda \dot{B}_i}_{\text{hysteresis}} + \underbrace{2\tau\lambda_f \dot{B}_i^{\,2}}_{\text{coupling}} \tag{4}$$

The parameters that most affect this heat generation are linked to the wire and strand geometry.

### 1.2 Temperature rise

A power loss inside a superconductor leads to a temperature rise. Depending on field amplitude and ramp speed this temperature rise can be high enough to cause transition to the normal state (quenching). Two main strategies can be used in order to reduce this phenomenon:

1. Wire and strand optimization
2. Increase of the enthalpy margin

Clearly those two methods can be combined in order to reduce the impact of AC losses on the performance of the wire.
The first method consists in optimising the manufacturing parameters of wire and strands in order to reduce the AC losses described in the previous section [2]. The second strategy is to reduce the temperature increase, not by reducing the losses, but by enlarging the enthalpy margin to transition of the conductor. To achieve this it is necessary to change materials and most importantly, to operate at high temperature. Indeed enthalpy has a strong dependence on the temperature:

$$H = \int_{Top}^{Tc} Cp\,(T)\; dT \;\alpha\; T^4 \tag{5}$$

Increasing the enthalpy margin leads to lower temperature rise with the same dissipated energy.

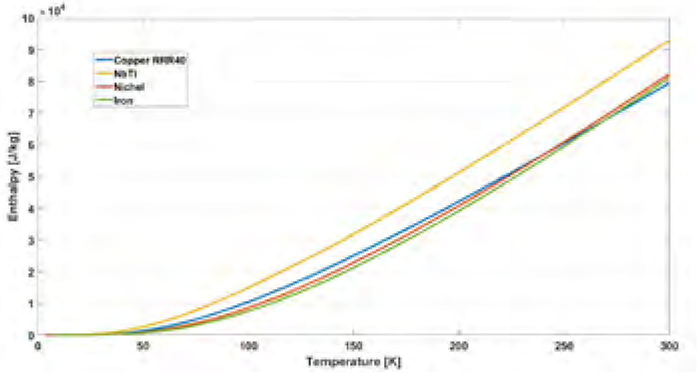


**Figure 1** Example of enthalpy for typical materials used in superconductor manufacturing

In the data analysis of this paper the enthalpy is replaced with the density of internal energy. This quantity can be evaluated using the simple relation:

$$E = \rho \cdot H \tag{6}$$

Where $E$ is the density of internal energy expressed in $J / m^3$ and $\rho$ is the density of the material taken in to account.

## 2 Empiric Experiment

An empiric experiment has been designed to compare the overall performance of NbTi and $MgB_2$ during field variation.

### 2.1 Design of the experiment

In order to compare NbTi and $MgB_2$ two solenoids were designed using legacy tool by ASG [5] and Cobham Opera [3].
The design was made using two standard commercial wires:

- NbTi commercial standard wire Ø1.8
- $MgB_2$ wire ASG MRO plus wire [4]

The results of the design are reported in the following list:

NbTi coil

- 1770 turns
- Ø 1.8 mm standard wire
$(d_f\ 50\ \mu m\ /\ l_p$[1] $50\ mm)$
- Central field at $250A = 1.4T$
- Max field on conductor at 250A = $1.7T$
- Inductance $0.77H$
(without $MgB_2$ nickel matrix contribution effects)

$MgB_2$ coil

- 1768 turns
- 3.79 × 0.77 $mm$ standard wire
$(d_f\ 500\ \mu m\ /\ l_p\ 750\ mm)$
- Central field at $250A = 1.4T$
- Max field on conductor at 250A = $1.7T$
- Inductance $0.75H$
(without $MgB_2$ nickel matrix contribution effects)

The two coils have been designed to be as similar as possible from a magnetic point of view.
According to equation (4) greatest losses will be expected in the $MgB_2$ coil. In order to optimize and simplify the set up the two solenoids are wound on the same former as shown in *Figure 2*.

[1] $l_p$ is called twist pitch and is the axial length in which a filament or strand firstly returns to its original relative position in a twisted conductor. This parameter highly affects the AC performance of the wire.





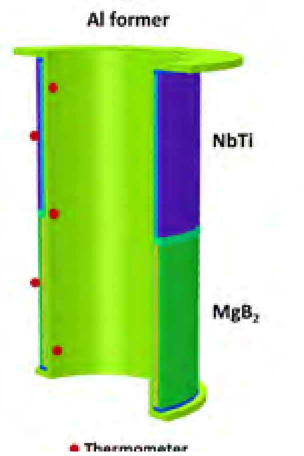


**Figure 2** Sketch of the experimental set up

The thermometers used in this experiment are the LakeShore Cernox CX-1050. The sensitivities of those sensors are shown in *Figure 3*.
The typical sensor accuracy at $10K$ is $\pm\ 6mK$.

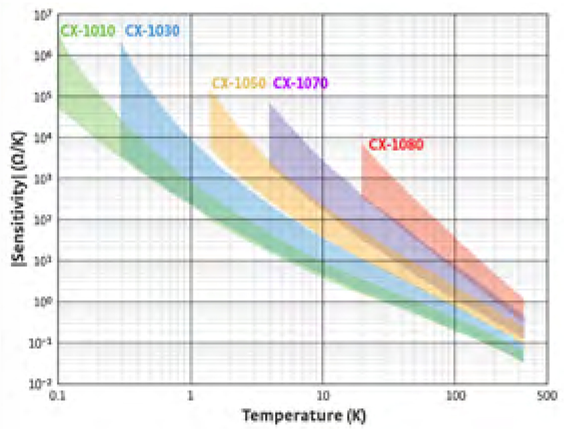


**Figure 3** Typical Cernox sensibility

### 2.2 Cooling system

The cryogenic system used to keep the set up cold is composed of a Sumitomo RDK 415D cryocooler and a Cryomech PT815 PulseTube.
The cryocooler 2nd stage is linked to the NbTi side of the coil, while the 1st stage is used to keep the thermal shield cold. The PulseTube is used to refrigerate the current leads. The details of the cooling system are reported in *Table 1*.

| | Dissipated heat [W] | Operating Temperature [K] |
|---|---|---|
| 1st stage RDK | 45 | 60 |
| 2nd stage RDK | 2 | 6 |
| 1st stage PT | 43 | 90 |
| 2nd stage PT | 12 | 15 |

**Table 1** Dissipated power and operating temperature of the different part of the set up (max field conditions)

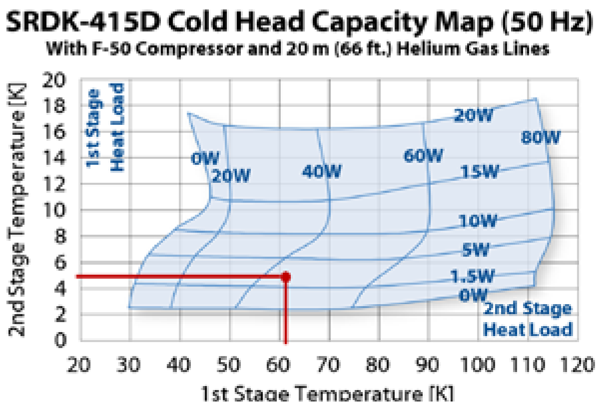


**Figure 4** Capacity map of Sumitomo RDK 415D and operating conditions of the facility (in red)

## 2.3 Electrical connection and bus bars

The two coils are connected in a three way system, as shown in *Figure 5*, but tested one at time. The power supply is capable of providing $6V$ and 300A.

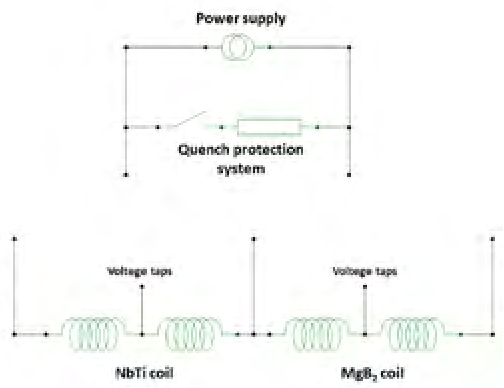


**Figure 5** Electrical scheme of the experimental set up





To reduce the heat input to the cold mass every lead is optimized in three different stages.
The protection system consists of an external dump resistor ($2.3\Omega$) and a quench detector with a $250ms/200mV$ trigger. Those values are evaluated using the Cobham Opera [3] quench module. Using those values the tension during a quench will be lower than $300V$ and the maximum temperature reached by the coil will be $120K$ at $256A$, established to be the maximum allowable temperature for coil safety in the case of a quench.

## 2.4 Manufacturing process

A 6061 aluminium former is placed on the winding machine. Then two layers of glass tape, half overlapped, are installed as ground insulation. The volumes that will be occupied by the two coils are delimited using G10 curved profiles as shown in *Figure 6*.

**Figure 6** Photo of the former placed on the winding machine with counter mass and G10 shoulders

The NbTi has the mid coil voltage tap placed at the 6th layer. The $MgB_2$ coil instead has the tap at the 13th layer. Once the wires are completely wound on the former another two layer of glass tape are wound over the magnet. To prevent any damage on the coil during the detachment of the extra epoxy resin after the impregnation one layer of PTFE tape is applied over the external counter mass. For the same reason all the surfaces are treated with a silicon based release liquid and all the brittle parts are covered with an appropriate soft filler. The result is shown in *Figure 7*.

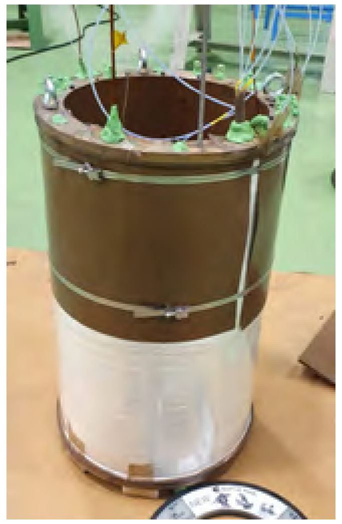

Figure 7 Photo of the coil before the impregnation process

The impregnation is made using an epoxy resin compatible with the materials used and the autoclave setting at 110°C for 96 hours. After impregnation and cleaning of the coil is set in position.

### 2.5 Final assembly

The coil is held in place using eight threaded rods (Ø6$mm$, L250$mm$) made of fiberglass N. Those rods are hung from the thermal shield in order to reduce the thermal input to the cold mass. The thermal link between the 2nd stage of the cryocooler and the coil is made with twelve 5N aluminium bars (20×4×250 $mm^3$). The shield is made of aluminium covered with 30 layers of MLI and kept in place by three threaded rods (Ø8$mm$, L350$mm$) made of fiberglass N linked to the vacuum chamber upper flange.

Figure 8 Photo of the facility before the closure of the vacuum chamber

The connection between the 1st stage of the RDK and the shield is achieved using eight copper braid of 25 $mm^2$ section and 300 $mm$ length. The cold mass, thermal shield, current leads and the two cold heads are linked to the upper flange of the vacuum chamber.





### 3 Experimental Data

As first several voltage controlled ramps have been done in order to caracterize the coil responses to fast charges up to the faster one in a fixed current range of $100A$. The $MgB_2$ winding presents higher inductance, than calculated from theory, believed to be due to to the nickel matrix. This implies that ramp speed would be slower than NbTi at the same voltage.

After checking compatibility of the system with the maximum voltage of $6V$ all the further ramps are done at the highes ramp speed. In the NbTi coil at max ramp speed, at $130A$, the quech protection system detects a resistive transition: the NbTi reached somewhere the critical tempereture. On the other side the $MgB_2$ coil reached, without thermal drawbacks, a current of $256A$ at maximum ramp speed. Relaxing the maximum acceptable quench temperature, it would be possible to reach higher current at the same ramp up rate.

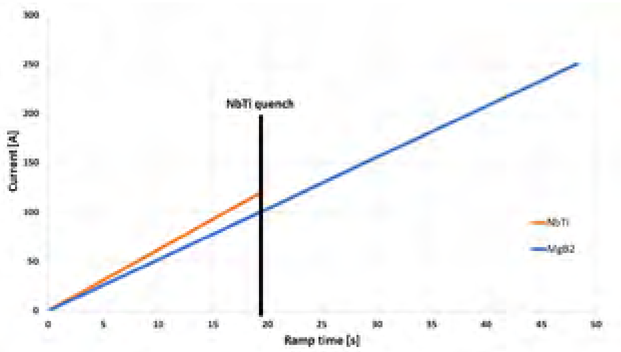


Figure 9 Recorder current during maximum speed ramp

From the recorded $100A$ ramps data is possible to evaluate the following results:

| P.S. output Voltage [V] | Current Increase [A] | Temperature Increase [K] | Ramp time [s] | Ramp rate [A/s] | Estimated energy release $[J/m^3]$ |
|---|---|---|---|---|---|
| 1.5 | 100 | 0.39 | 64 | 1.56 | 2431 |
| 2 | 100 | 0.22 | 48 | 2.08 | 3230 |
| 3 | 100 | 0.45 | 37 | 2.70 | 6594 |
| 5 | 100 | 0.57 | 26 | 3.85 | 8361 |
| 6 | 100 | 0.74 | 19 | 5.26 | 10831 |

Table 2 A selection of ramp up data of $MgB_2$ winding

| P.S. output Voltage [V] | Current Increase [A] | Temperature Increase [K] | Ramp time [s] | Ramp rate [A/s] | Estimated energy release [$J/m^3$] |
|---|---|---|---|---|---|
| 1.5 | 100 | 0.35 | 57 | 1.75 | 1357 |
| 2 | 100 | 0.47 | 46 | 2.17 | 1832 |
| 2.5 | 100 | 0.58 | 40 | 2.50 | 2262 |
| 3.5 | 100 | 0.83 | 27 | 3.70 | 3236 |
| 6 | 100 | 1.32 | 16 | 6.25 | 5147 |

**Table 3** A selection of ramp up data of NbTi winding

As shown in *Table 2* and T*able 3* the ramps are fast enough to be considered adiabatic and the temperature increases are low enough to allow evaluation of the density of the released energy as follow:

$$E = \rho \cdot Cp \cdot \Delta T - E_{eddy} \tag{7}$$

Where $\rho$ is the winding density, $Cp$ is the specific heat capacity and $\Delta T$ is the temperature increase during ramp up. $E_{eddy}$ is the contribution to the temperature increase due to the eddy current induced in the aluminium former. This contribution is evaluated using the Elektra Transient module of Opera [3]. The calculation of the $Cp$ of the wires is done by making a weighted average of the materials that compose them. The wire compositions are shown in *Figure 10*. The bulk heat capacity calculation takes into account also the insulation physical properties.

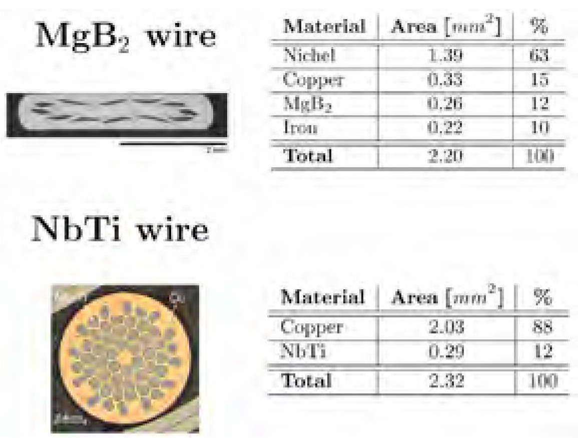
MgB$_2$ wire

| Material | Area [$mm^2$] | % |
|---|---|---|
| Nichel | 1.39 | 63 |
| Copper | 0.33 | 15 |
| MgB$_2$ | 0.26 | 12 |
| Iron | 0.22 | 10 |
| Total | 2.20 | 100 |

NbTi wire

| Material | Area [$mm^2$] | % |
|---|---|---|
| Copper | 2.03 | 88 |
| NbTi | 0.29 | 12 |
| Total | 2.32 | 100 |

**Figure 10** Detail of the composition of wires

As expected the energy released during ramps is higher in the MgB$_2$ winding as shown in *Figure 11*, but the overall performance is better.





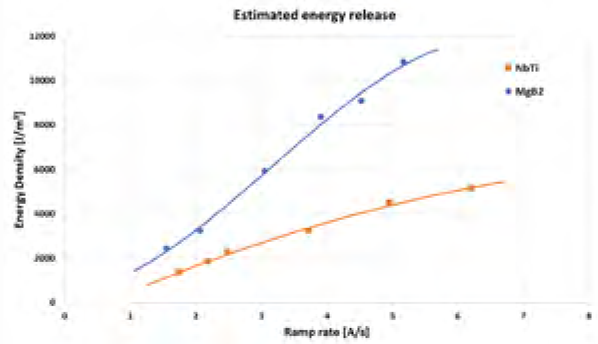


**Figure 11** Energy release at different ramp rate

The higher energy margin compensates for the higher losses. Indeed, as is shown in *Figure 12* and *Figure 13*, the MgB$_2$ energy needed to reach the normal state is 40 – 100 times higher than for the NbTi.

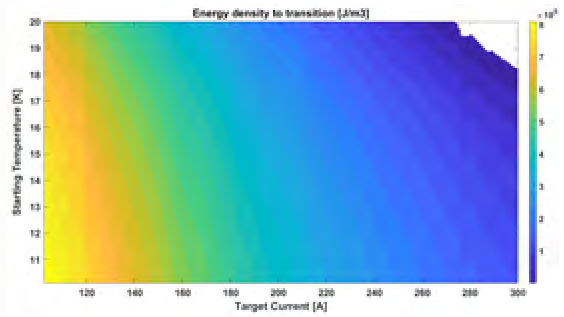


**Figure 12** Energy density to transition for MgB$_2$ winding as function of starting temperature and target current (adiabatic conditions)

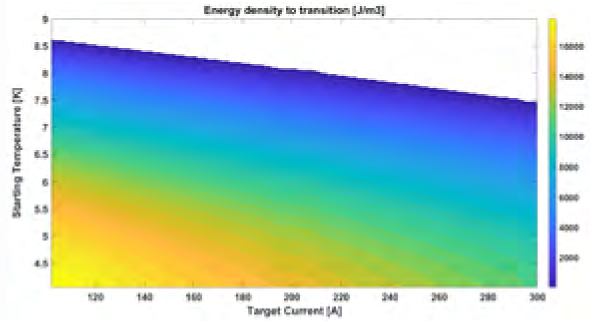


**Figure 13** Energy density to transition for NbTi winding as function of starting temperature and target current (adiabatic conditions)

The density of energy to transition shown in the two previous figures was evaluated using the relation:

$$E = \rho \cdot \int_{Ts}^{Tc\,(I,B)} Cp\,(T) \cdot dT \tag{8}$$

Where $T_S$ is the starting temperature of the magnet and $T_C\ (I,B)$ is the critical temperature of the superconductor as a function of operating current and external field. Some values of critical temperature are shown in *Figure 14* and *Figure 15*.

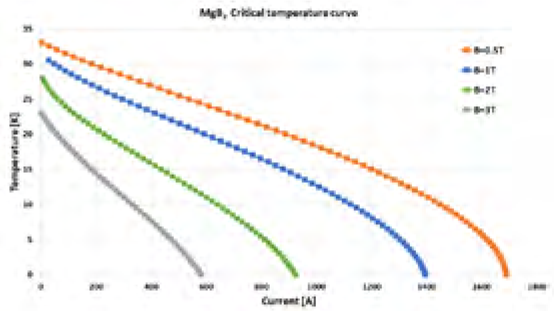


**Figure 14** Critical temperature curve of $MgB_2$ MRO plus wire

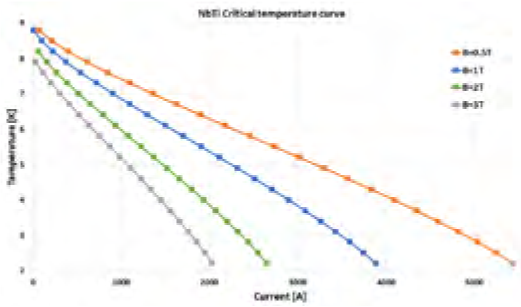


**Figure 15** Critical temperature curve of NbTi standard Ø1.8

## 4 Conclusions

As empirically demonstated by the previous data operating at higher temperature naturally means a wire more resiliant to field variations. Indeed the enthalpy benefits are neglible at low temperature because of the temperature dependance ($H \alpha T^4$). As can be deduced from *Figure 12* and *Figure 13* reducing the operating temperature of the $MgB_2$ coil from $15K$ to $14K$ increases the energy margin by 35 times more than in the case of the same temperature decrease of $1K$ at $5.2K$ for the NbTi coil.

### 4.1 Clarification example

To clarify the difference between temperature and energy margin an example, based on the measured data, will follow. Consider two coils, like those used for the experiment, ramped in 80 seconds up to $2T$.
In *Table 4* the energy densities released during the ramp up are shown.





| Energy density released in 80s ramp to $2T$ for NbTi | Energy density released in 80s ramp to $2T$ for $MgB_2$ |
|---|---|
| 9380 $J/m^3$ | 24000 $J/m^3$ |

**Table 4** Energy density released during ramp up of NbTi and MgB2 windings

As shown in *Figure 16* the energy released during the ramp up will bring the magnet to the transition temperature even if the starting temperature is $5.2K$ or $4.2K$. In this case a $1K$ margin gives only a 900 $J/m^3$ energy margin. This implies that in these conditions the temperature margin doesn't pratically affect the final temperature.

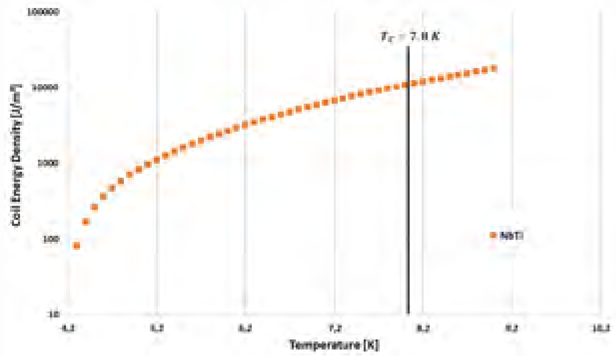


**Figure 16** NbTi coil energy density as function of temperature

On the other side the $MgB_2$ winding release more energy, during ramp up, due to the wire architecture. However the energy margin to transition is many times bigger because of the higher operating temperature. The same starting temperature difference of $1K$ leads to different final temperature as shown in *Figure 17*.

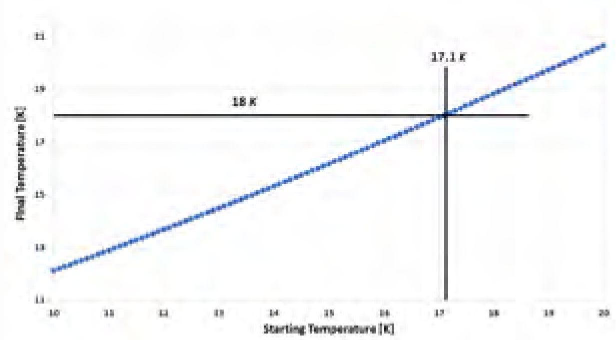


**Figure 17** Relation between starting and final temperature of the MgB2 winding during ramp up

## 4.2 AC losses optimization

Neither wires were optimized for AC losses but the $MgB_2$ demonstrated to be more adapt for low-field/fast-ramped applications than a standard NbTi wire. ASG $MgB_2$ wire division is improving the manufacturing process to optimize the wire parameters for AC losses. The state of art of AC losses optimization for $MgB_2$ wire is shown and compared to the wire used in this experiment in *Table 5*.

| Used for this experiment | | State of art | |
|---|---|---|---|
| $d_f$ [$\mu m$] | $l_p$ [$mm$] | $d_f$ [$\mu m$] | $l_p$ [$mm$] |
| 500 | 750 | 55 | 85 |

**Table 5** Comparison between sate of art of MgB2 wire and the one used for this experiment

Another pro of higher operating temperature is the costs reduction of the cryogenics. Indeed, using a cryocooler cooling system, a typical refrigerating power of $13W$ at $15K$ costs one half of a refrigerating power of $1.5W$ at $4.2K$.





## 4.3 Consecutive ramps

All the presented results are refered to a single ramp, fast enough to be considered adiabatic. During this experiment some consecutive ramps are recorded in order to emirically evaluate the overall response of the system. The aim of this paper is not to analize the behaviour of consecutive ramps. More complex studyes will be done taking in account the thermal diffusivity and all the non-neglible effects of consecutive charges.

The recorded data are resumed in the following graph.

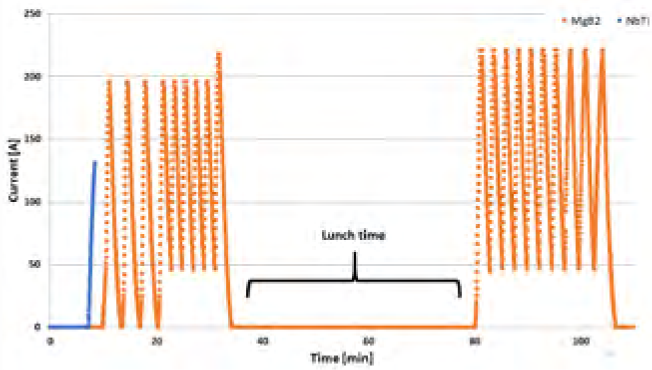


**Figure 18** Recorded current during multiple ramp up

As it's possible to see in *Figure 18*, the $MgB_2$ coil does not reach the operational critical value despite repeated charges and discharges in different current ranges.

**References**

[1] Wilson Martin N. 1983 *Superconductin Magnets* Oxford Science Pubblication

[2] M. Lyly, M. Holm, A. Stenvall and R. Mikkonen, *Design Process for a NbTi Wire With New Specification Objectives: Technical Design Constraints and Optimization of a Wire Layout Considering Critical Current and AC Losses*, in IEEE Transactions on Applied Superconductivity, vol. 23, no. 1, pp. 6000910-6000910, Feb. 2013, Art no. 6000910, doi: 10.1109/TASC.2012.2232918.

[3] Dassault Systemes *Opera version* 14R1 x64, www.3ds.com, 2018.

[4] ASG Superconductors S.p.A. Wire for MRI systems PLUS, www.asgsuperconductors.com

[5] A. Capelluto, M. Nervi, P. Molfino, 2014. *Algorithm for the Fast Calculation of Magnetic Fields Generated by Arc-Shaped Conductors With Rectangular Cross Section*. IEEE Transactions on Applied Superconductivity. 24. 1-5. 10.1109/TASC.2014.2326918.

# MAGNETIC FLUX DENSITY

Merging metrology with magnetic measurement: developing innovative and cost effective solutions for a flexible field mapper.

In magnet fabrication technology the effective magnetic field is the final indicator of the quality of the job.

Commercial solution are not flexible enough to cover all the needs of the workshop by using only one device.

This paper describes a flexible and innovative tool for the magnetic field mapping for the following case study: ITER Toroidal Field Coil Winding Pack WP magnetic flux density measurement.

# HIGH PRECISION MAGNETIC FLUX DENSITY MEASUREMENT

Alberto Barutti, Matteo Bargiacchi

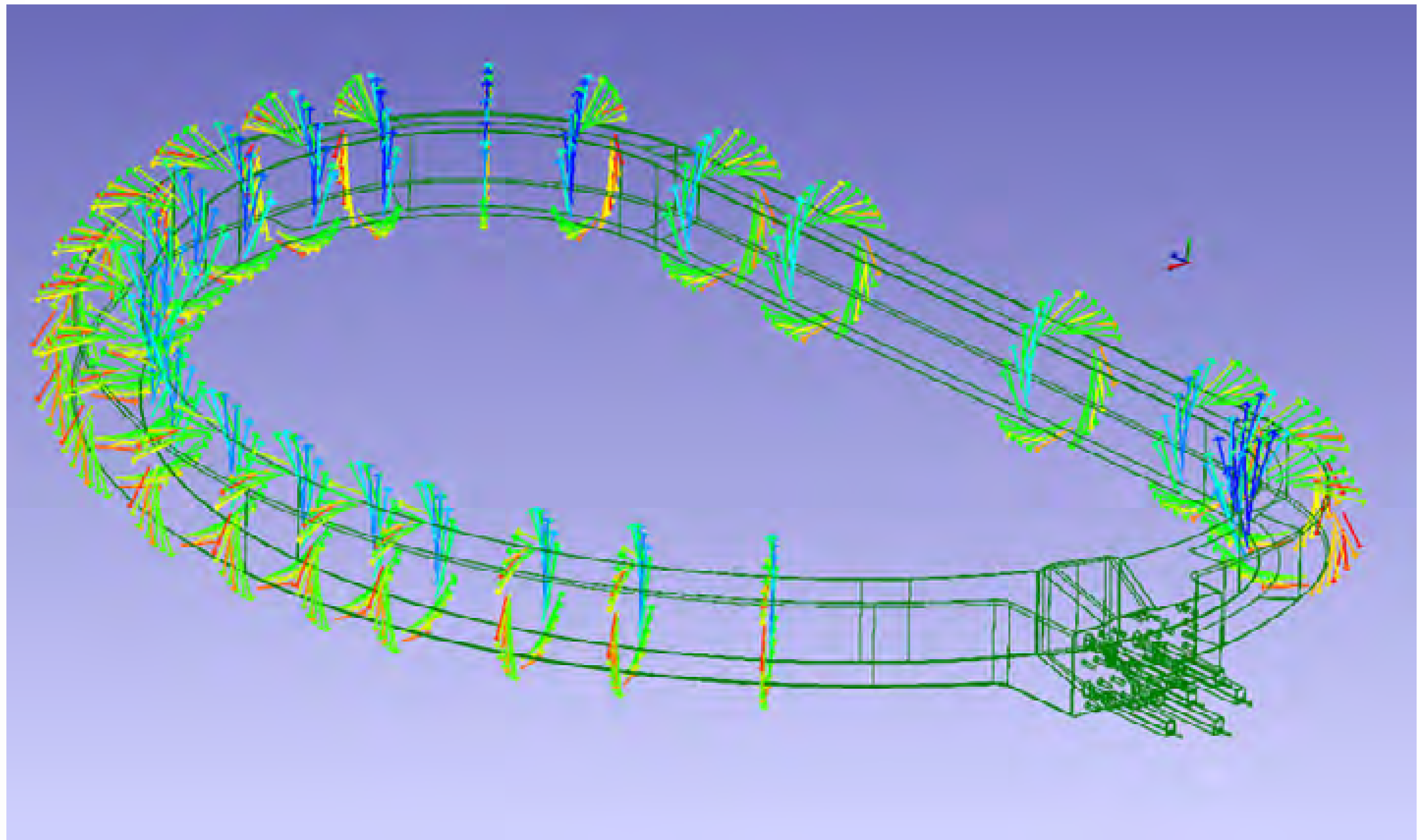

Merging metrology with magnetic measurement: developing innovative and cost effective solutions.
When ASG started the engineering of the ITER contract and the development of the necessary fabrication technology it started as well to face a very challenging technological goal: how to obtain very large component with high accuracies. Fusion for Energy (F4E), our customer, asked for the definition of some indicators for the as-built performances,
after the coil manufacturing, to check that the product quality fulfils the requirements and to allow the integration inside the reactor of the components supplied by ASG with the others produced by other firms.

https://fusionforenergy.europa.eu/

The most important key indicators in the definition of our coils as-built performances were identified to be:
— the as built dimensions
— the insulation system performances
— the room temperature magnetic field fingerprint. This is an indicator that allows to understand the quality of the internal geometry of the coils without accessing to the internal part of the coil.

Once the WP is completed it is not possible to access the internal components; the final assembly on the reactor must be driven by using a combination of the results of the test campaign during fabrication and after completion.

Cold tests campaign, that could allow to reach a field big enough to make easy measurements with large accuracies, is too expensive and not included in our scope of supply. Therefore, we decided to design a tool in order to guarantee enough accuracy to make the reconstruction of the magnetic field around the coil possible, by solving an inverse problem, with a very low field. This was useful also because at room temperature it's not possible to feed the coils with high current to avoid heating and large component deformations.

A first step was the Design of Experiment, whose results were the main parameters for the test design:
— Requirements of the workshop area.
— Huge number of points to be measured.
— Position and field measurements accuracy.
— Maximum current on the coil (i.e. maximum field available) in order to avoid thermal deformations.

The tool should have been robust, industrial, within time and budget: no ready commercial solution was available.

— **Goal**: obtaining a map of the magnetic field around the coil at standard temperature
— **Delighter**: speed and flexibility of the measurement system
— **To solve**:
  → No commercial solution available.
  → Required accuracy is close to the best available technology.
  → We are an industry, not a laboratory.
  → Very low magnetic field: approximately 150 G (15mT).
  As a comparison, the earth magnetic field is approximately 1000 times smaller (0.5G = 50μT) and the peak field of the magnet is 1000 times bigger (118 000 G = 11.8 T).

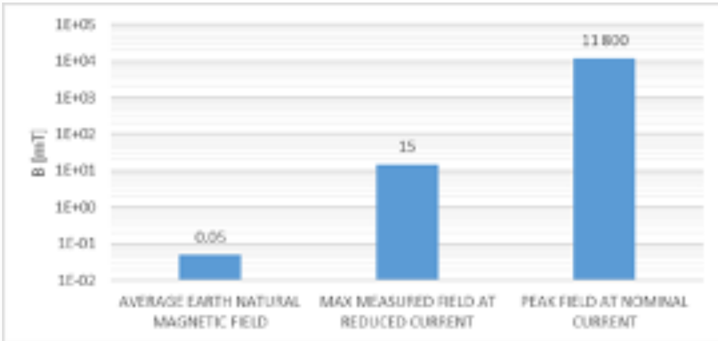


**Figure 1**. Magnetic field ranges in logarithmic scale.

Only after a long scouting some custom solutions was found, but they seemed too difficult to be developed in a timely manner, not robust enough and with poor flexibility. In the scouting process we understood that a flexible solution should be preferred, both for the scope of the project and for future transfer to other applications.

A flexible field mapper, in fact, is needed for environmental field mapping, including the fringe field on the installations, the fringe MRI field mapping and many other uses. In particular, such technology is useful where it is necessary to sample a big number of measured points in a short time, with no predetermined location in space but with a precise knowledge of their position (it will be shown that it is possible to get points with a precise positioning).

All these reasons convinced us to turn to an internal solution, by adapting the technology and know-how already in our possession.

So, we started to implement our solution, based on the merging of two supposedly distant worlds, metrology and magnetic measurements, which turned out to be an innovative measurement system based on a laser tracker and a Hall probe.

The main advantages of this configuration are:

— The possibility to share the same reference system between metrologic and magnetic measurements (and correlating results).
— The flexibility to measure objects with virtually all shapes and dimensions (no theoretical limit to dimension).
— It is possible to map a large volume of space obtaining the three components of the magnetic field and the position of the probe immediately with one measurement.
— Thanks to the innovative design of the hall probe (with a very small sensible volume) it is possible to operate in highly inhomogeneous magnetic fields without significant loss of information.
For a smarter use of this system, we developed a software plugin that allows to measure the magnetic field directly through the GUI (Graphic User Interface) of the commercial metrological software that we have adopted for the laser tracker management, making it easier to use the tooling and the generation of the output.





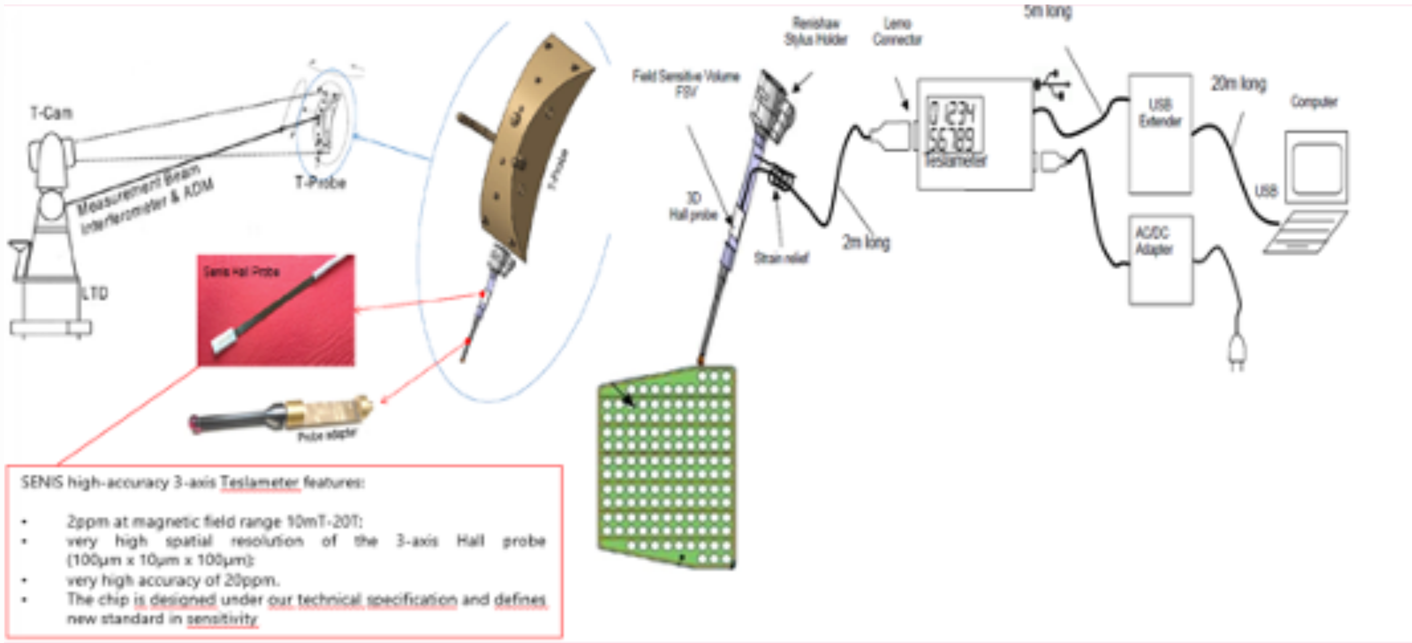


## 1. Introduction and scope of the measurement campaign within the ITER project

[1] https://www.iter.org/mach/magnets

Regarding the ITER TF project, each of the 18 Toroidal Field Coils Winding Packs (TFC-WPs) is composed of 134 turns made of niobium-tin ($Nb_3Sn$), generating a peak field of 11.8T and storing 41GJ[1]. Fabrication and assembly tolerances might generate sensible deviations from the expected nominal field generated inside the Tokamak.

The magnetic Flux Density Field $\vec{B}$ generated by the TF coil is therefore characterized through the definition of the Current Center Line (CCL) of each TFC-WP. The CCL is defined as the *single turn* that best approximates the field generated by the complete winding of each single TFC-WP, i.e. the solution of the inverse problem that minimizes the difference between the measured and nominal values of the magnetic field $\| B_M - B_N \|$, and represents the fingerprint of each coil. Current specifications for the ITER project require the reconstruction of the 3D position of the CCL for each TFC-WP, for the purpose of using these data during the final alignment of the coil inside the Tokamak. In order to achieve such a goal, it is essential to measure the field produced by the TFC-WP, at room temperature, with a tight accuracy.

## 2. The instrumentation concept, calibration and uncertainty essentials

A fully integrated 3-axis Type C hall probe[2] has been designed and realized in order to map the 3D field generated by the TFC-WP. Hall Effect is a well-known principle widely used for a broad range of applications, from proximity sensors in their simplest forms, to magnetometers. Hall Effects is based on the Lorentz force that electric charge carriers experience while travelling in a conductor immersed in a transverse magnetic field $B$. The displacement of the charges within the sensor generates an electric field mutually perpendicular to the current I and B. The hall probe sensible volume HSV measures 0.1 × 0.1 × 0.1 mm: it is embedded into an outer volume of about 8 x 4 x 0.9mm3 and mounted on the stylus of a Leica T-probe[3] as shown in Figure 3. The Leica T-Probe is a 6 Degrees of Freedom PCM device (Portable Coordinate Measurement) based on the combination of photogrammetry and an Absolute Laser Interferometer (AIFM). A T-probe simultaneously measures the position and the orientation of the device. Such a feature is essential to characterize the HSV with respect to the absolute reference frame of the object under measure.

[2] https://www.senis.ch/magnetometer/hall-probes

[3] https://www.hexagonmi.com/it-IT/products/laser-tracker-systems/leica-probing-solutions/leica-tprobe

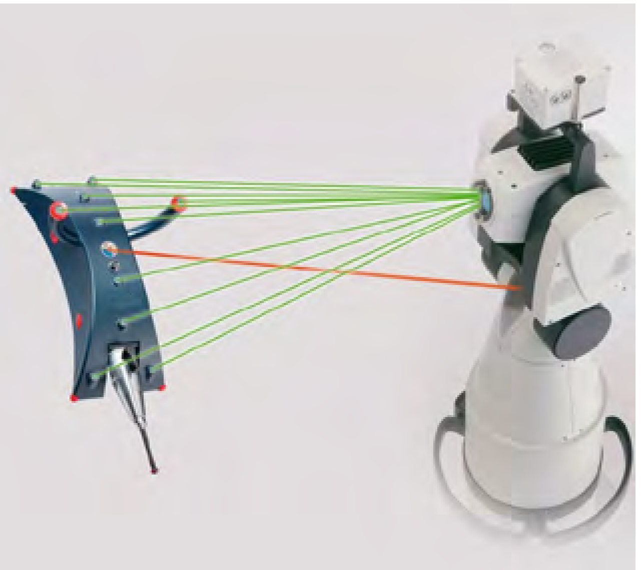

**Figure 2.** Leica Laser Tracker 6 DOF system (T-Probe). The position of the reflector is measured via the AIFM (red beam). The orientation of the device is measured via the T-Cam and a set of LEDs embedded on the surface of the target device (green beams).






**Figure 3.** ASG integration of a SENIS Type C Hall Probe inside the stylus of a Leica T-Probe. The white cable connected to the electronics supplies the DC current to the sensor and measures the DC voltage generated by the Lorentz force. A reference frame is defined centered on the T-Probe.

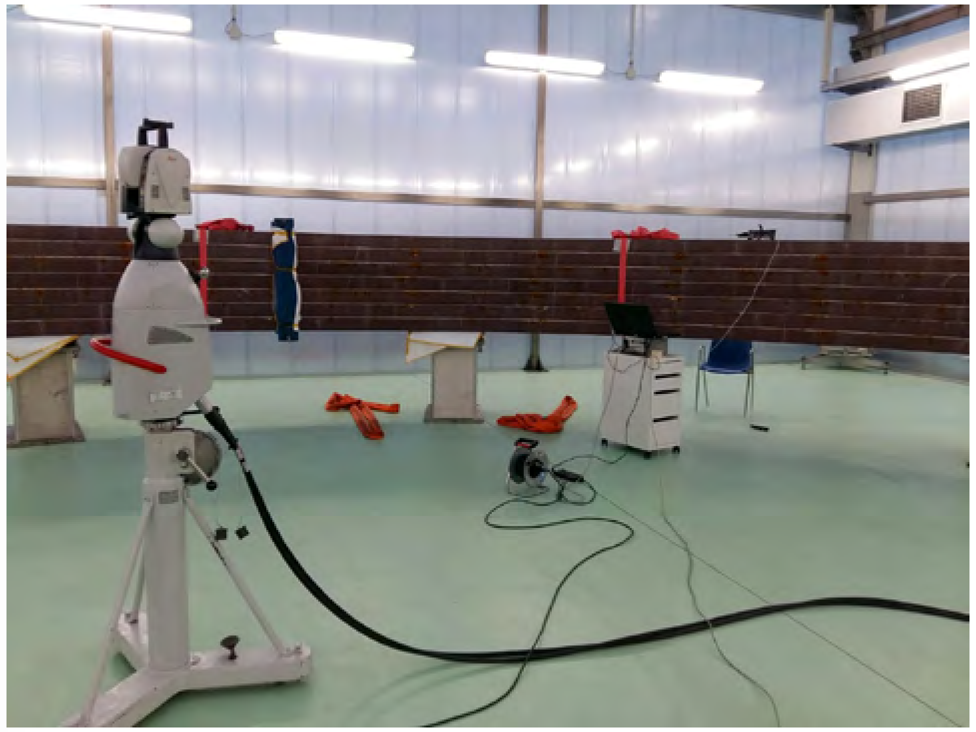

**Figure 4.** A picture shot during the R&D activities in 2016 on a WP, before its ground insulation.

This device concept requires a careful calibration activity. In practice, a set of matrix transformations is necessary to retrieve the real magnetic field from the raw magnetic field measured by the Teslameter and the 6 DOF measured by the T-Probe. This was the main activity carried out during the last months of 2016 and the first half of 2017 up to the first successful measure of the magnetic field generated by a WP, performed in June 2017. The accuracy with which the transformations matrices are calculated greatly influences the accuracy of the final measure. The calibration activity determines the final uncertainty of the measure and is the core of the present work.

The absolute field defined with respect to the absolute reference frame TGCS (Tokamak General Coordinate System, see Figure 12, later in this paper) of the object under analysis is $\vec{\boldsymbol{B}}_{TGCS}$. This is the final output, starting from the raw field vector $\vec{\boldsymbol{B}}_H$ that the operator can to read on the screen of the Teslameter. Anyway, the Teslameter does not know the orientation of the 3 axis of the HSV with respect to the absolute reference frame. Two transformation matrices $\underline{\boldsymbol{R}}$ and $\underline{\boldsymbol{C}}$ must be applied to the vector $\vec{\boldsymbol{B}}_H$. Matrix $\underline{\boldsymbol{R}}$ is a pure roto-translation (orthogonal matrix) coming from the Euler angles of the T-probe stylus $R_x$, $R_y$ and $R_z$ and absolute position $\vec{\boldsymbol{r}}$. It requires no additional calibration and varies in each measure, according to the orientation of the T-probe with respect to the absolute reference frame. Matrix $\underline{\boldsymbol{C}}$, on the other hand, is a non-orthogonal matrix resulting from calculation, and constant for all the measures.

The calibration of the system is embedded in matrix $\underline{\boldsymbol{C}}$. The raw field vector $\vec{\boldsymbol{B}}_H$ is roto-translated according to the Leica angles $R_x$, $R_y$ and $R_z$ and absolute coordinates vector $\vec{\boldsymbol{r}}$ to obtain the field referred to the absolute system $\vec{\boldsymbol{B}}_{TGCS}$. The expression is:

$$\vec{\boldsymbol{B}}_{TGCS} = \underline{\boldsymbol{R}} \cdot \underline{\boldsymbol{C}} \cdot \vec{\boldsymbol{B}}_H = \underline{\boldsymbol{R}} \cdot \vec{\boldsymbol{B}}_{T\text{-}Probe}$$

It is straightforward to understand that the so called calibration matrix $\underline{\boldsymbol{C}}$ is a function of the orientation of the hall axes with respect to the T-probe axes. Its definition is:

$$\underline{\boldsymbol{C}}^{-1} = \begin{bmatrix} \vec{x}_H^{\,T} \\ \vec{y}_H^{\,T} \\ \vec{z}_H^{\,T} \end{bmatrix}$$

Each line of matrix $\underline{C}$ is the transposed vector representation of each hall axis in the reference frame of the T-probe (see Figure 3).

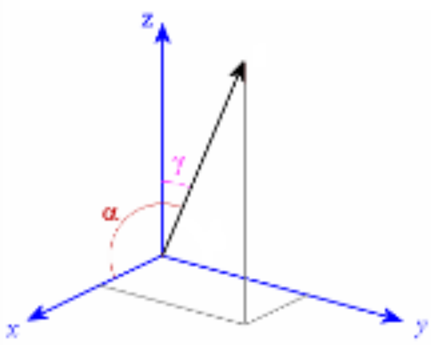


**Figure 5.** Vector representation of a single Hall probe axis inside the xyz T-probe reference frame (r = 1). Frame in figure is the same shown in Figure 3.

Actually, the chain of measure requires a careful calibration at different level to minimize the uncertainty related to the measure. Low level calibration and temperature corrections is provided directly by SENIS, the probe supplier, via firmware integration. This will be included in the uncertainty model but is not the object of this paper or of additional evaluations. We will see that its contribution to the final uncertainty will be automatically included during the calibration process. Geometrical calibration, synthetized in the constant calibration matrix $\underline{C}$, is essential to compensate for the following assembling imperfections:

1. Non orthogonality of the hall probe's axes $\mathcal{H}\mathbf{no}$
2. Misalignment of the hall probe's orthogonalized axes $\mathcal{H}\mathbf{o}$ with respect to the orthogonal T-Probe axes $\mathcal{T}$

| Variable | Symbol | Correction applied | Application level |
|---|---|---|---|
| Voltage output | $\vec{U}_{RAW}$ | — | Firmware |
| Corrected voltage output | $\vec{U}_{T} = \vec{U}_{T}(\vec{U}_{RAW})$ | Temperature compensation | |
| Raw field | $\vec{B}_{H} = \vec{B}_{H}(\vec{U}_{T})$ | Standard calibration curve from -40mT to 40mT per each component | |
| Orthogonalized Field aligned to T-Probe relative reference frame | $\vec{B}_{T\text{-}Probe} = \underline{C} \cdot \vec{B}_{H}$ | Sensitivity evaluation with respect to 3 orthogonal axes + Orthogonal rotation with respect to relative (T-probe) axes | Constant calibration matrix applied in the software $\underline{C}$ |
| Field aligned to absolute reference frame | $\vec{B}_{TGCS} = \underline{R} \cdot \vec{B}_{T\text{-}Probe}$ | Roto-translation | Variable transformation matrix $\underline{R}$ applied at each measured point |

Calibration and uncertainty evaluation were at first performed in collaboration with the Italian National Institute for Metrologic Research (INRIM[4]) in 2017. INRIM supplied a calibrated Helmholtz Coil[5] that was used to produce a steady and uniform reference field in the measurement range (see Figure 6). The reference field is aligned to the X axis of the HH coil and its homogeneity ΔH / H is smaller than 1e-4 in a sphere of 10 mm radius. This feature allows to place the HSV inside a homogeneity volume that is big enough to assume that the field measured is always the same in the absolute reference frame of the HH coil aligned to the Laser Tracker.

[4] https://www.inrim.it/

[5] F. Fiorillo, G.F. Durin, L. Rocchino, A reference system for the measurement of low-strength magnetic flux density, Journal of Magnetism and Magnetic Materials, Volume 304, Issue 2, 2006.





Essentially, the HH Coil from INRIM was used to calculate the calibration matrix $\underline{C}$. The hypothesis is that the reference field $\vec{B}_{REF}$ inside the homogeneity volume is constant regardless the position and orientation $\underline{R}_i$ of the sensible volume. The raw data from the 3 axis of the sensor $\vec{B}_{Hi}$ and the matrix $\underline{R}$ are registered and an GRG optimization loop is deployed to calculate the best coefficient of the calibration matrix $\underline{C}$.

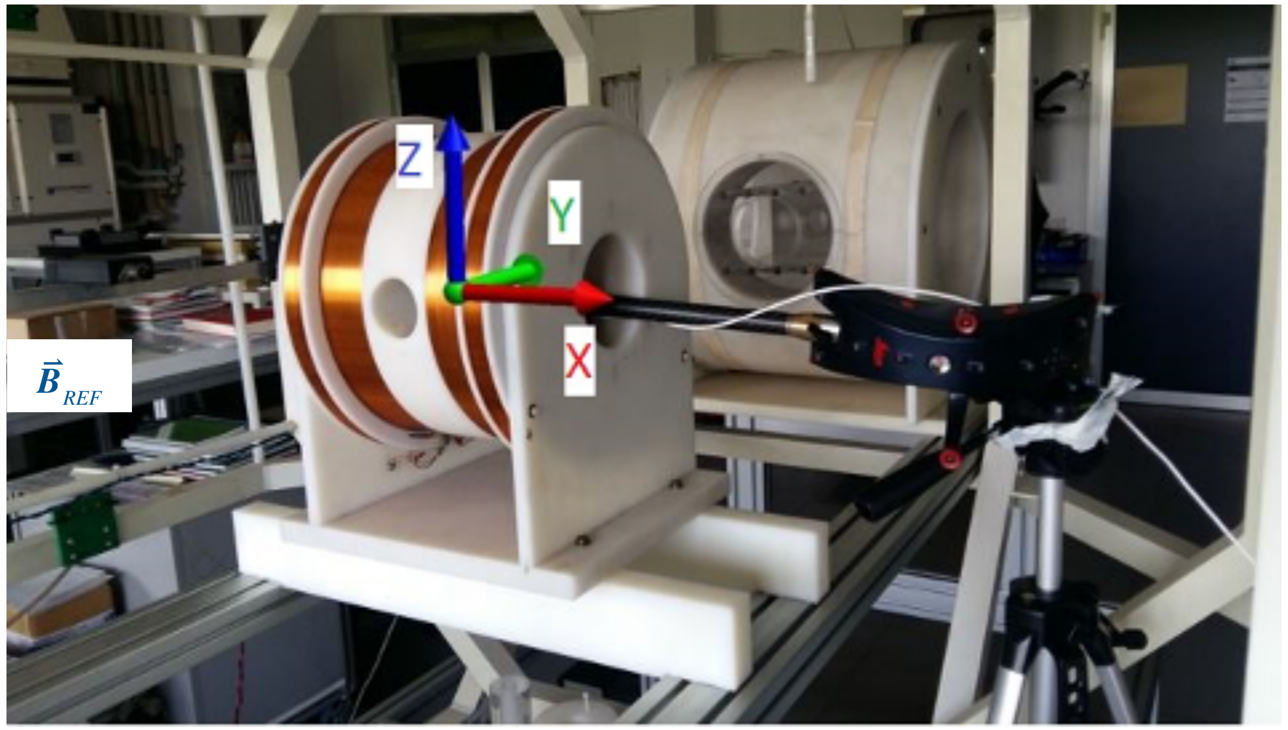


**Figure 6.** Calibration and uncertainty evaluation using a certified HH Coil @ INRIM.

The target function of the optimization is $\boldsymbol{J}(\underline{\boldsymbol{C}})$, defined as follows:

$$\boldsymbol{J}\,(\underline{\boldsymbol{C}},\ \vec{\boldsymbol{B}}_{REF}) = \sum_i \| \vec{\boldsymbol{B}}_{REF} - \underline{\boldsymbol{R}}_i \cdot \underline{\boldsymbol{C}} \cdot \vec{\boldsymbol{B}}_{Hi} \|$$

The optimization parameters are the components of matrix $\underline{\boldsymbol{C}}$ and the 2 Euler angles of the reference field $\beta_x$, $\beta_z$, that, in principle, are not known a-priori with enough precision.

The geometrical centre of the HH coil is detected probing the surface of the coils. High accuracy is not necessary, as the homogeneity volume is big enough to allow some errors in the evaluation of its centre.

Anyway, the optimization process produces an orientation of the reference field $\vec{\boldsymbol{B}}_{REF}$ that differs from the geometrical approximation by $14.7\ mrad$ and $\beta_z$ and $0.5\ mrad$ for $\beta_z$ only. Nevertheless, the magnitude of these angles does not influence in any way the calibration procedure, as the reference field is fixed and uniform regardless of its orientation. Anyway, they give a good grasp of the quality of the geometrical characterization of the HH coil.

A campaign of 90 different measurements, with different combinations of current applied to the coils and orientation of the probe, was performed. The set of positions was chosen in order to have the minimum condition number for the system to be solved, i.e. to have enough orientation to maximize the sensitivity for each axis of the hall probe.

Mathematically speaking it is an over-constrained non-linear system of 90 equations with 8 unknowns to be solved via an iterative approach. The distribution of the relative error with respect to the reference field

$$\varepsilon\% = \frac{\|\vec{\boldsymbol{B}}_{REF} - \vec{\boldsymbol{B}}_{MEASi}\ \|}{\vec{\boldsymbol{B}}_{REF}}\ \%$$

is shown in Figure 7.

The average is found to be 0.13% with a standard deviation of 0.05%. These numbers include also the uncertainty on $\vec{\boldsymbol{B}}_{Hi}$ and on $\underline{\boldsymbol{R}}_i$ produced by the Teslameter and by the Laser Tracker respectively.





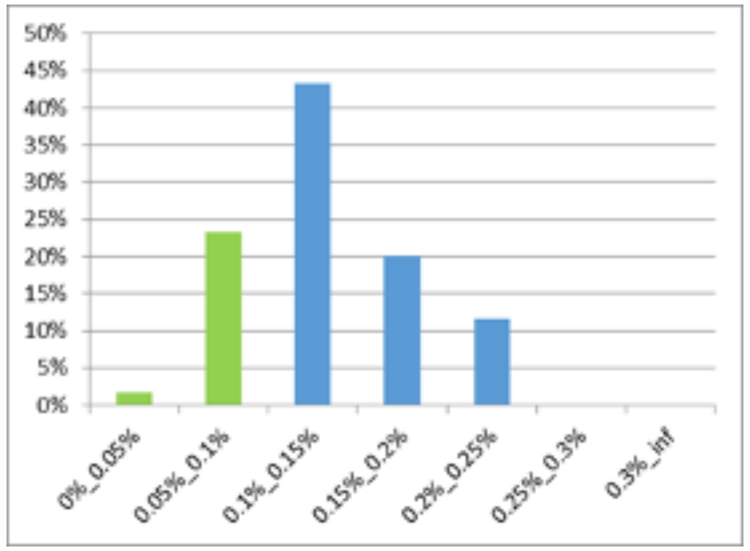


**Figure 7**. Distribution of relative error ε% of the measures after application of the calibration matrix.

A model for the uncertainty is calculated as follows:

$$U_{B_{Ai}} \approx \sqrt{(U_{B_{Hi}})^2 + (B_{Hi}\,U_{C_{ij}})^2}$$

Where $U_i$ is the uncertainty on the *i-th* quantity.
The final uncertainty of the complete system is evaluated to be $U_{C_{ij}} \approx 0.23\%\ @2\sigma$ for any measure performed in the applicable range of the campaign. $U_{B_{Hi}} = 7\mu T$.

A similar HH coil, characterized by 4 fiducials, was lately developed in order to perform in-house calibration in any moment.

Figure 8. A similar HH coil developed to perform the calibration procedure in house.

| | |
|---|---|
| Magnetic field range | 1mT - 20mT; Short time 50mT |
| Maximal current (for 20mT) | 1.4A |
| Helmholtz Coil constant k = B/I [mT/ A] | 14.353 mT/A |
| Non-linearity error<br>in the applicable range (after 30') | 1e-5 |
| ΔH/H in 20mm sphere | < 4e-4 |
| ΔH/H in 2mm sphere | < 4e-5 |
| Resistance (series connected coils) | 63 Ω |
| Turns | 2 x 2200 x |
| Wire diameter | Ø1mm |
| Max power | 125W |





### 3. Examples of measured magnetic field

A tool is developed in .net Framework to coordinate the measurements of the Laser Tracker and the Teslameter all within a SpatialAnalyzer® (SA) environment. The software can instantly visualize the vector of the magnetic flux density inside the 3D environment of SA aligned to the CAD model of the object under inspection.

The tool was initially implemented to be flexible enough to measure a vector $\vec{B}$ in any visible and accessible position. For the present purpose some additional features were developed to streamline the process of acquisition and facilitate the sequence of actions to be performed by the operator (e.g. switch on/off the power supply of 200A DC or measure control points).

Depending on the measurements accuracy, the procedure might need a physical tool to precisely move the T-probe and keep it in a steady position for each single acquisition. If minor accuracy is acceptable, the T-probe could be moved by hand and the acquisition process might be significantly faster.

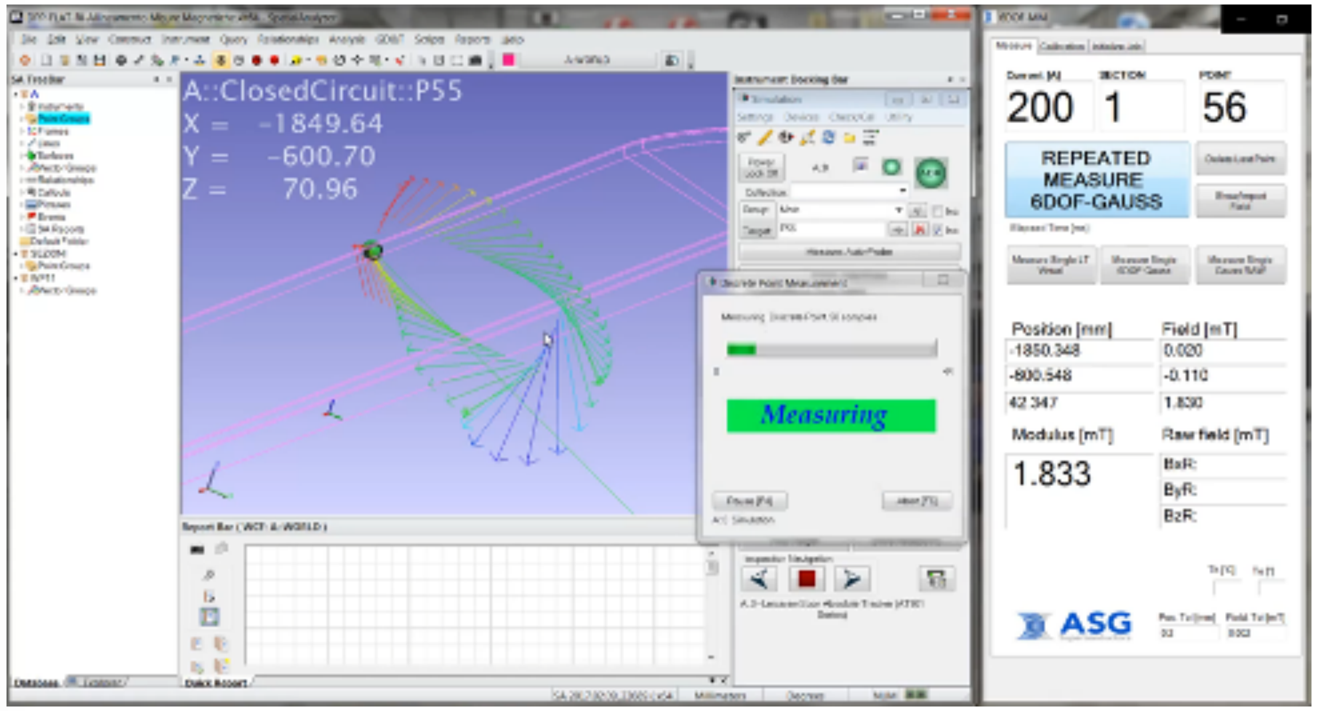


Figure 9. Snapshot of the GUI to control the 6DOF-MM device within SA.

A preliminary test was performed on the Double Pancake Prototype (DPP) coil. The line integral of the magnetic field around a closed loop was measured ($\Gamma(\vec{B})$) and calculated from theory ($\Gamma_{CALC}$). The relative difference was found to be only 0.14% despite the coarse grid used for the numerical approximation of the integral.

$$\Gamma(\vec{B}) := \oint \vec{B} \cdot d\vec{l} = \oint \vec{B} \cdot d\vec{l} \approx \frac{1}{2} \sum_i (\vec{B}_i + \vec{B}_{i+1}) \cdot (\vec{r}_{i+1} - \vec{r}_i) = -4530.2\ mT \cdot mm$$

$$\Gamma_{CALC} = \mu_0 \sum_i I_i = -4\pi \cdot 10^{-7} \cdot 12 \cdot 300\ T \cdot m = -4523.9\ mT \cdot mm$$

$$\varepsilon_\Gamma = \frac{\Gamma(\vec{B}) - \Gamma_{CALC}}{\Gamma_{CALC}} \% = 0.14\%$$

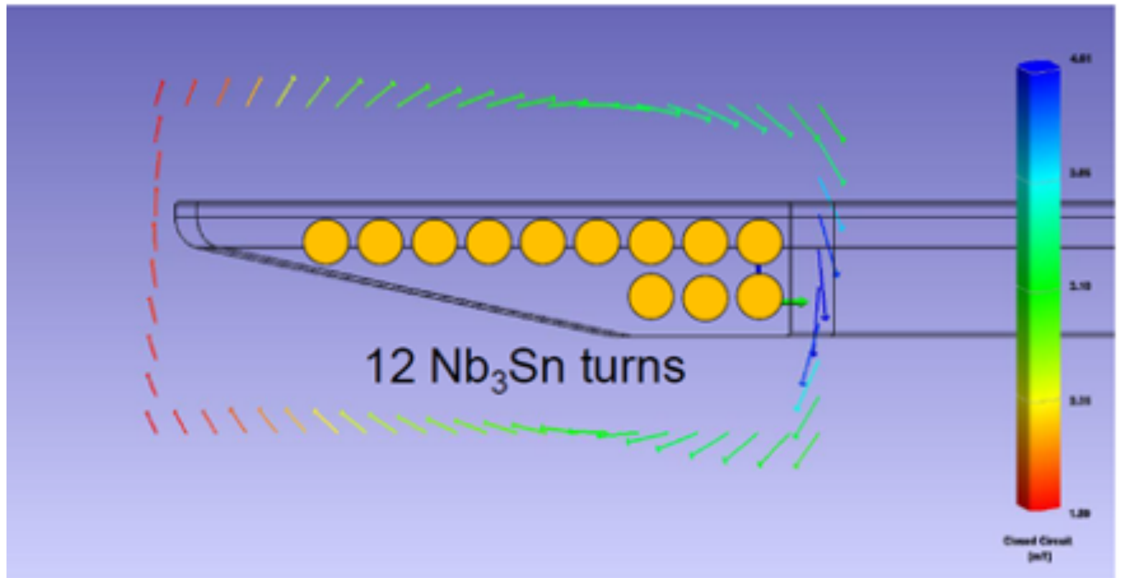


**Figure 10.** Line integral measure around a section of Double Pancake Prototype (DPP).

Measures on the WPs cannot be performed at nominal current of 68kA due to physical constraints. Therefore, a steady DC current of 200A is applied to the winding. The higher the current, the lower the noise to signal ratio. So, in principle, the current should be maximized. Pre-existent studies and practical tests had shown that, to avoid significant deformations due to thermal expansion, it is necessary to keep an unsteady current throughout the duration of the whole survey.
The complete set of measurements could take up to 40 non-consecutive hours, therefore waiting for the thermal stabilization of the system is not worth the effort. For this reason, the current is switched on and off at each measuring section in order to minimize the thermal drift and avoid temperature compensations. Current stabilization is long enough to neglect any contribution from eddy currents.

All the ten Toroidal Field Winding Packs manufactured in ASG were measured with the described technique. Some snapshots of the WPs measured in 2017 are shown in the following pictures.

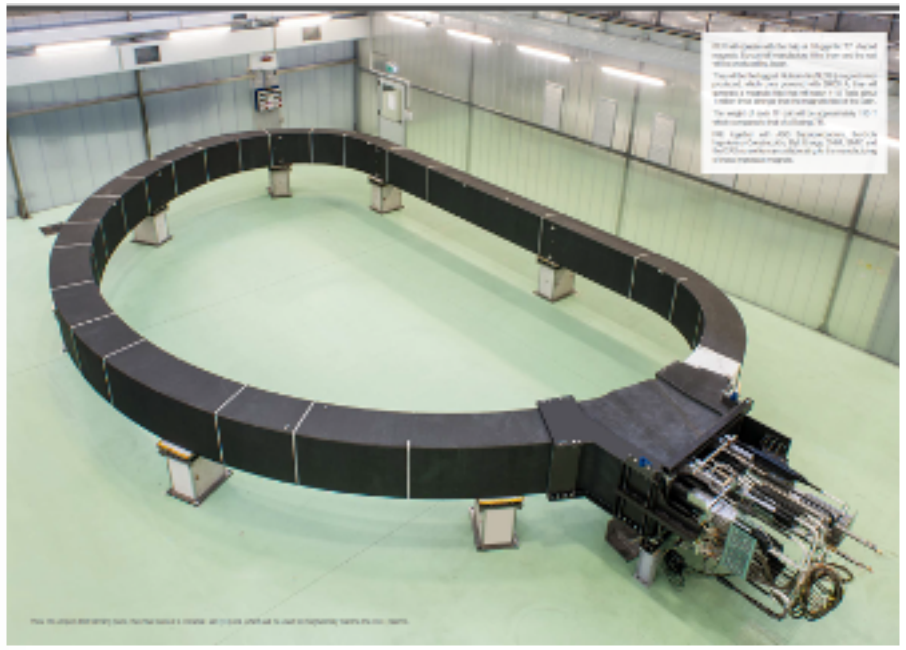

**Figure 11.** View of a WP inside the dedicated a-magnetic clean area at ASG premises (La Spezia). White tape visible on the coated surface was used to visualize the location of the sections to be measured and simplify the preliminary alignment of the device.

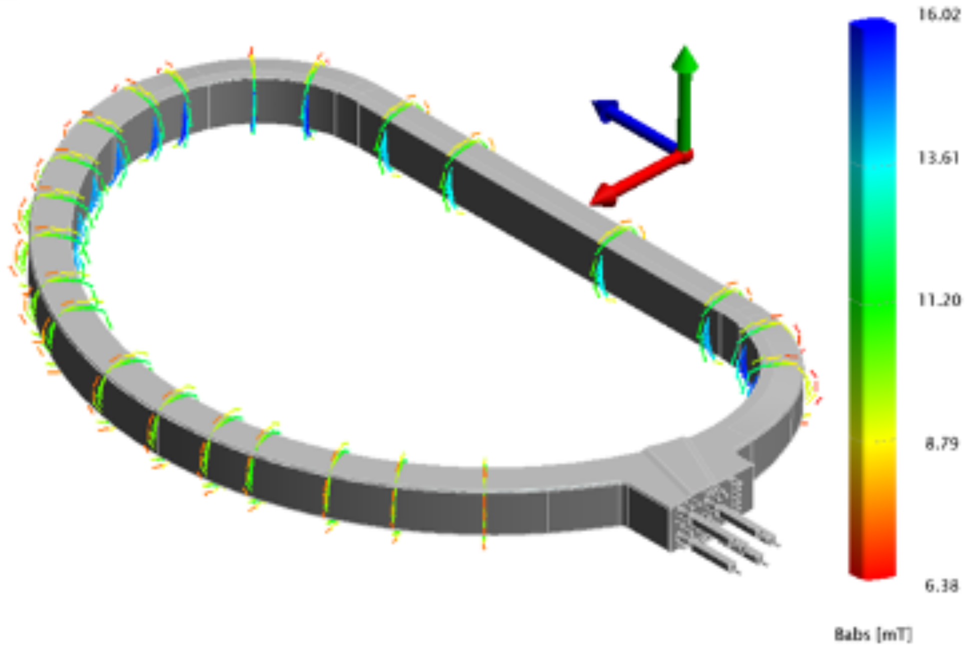


**Figure 12.** View of the entire WP magnetic flux density field at reduced current (200A) after numerical removal of the geomagnetic stray field. Vectors are proportional to the intensity |B| and are represented in the TGCS frame.

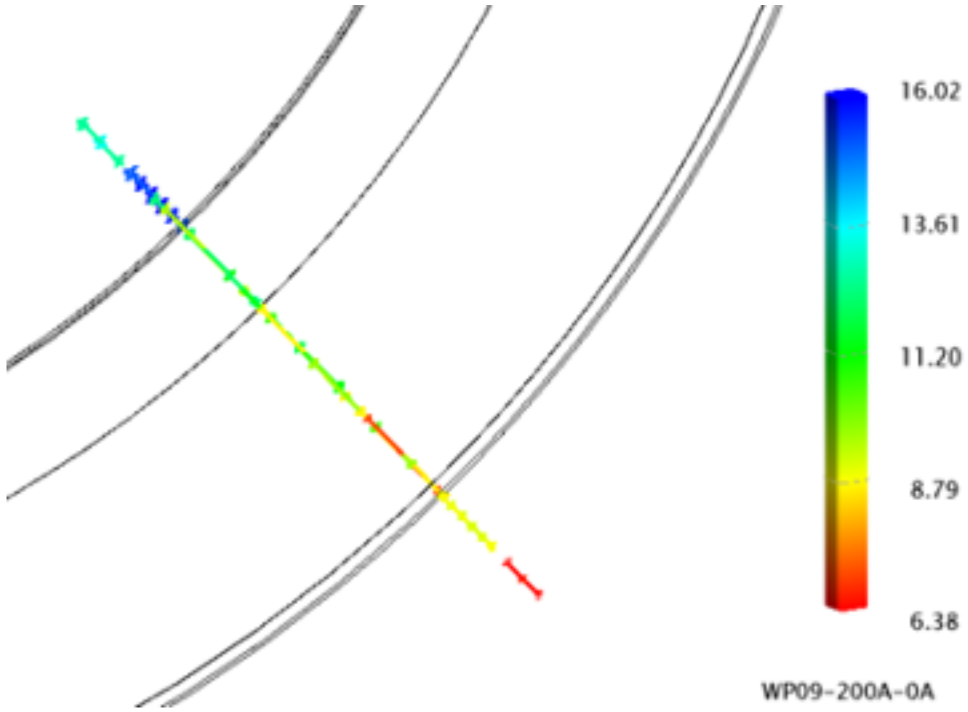


**Figure 13**. View of the magnetic field at reduced current (200A) after numerical removal of the stray field of a single section.

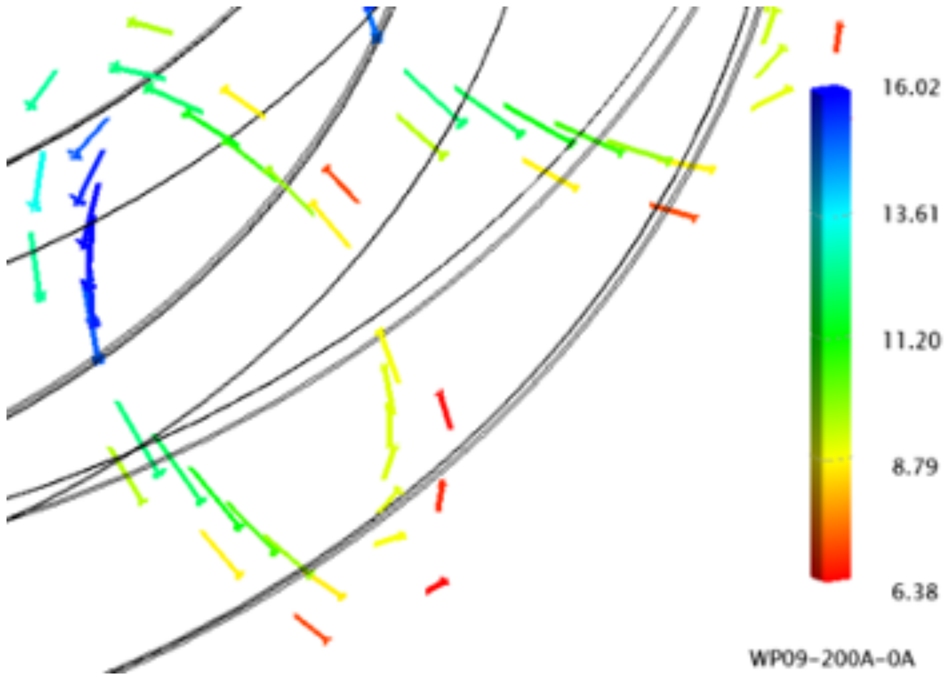


**Figure 14**. View of the magnetic field at reduced current (200A) after numerical removal of the stray field of the section in Figure 12.





## 4. Measurement statistics on 6 WPs

In the following pages, some statistic elements of the vector fields measured on 6 manufactured WPs are illustrated.

Definition: **Standard deviation σ** of the vector field of WPs at acquisition point "i"

$$\sigma_i = \sqrt{\frac{1}{N-1}\sum_{WP}\left(\vec{B}_{WPxi} - \left\langle \vec{B}_{WPxi}\right\rangle_{WP}\right)^2} \cdot 100\% \qquad \text{for } WP = 1, .., 6$$

Definition: **Magnetic Field Relative Difference** between WPx and average vector field of WPs at acquisition point "i"

$$\frac{dB_{WPi}}{B} = \frac{\| \vec{B}_{WPx} - \langle \vec{B}_{WPx} \rangle_i \|}{\| \langle \vec{B}_{WPx} \rangle_i \|} \cdot 100\%$$

Definition: **Geometrical Mean Deviation from Average**

$$\langle ds \rangle_{WP} = \left\| \left\langle d\vec{r}_{WPx} - \langle d\vec{r}_{WPx} \rangle_{WP} \right\rangle_i \right\|$$

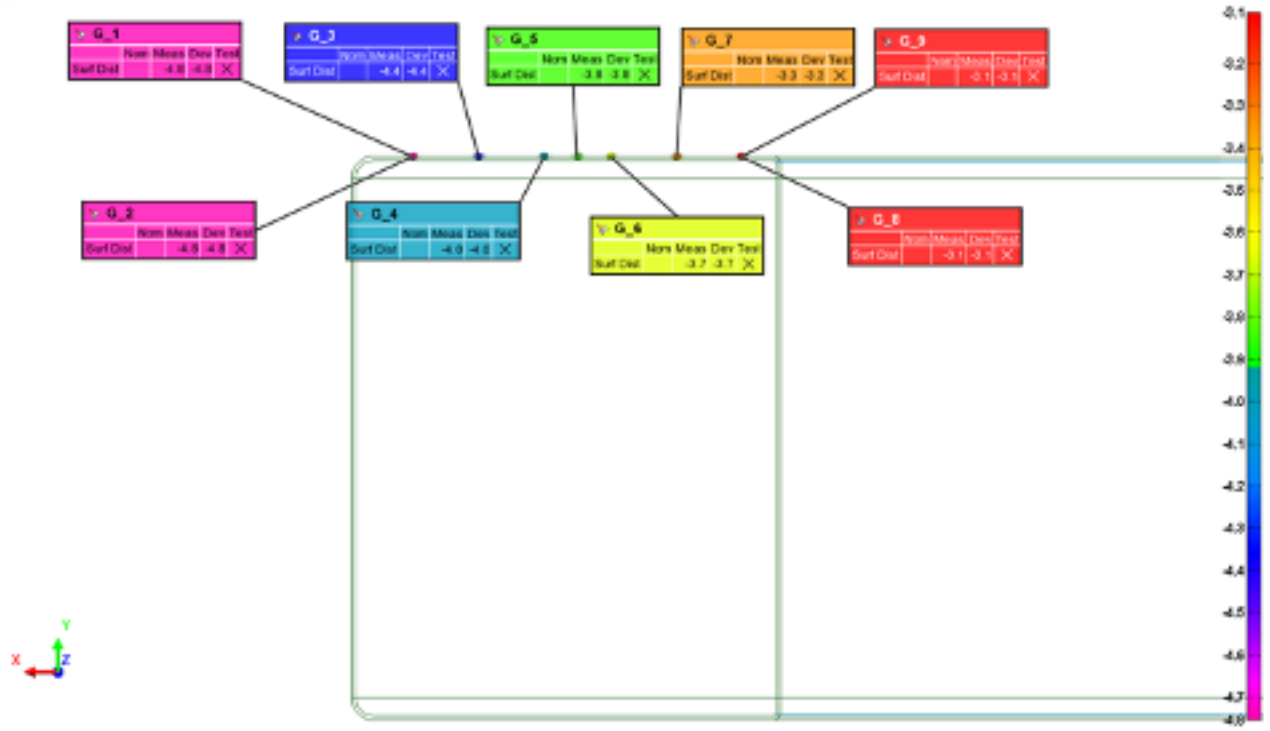

**Figure 15**. Deviation of the measured geometric surface from the nominal in correspondence to the projection of the measured magnetic points on the WP.

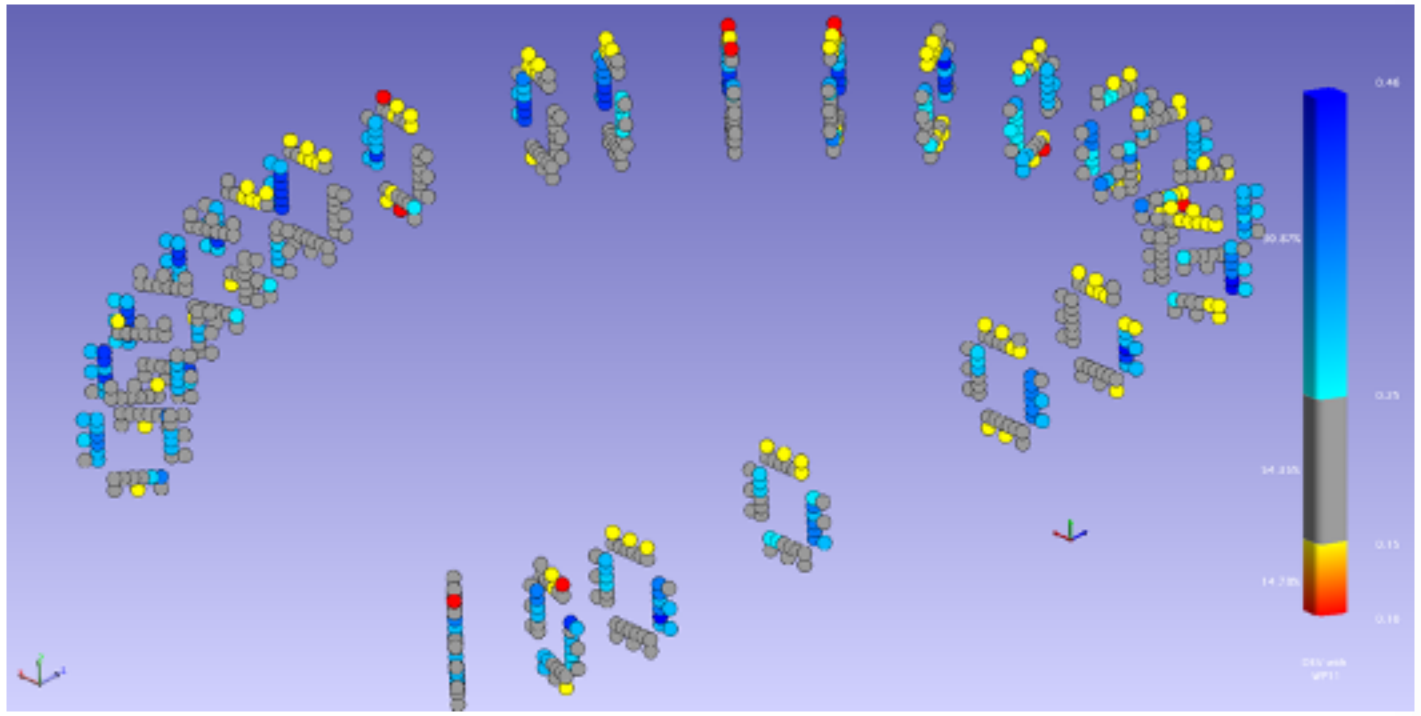

**Figure 16**. Standard deviation σ of 6 vector field of 6 different WPs [mT].

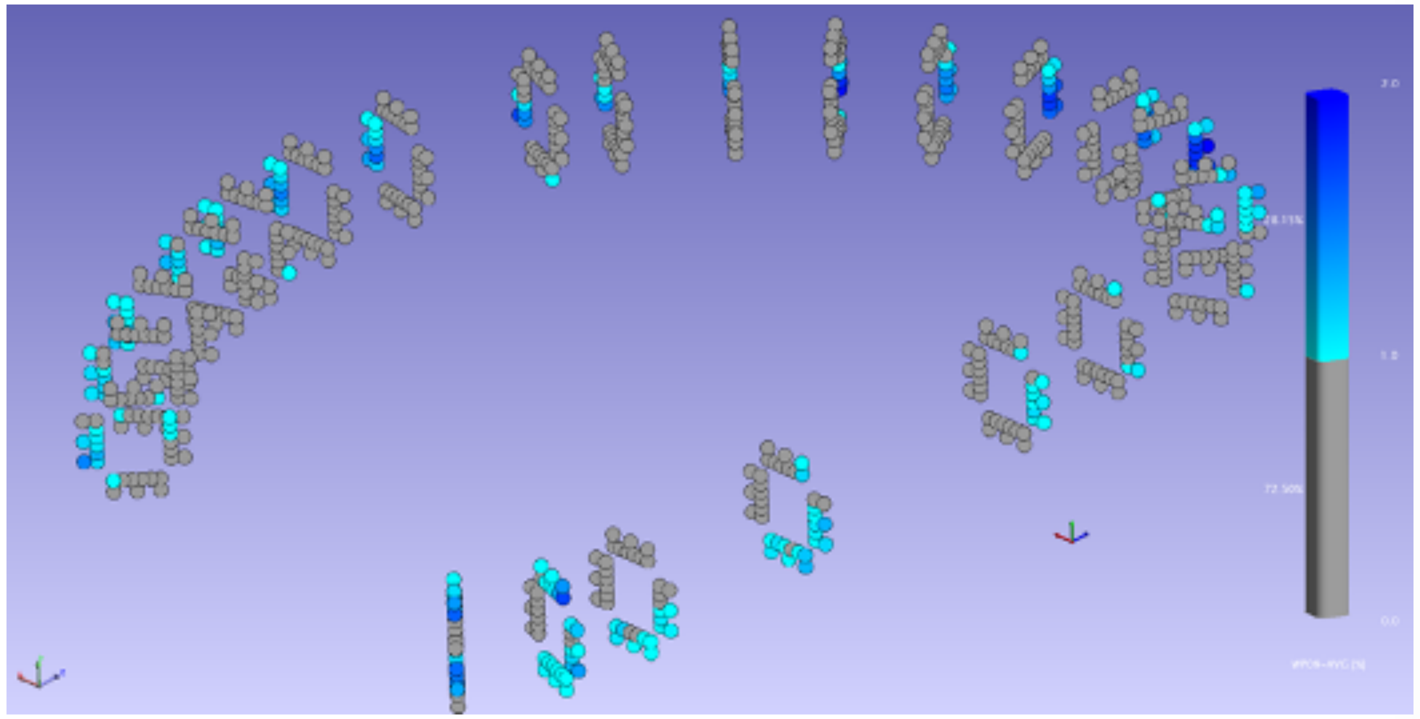

**Figure 17**. Relative difference $dB/B$ between WP09 and average.





In Figure 18 it is possible to appreciate the consistency of the geometrical manufacturing (horizontal axis) with respect to the consistency of the resulting magnetic field at reduced current (vertical axis).

Consistency of manufacturing is crucial to maximize the quality of the magnetic field generated by the Tokamak[6]. The more similar the WPs the higher the quality of the field.

[6] N. Mitchell and J. Knaster: "Contribution to Plasma Error Fields from the CS, PF and TF coils", ITER_D_23DVQU, v. 1.3: 2 September 2006.

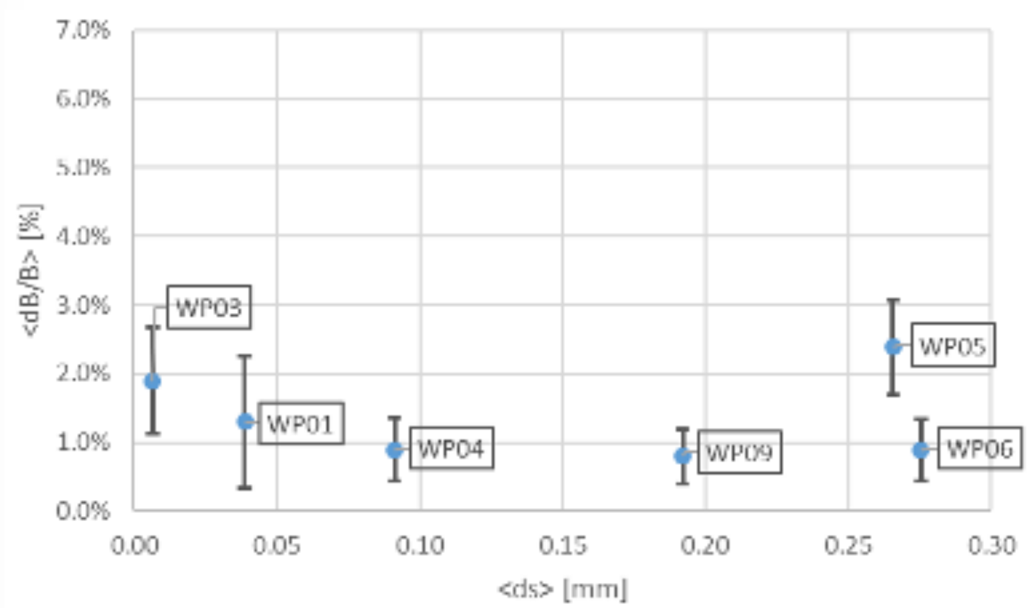


**Figure 18.** "Average Magnetic Field Relative Difference" <dB/B> plotted against the Geometrical Mean Deviation from Average $\langle ds \rangle$. Black error bars shows the standard deviation of the "Magnetic Field Relative Difference per each WP"

# SAFETY CAMPAIGN


**ASG Superconductors 2020/21 safety campaign is underway**

ASG Superconductors' safety campaign 2020/21 aims to strengthen awareness of concepts related to safety in the workplace. It presents a series of initiatives, relevant to all who work in the company, to encourage safety-conscious behaviour and compliance with the rules.

Safety in the workplace is the responsibility of every individual and is reliant on us all being aware of and implementing the internal rules and procedures. The campaign aims to remind us all of the need to avoid accidents, to protect the health of ourselves and our colleagues and to make our working environment, in which we spend much of our day, safer and more pleasant.

Safety awareness is of course not a new-born concept in ASG but a long-established and continuously improving aspect of our culture. This campaign is to remind us all of well-established Best Practices and to encourage us to adopt and adapt them to our specific activities and needs. In particular, we focus attention on some key concepts, including:

— Correct use of PPE, Personal Protective Equipment
— Compliance with Safety Procedures
— Collaboration and mutual respect between workers

ASG will promote these concepts through an integrated series of meetings, video conferences and training courses and will place highly visible and attractive graphic totems in company work areas, with messages and visuals aimed at raising awareness of safety and the topics connected with it. The aim is to encourage the awareness of the processes linked to this important issue which not only affects primary values such as health and safety, but which also has concrete implications in terms of business development and value creation.
The protection of the health and safety of all who work in the company is an absolute priority for ASG Superconductors and for every individual who contributes to carrying out its activities every day, from design to production line.

**Marco Carrega**
RSPP, ASG Superconductors

SAFETY CAMPAIGN

## A LITTLE CARE MAKES ACCIDENTS RARE


TO REACH A GOAL

TO RESPECT LIFE

## SAFETY IS A CHOICE YOU MAKE


TO DREAM BIG


TO WORK BETTER

SAFETY CAMPAIGN

## AT WORK, AT PLAY, LET SAFETY LEAD THE WAY


FOLLOW THE RULES


FOLLOW SAFETY PROCEDURES

## SAFETY BY CHOICE NOT BY CHANCE


TO PROTECT 100%


TO PERFORM 100%

SAFETY CAMPAIGN

## HEARING PROTECTION IS A SOUND INVESTMENT

FOR YOUR FUTURE

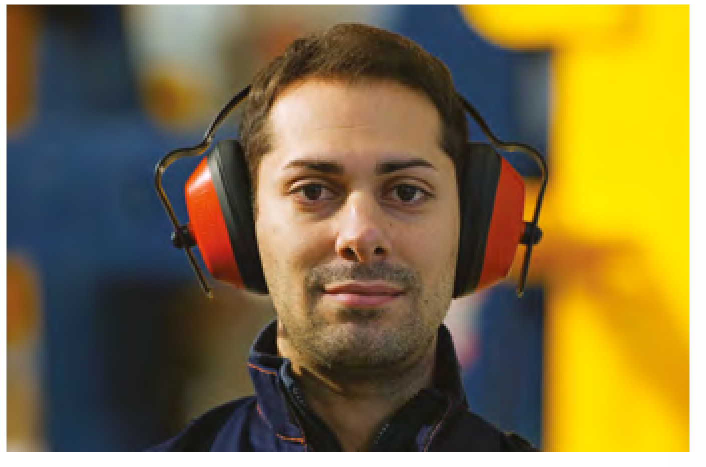

FOR YOUR SAFETY

## THE SAFE WAY IS THE BEST WAY

TAKE CARE

BE AWARE

# THE BEST MRI EXPERIENCE

The MROpen EVO is the world's only superconducting, cryogen-free MRI system, offering high quality imaging, a small carbon footprint and all of the functionality of a truly positional MRI system.

The MROpen EVO contains upgrades such as a digital spectrometer, new graphic user interface, faster scans, new coils and re-designed sequences among other features.

# MROPEN EVO THE BEST MRI EXPERIENCE THE NEXT GENERATION IN POSITIONAL MR IMAGING

Heather Mason

The MROpen EVO system is the next generation in positional MR imaging. The MROpen EVO is the world's only superconducting,wwwcryogen-free MRI system, offering high quality imaging, a small carbon footprint and all of the functionality of a truly positional MRI system.

The MROpen EVO contains upgrades such as a digital spectrometer, new graphic user interface, faster scans, new coils and re-designed sequences among other features. The wide open design of the MROpen EVO is extremely patient friendly, greatly reducing claustrophobia and offering the patient high quality diagnostic images in a comfortable scanning environment.

The MROpen EVO has an entirely new graphic interface that is moreuser friendly and offers many more parameter choices than the first generation MROpen. The new parameter selections such as percentage of phase oversampling, image filtering, number of echos, echo spacing, zero filter, partial Fourier, and more allow the user to customize their scan sequence to balance high-quality images with faster scan times as compared to our first-generation system.

I was a technologist for nearly 4 years on the first-generation MROpen prior to joining the team at ASG and while the image quality is very good on that system, the new MROpen EVO images reflect increased spatial resolution, reduced scan times compared to the original MROpen.
The digital spectrometer and re-designed sequences along with a new reconstruction algorithm are 3 additional noteworthy features.


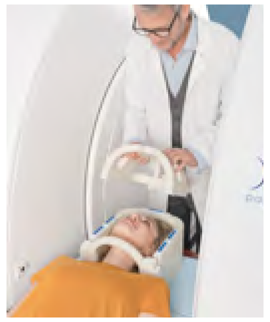

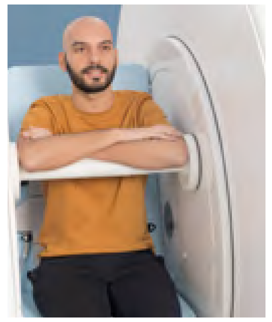

One of the challenges of using a positional, mid-field MR system such as the 0.5T MROpen is scan time. The newly designed MROpen EVO optimizes that challenge by producing faster scans as described earlier and by offering a new head and neck coil for improved neurological imaging, and a long spine coil that allows the entire spine to be imaged without taking the patient off of the table and changing coils. The patient can stay on the coil and the table can be re-centered for the anatomy of choice, and a larger effective field of view allows the user to obtain spinal images that cover the cervical spine and most of the upper to mid-thoracic spine or the lumbar spine and most of the lower to mid-thoracic spine.
This large field of view can accommodate a variety of pathologies that may extend beyond the traditional field of view such as syringomyelia, metastatic disease, scoliosis, multiple sclerosis and more. The head and neck coil (pictured above) is capable of covering both the head and neck and is optimized for angiographic exams of these areas without the need for the technologist to take extra time to change coils.
The new head and neck coil can be used with all of the routine and special imaging sequences that the MROpen EVO offers including DWI, MRA and 3D imaging.
The MROpen EVO also offers in-console post processing for MRA exams, allowing the technologist to produce Maximum Intensity Projection (MIP) cut outs of the vessels and reconstruct them in the traditional tumble and turn directions for evaluation.


Example of patient female -95yy with acute cerebral ischemia

The MROpen EVO also offers a positioning device to assist with shoulder exams which places the patient and coil in the appropriate position for image optimization so that both the patient and the coil are stabilized which reduces motion artifact and breathing motion in addition to streamlining the process of positioning the patient and coil at isocenter and improving patient comfort.
The upright/weight-bearing tools that are also available, speed up the positioning process for weight-bearing examinations in addition to increasing patient safety by stabilizing the patient in the weight bearing position. The result is an overall reduction of motion artifact and an increase in patient comfort in the weight-bearing position, ultimately improving the overall outcome.
The MROpen EVO brings to MRI state of the art positional imaging capabilities, with the head and neck coil, the long spine coil, a new graphic user interface, digital spectrometer, redesigned sequences and the shoulder positioner and weight-bearing tools, which in concert offer unparalleled patient safety, comfort and success. The MROpen EVO from ASG Paramed MRI unit truly is the next generation in positional MR imaging.

# NICA MULTI PURPOSE DETECTOR

# MPD MULTI PURPOSE DETECTOR MAGNET FOR NICA ACCELERATOR

Roberto Repetto, Simone Meneghetti, Simone Grillo, Nicolò Valle

NICA is a new complex accellerator designed at the Joint Institute for Nuclear Research (Dubna, Russia) to study the properties of dense baryonic matter.

ASG in 2016 has been awarded a contract for the construction of the magnet for the MPD, one of the largest superconductive magnet ever produced in its workshops.

The manufactoring was completed in summer 2019 and the Factory Acceptance Test was successfully awarded.

NICA (Nuclotron-based Ion Collider fAcility) is a new complex accelerator designed at the Joint Institute for Nuclear Research (Dubna, Russia) to study the properties of dense baryonic matter.
When the NICA will be ready, JINR scientists will be able to create in the Laboratory a special state of matter in which the Universe stayed shortly after the Big Bang - the Quark-Gluon Plasma (QGP).
NICA will provide variety of beam species ranged from protons and polarized deuterons to very massive gold ions. One interaction point at the NICA rings is the MPD detector for studying charged hadrons, electrons, and photons generated in heavy ion collisions at energies provided by the Collider.
ASG in 2016 has been awarded a contract for the construction of the magnet for the MPD, one of the largest superconductive magnets ever produced in its workshops. The manufacturing was completed in summer 2019 and the Factory Acceptance Test was successfully awarded.

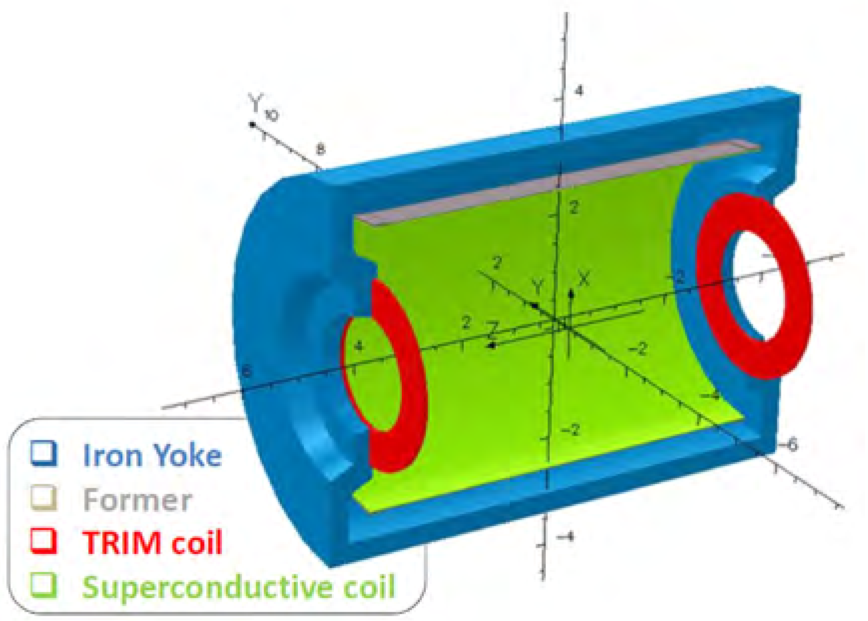


The MPD Magnet is a single solenoid more than 7 m long and with a diameter of about 5 m. The cable (custom designed on purpose) is manufactured by coextrusion of stabilizing high-purity aluminum and superconducting NbTi strand. The coil solenoid has an indirect cooling system that consists in a hydraulic LHe circuit welded directly on the coil former.





The NbTi cable has been insulated and wound from the inner side around three aluminum formers (modules), with vertical axis, by using special tools designed on purpose. Each module was impregnated with epoxy-resin into a special oven. The VPI process has been selected to get the best thermal, electrical and mechanical performances.
The three modules were then tilted into horizontal axis and assembled together by using a dedicated fixture. The connections of the electric and L-He cryogenic circuits completed the assembly phase.

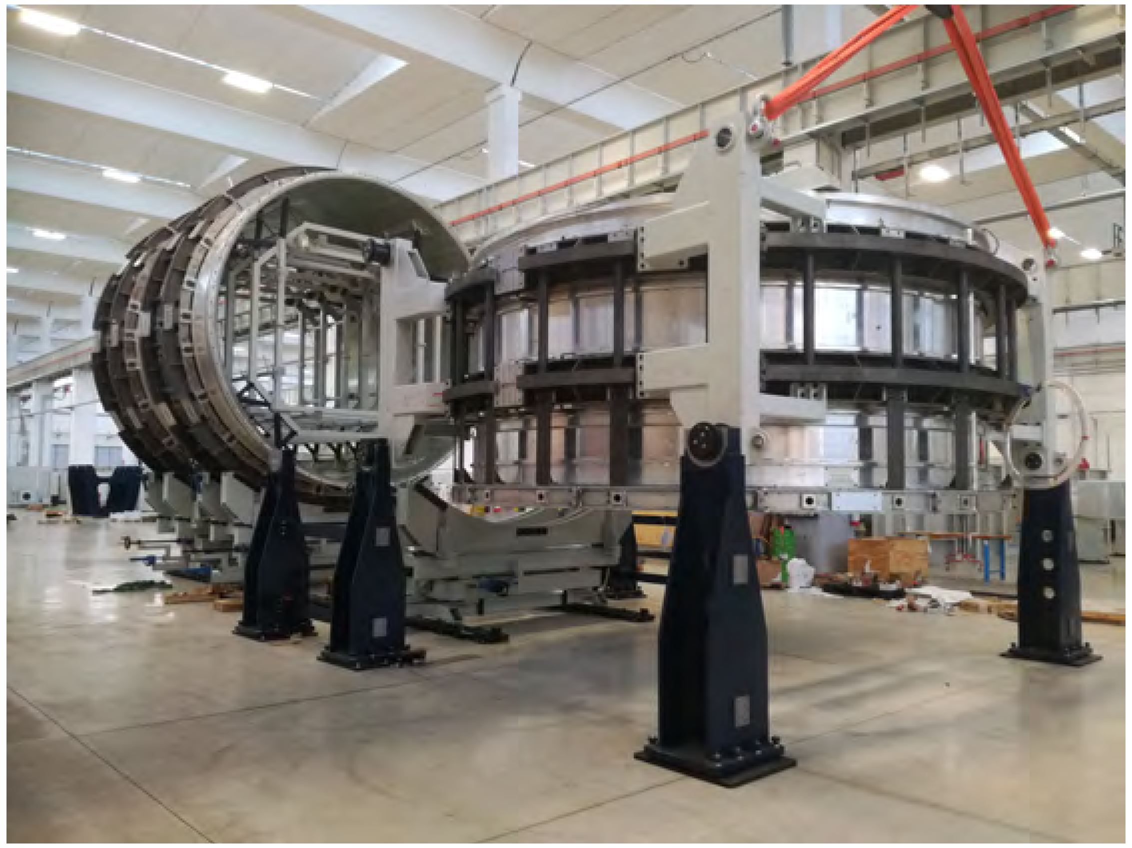

The most challenging issue of this job was to manage huge components and guarantee at the same time very tight tolerances after the assembly. These requirements were necessary to get the target field, a highly homogeneous magnetic field of 0.5 T in a cylindrical volume (2.4 m diameter, 3.4 m length). In addition, two resistive TRIM coils were manufactured to be installed at both ends of the solenoid to correct and trim the field.

| MAIN DIMENSIONS | |
|---|---|
| SC Coil Ø | 5.2 m |
| SC Coil lenght: | 7.6 m |
| SC Coil weight: | 15 Ton |
| Cryostat Ø: | 5.8 m |
| Cryostat lenght: | 8.1 m |
| TRIM coil Ø: | 3.2 m |
| TRIM coil depth: | 80 mm |
| Yoke + Coils weight: | ≈ 835 Ton |

Another challenge of this job has been to design and supply a complete keys-in-hand system, including the magnet itself with all the auxiliary systems as the power supplies, the pumping station, the cryogenic valves box and the Control System.
This last one integrates the information coming from all the systems in a user-friendly interface, to operate correctly the magnet, manages interlocks and retroactions, sets the parameters (i.e. SC cable ramp rate, temperature threshold, etc.) and switches the operating regimes, including emergencies.

# GSI SUPER-FRS MULTIPLETS

Super-FRS (Superconducting FRagment Separator) at GSI/FAIR in Darmstadt will be the most powerful in-flight separator for exotic nuclei up to relativistic energies

It is composed, among other components, by multipole superconducting magnets with very large acceptance aperture combined in different Multiplets

ASG is currently manufacturing 32 Multiplets that are required by Super-FRS separator

First of series Short Multiplet has been delivered in February 2019 and the completion of its Site Acceptance Test at CERN is scheduled for March 2020

# GSI SUPER-FRS MULTIPLETS: THE NEXT FUTURE OF PARTICLES SEPARATOR

Roberto Repetto, Giovanni Valesi, Alice Borceto, Giovanni Drago

Super-FRS (Superconducting FRagment Separator) at GSI/FAIR in Darmstadt will be the most powerful in-flight separator for exotic nuclei up to relativistic energies. It is composed, among other components, by multipole superconducting magnets with large acceptance aperture combined different Multiplets.
ASG is currently manufacturing 32 Multiplets that are required by Super-FRS separator.

**Figure 1.** First of Series Short Multiplet under test at CERN

First of series Short Multiplet has been delivered in February 2019 and the completion of its Site Acceptance Test at CERN is scheduled for March 2020 (Figure 1).
Each Multiplet houses different super-ferric magnets made by iron yoke and NbTi uperconducting coils in common cryostat, filled with Liquid Helium.

Key design challenges are the very high field quality requirements, protection against quench, high design pressure and tight mechanical tolerances.
One of the most challenging issues was to fulfill the field quality requirement for the quadrupole magnets.
The field quality requirement is rather tight while the good field region radius, wherein the magnetic field performance has to be respected is as large as 190 mm.
Furthermore, the magnetic field shows a non-linear behavior due to the highly saturated iron yoke.
Dedicated de-saturating holes were placed in the yoke cross-section to control the iron saturation and therefore meet the required field homogeneity as depicted in Figure 2.
The second challenge was to constrain the movement of the quadrupole coils as much as possible during the excitation in order to prevent recurring quenches.

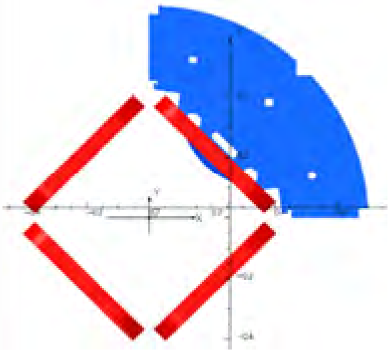

**Figure 2.** Magnetic model of super-ferric quadrupole magnet

It was concerned that the quadrupole coils could move due to the large electromagnetic force during the excitation up to the maximum current level of 330 A, therefore a quench could be triggered when all the work against the electromagnetic force dissipates in thermal energy.
To avoid recurring quenches special stainless-steel coil retainers have been designed by ASG. Those design solutions were confirmed during first of series Short Multiplet Site Acceptance Test at CERN, where a first quadrupole was successfully tested with satisfactory magnetic field quality and no quench.

Another innovating solution is applied during coil winding and impregnation manufacturing phases. Standard practice is epoxy Vacuum Pressure Impregnation in common tank. GSI Super-FRS coils are wound and impregnated in the same mold in order to reach required demanding geometrical tolerances. Dedicated shells were designed to accommodate racetrack coils (quadrupole and sextupole) in both phases.
Once the winding the phase is completed the mold is closed and filled with epoxy resin in a fully controlled vacuum pressure environment.
The solution adopted also allows to minimize the amount of resin necessary for the VPI impregnation.

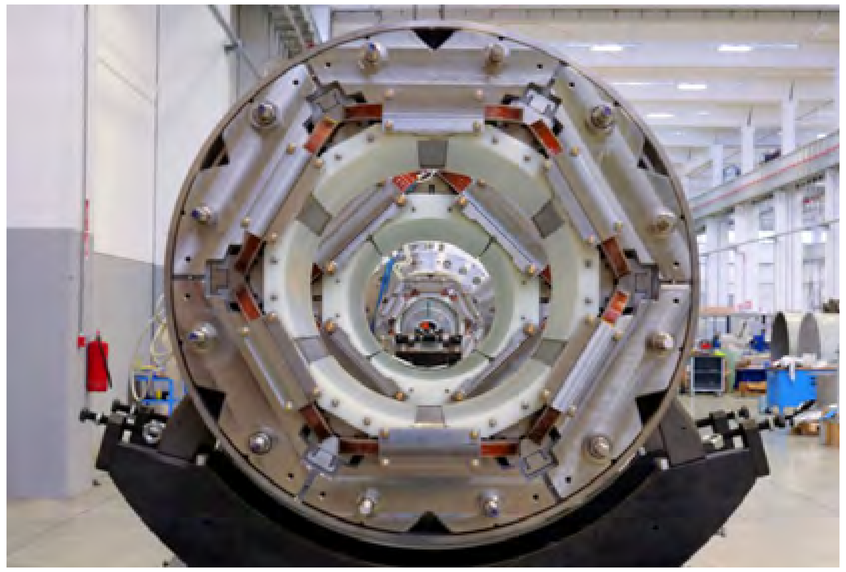

**Figure 3.** Magnets assembly inside LHe Vessel

Also the design of the LHe Vessel was very challenging as the chamber has to withstand a pressure of 20 bar, and for PED certification a pressure test of 22 bar.
Moreover, the chamber gives structural support and guarantees alignment to the magnets. Efforts are currently focused in the delivery of the first Long Multiplet (9 multipolar magnets, 70 tons weight and 7 meters length) and in the manufacturing of the Short Multiplets series, that was launched in late 2019.
Future work will aim to optimize and standardize the design of all components and proudly contribute to the progress of science with the new exiting insights the Super-FRS separator will bring into nuclear physics research.

# HTS AND LIQUID HYDROGEN

Having an extensive network of liquid hydrogen-filled pipes and containers in combination with superconducting devices was deemed inappropriate for many years.

Recently, the wind has significantly changed in favour of the hydrogen economy.

# HTS SUPERCONDUCTORS AND LIQUID HYDROGEN: IS NOW THE RIGHT TIME?

Gianni Grasso

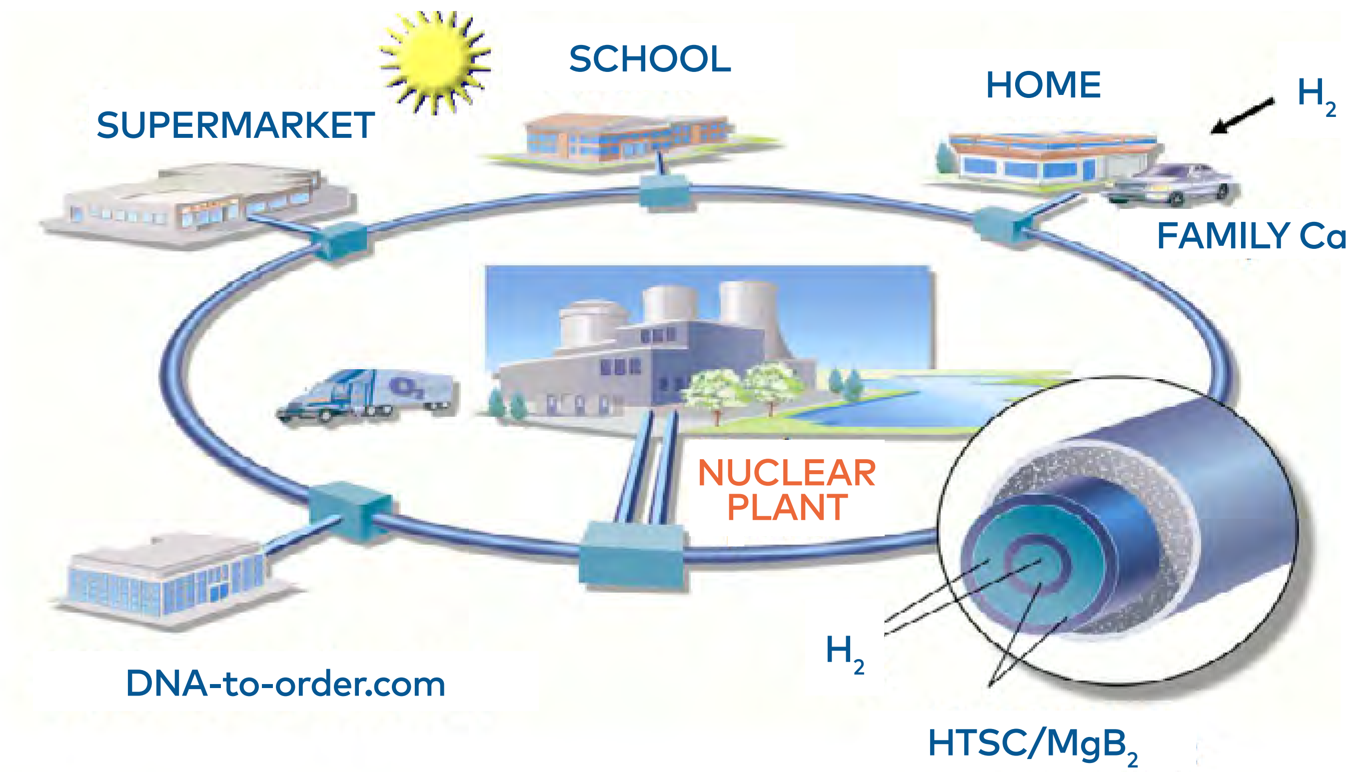

My first memory about combining liquid hydrogen and HTS superconductivity came from Paul Grant while he was at EPRI. His early 2001 Supercity sketch was very exciting particularly for me as I was starting the development of $MgB_2$ superconducting wires, which actually do quite well at a temperature of 20 Kelvin.
I include the Supercity sketch here for those who are not familiar with it with full reference to Paul (http://w2agz.com/), and in its comprehensive version including all HTS and not only $MgB_2$. Unfortunately for Paul and myself, the 9/11 event totally changed the approach to energy security and the idea of having an extensive network of liquid hydrogen-filled pipes and containers in combination with superconducting devices was deemed inappropriate for many years. For about a decade, I could not really remember any significant effort being made by anyone with this target in mind.
There was some activity about a decade ago thanks to Nobel Prize Prof. Carlo Rubbia, Dr. Vitaly Vysotski, and the late Dr. Michael Sander. At that time, we managed to put together a number of proposals aiming at demonstrating long distance power transmission and energy storage based on liquid hydrogen cooled $MgB_2$ superconducting devices.
In all cases, the concepts were very convincing and the economics were in favour of this solution. Unfortunately, it was still too early to allow people to accept the concept of using hydrogen simultaneously as a cooling medium and energy carrier.
Of the three initiatives, only Vitaly managed to bring some prototype to see the light (the Hydricity cable), and I am proud to be able to show a picture of a fully tested $MgB_2$ 15 kV cable prototype cooled by liquid hydrogen flow, taken in a Russian facility in Winter 2011.





Following this successful experiment, we have been working to demonstrate the endurance of $MgB_2$ superconducting technology in a liquid hydrogen environment but, unfortunately, we were still unable to break the barrier of scepticism against this solution.
As of today, ASG has no active projects or applications combining HTS and liquid hydrogen in a single device.
Recently, the wind has significantly changed in favour of the hydrogen economy, but I am not totally sure that the hydrogen community of today is fully aware of the tremendous advantage that they would gather from proposing solutions that combine liquid hydrogen and HTS materials.
As a matter of fact, compressed gaseous hydrogen is largely preferred to liquid hydrogen today. I wonder if the application of HTS materials may shift the preference to a liquid hydrogen technology in many cases.
Lossless energy transmission, conversion and storage all become more feasible if we join forces and combine the two technologies into one.
I am willing to write more on this topic and ask the community to do the same. We still have the time to inform about this unique chance we have been anticipating for more than two decades.

# THE NEW ASG CHALLENGE

# THE NEW ASG CHALLENGE

Gianni Grasso

The changes following the merger of ASG Superconductors, Paramed Medical Systems and Columbus Superconductors are way more far reaching and game-changing than one would have thought.

Paramed and Columbus as newer business units of the broader ASG bring different perspectives on the development of the superconducting business.

ASG Superconductors, Paramed Medical Systems, and Columbus Superconductors have recently been merged into a single entity. The changes following the merger are way more far reaching and game-changing than one would have thought, particularly for our engineering and sales people who are now better positioned to serve our customers, old and new.
The newly formed Magnets & Systems business unit of ASG brings ASG Superconductor's unique reputation and track record, developed during several decades, in supplying superconducting components to global customers. The main focus here has been essentially on **the uncompromised performance of superconductivity**. The ongoing manufacture of the huge





toroidal field coils for the gigantic ITER nuclear fusion experiment in Cadarache and of the two 11.7T UHF-MRI magnets produced in record time are live example of this.
Paramed and Columbus as newer business units of the broader ASG bring different perspectives on the development of the superconducting business. Their typical customer bases are less interested in the products' unique technical features, being rather more concerned that they can beat alternative solutions, superconducting or not, in terms of, for example, reduced ownership cost, increased efficiency and reduced drain on critical resources such as helium and rare earth elements. **The cryogen-free open-sky MRI systems** from Paramed and the **high current-density power cables**, both based on Columbus's $MgB_2$ wire technology, are two clear examples of this.
ASG Power Systems, our UK subsidiary, is also an active part of this new scenario, with its inductive fault current limiter which uses superconducting coils purely to be more compact and efficient than conventional solutions in its function to limit fault currents in electricity grids.
The possibility of fully exploiting the capabilities of the ASG Magnets & Systems business unit to conceive, design and build superconducting components & systems that would also benefit the medical and wire business units and in turn their customers, is a very rare if not unique opportunity in the superconducting industry, particularly considering that much of this work is based on the relatively youthful $MgB_2$ wire technology.
We are excited by the many new ideas and prospects that we are working on together in the new ASG – our active contribution to finally breaking the barrier of scepticism against cryo-electrotechnical devices.
So, chasing **uncompromised performance** or **cost efficiency** then?
We believe that these are **flip sides of the same coin**, and that full control of both approaches to the superconducting business is needed to make superconducting technology ready for a cleaner globe.

# SFCL

SFCL are one of the most promising solutions for the electricity grid that suppliers of superconductivity-based products.

Over this period we have seen the development of various implementations of this device, all having the same objective of acting as a dynamic impedance, intrinsically triggered by the intensity of the electrical current that flows through the device.

# SFCL: WHAT CAN WE LEARN FROM THE MRI EXPERIENCE?

Gianni Grasso

SFCL, or superconducting fault current limiters, are one of the most promising solutions for the electricity grid that suppliers of superconductivity-based products have been developing during the last 2 decades.
Over this period we have seen the development of various implementations of this device, all having the same objective of acting as a dynamic impedance, intrinsically triggered by the intensity of the electrical current that flows through the device. Heavily reducing fault currents mitigates the potential damage that may occur in the grid in case of a short circuit. Furthermore, interconnection of parallel grids through an SFCL should make the grid more flexible without increasing the potential propagation of a fault.

Clever designs have been proposed to make available in turn resistive, inductive or hybrid solutions to achieve the scope and validate the SFCL technology. Each technical approach has its PROs and CONs, including current limiting factor, recovery time, weight, power and auxiliary needs, stray field, maintenance requirements.
Depending on the specific opportunity that may envisage the adoption of an SFCL, there is typically a design that best fits the case under study. So, why don't we see many SFCL in the real electricity grid today?
The most straightforward and irreverent answer is that the SFCL solutions which are available today are more complex and expensive than the problems they are supposed to solve.

**Figure 1** Cooling of the $MgB_2$ coils of the ASG SFCL prior to type-test at IPH-Berlin

This is particularly true if we look at SFCLs in the broad sense as the devices of choice to limit fault current levels in medium voltage networks. In reality, today's devices are more suited for application in high voltage transmission grids, where fault events may create more serious damage and an SFCL may make the transmission grid more resilient and robust than today.

In our opinion, the biggest lesson that the SFCL industry community has to learn is from the recent MRI experience. Since its early days as a diagnostic tool, superconducting MRI has evolved from a niche, high-end imaging instrument to a very broadly adopted solution, with a number of global players producing thousands of systems a year at a fraction of the costs in the early days.

Furthermore, cooling solutions have progressively become so transparent for the end customer that, in the majority of cases, users tend even to forget that they are dealing with a 4K cooled magnet. Price pressure and market demand has made 1.5T MRI so robust, compact and user friendly that they cannot be competed with by non-superconducting alternatives.

**Figure 2** From a crystal glass of Champagne once in a while to a daily dose of soda

The biggest challenge we face with the SFCL product evolution is whether we will be able to find enough niche market opportunities in the immediate future (in HV grids and industrial networks where the value proposition justifies current costs) to support the actions needed to drive the cost down following the same trajectory that MRI did (but of course in much less time). We do not feel that SFCL is more technologically complex than a whole body 1.5T MRI system. Are we able to be as good as MRI engineers to follow their optimization path?

Cheers!

# PROGRESS OF $MGB_2$

Persistent mode operation is a specific feature of superconducting magnets exploiting their lack of electrical resistance to trap a current in a closed loop indefinitely.

$MgB_2$ superconductors have a chance to succeed in reaching this favourable operating mode, and to fully qualify for a variety of uses including MRI and NMR.

# PROGRESS OF $MGB_2$ TOWARDS PERSISTENT MODE OPERATION OF MAGNETS

Gianni Grasso

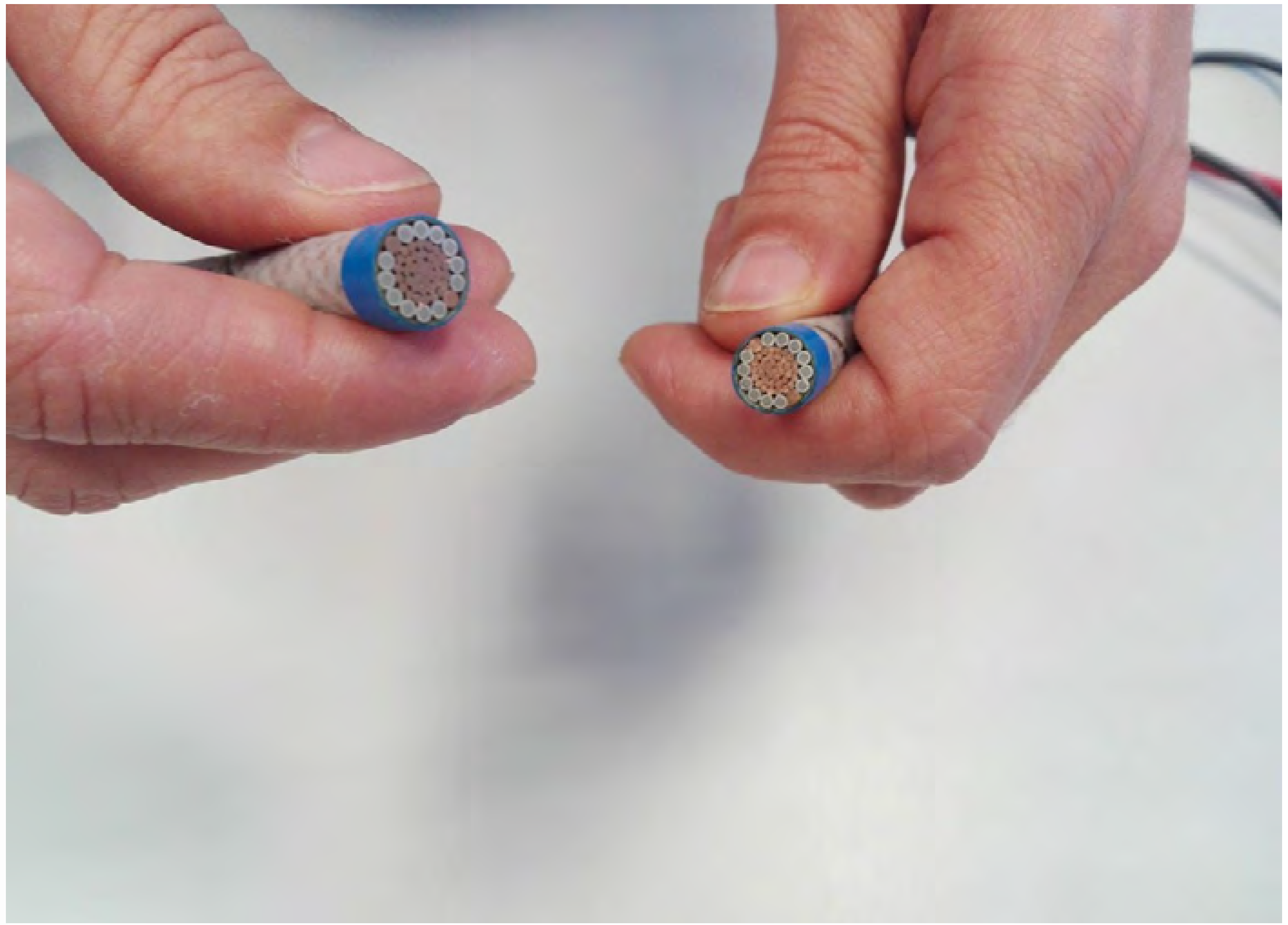

**Persistent mode operation of superconducting magnets is a competitive advantage with respect to conventional electro-magnet solutions.**
In magnetic resonance imaging (MRI) and nuclear magnetic resonance (NMR), persistent mode (PM) operation of LTS magnets allows to design and manufacture competitive zero-boil off liquid helium systems, and to achieve a superior field stability. Both have become great selling points for superconducting devices, and so they have consequently gained a large market share. The main components needed to enable PM operation are the superconducting joints and the superconducting switch.

For low temperature superconductors (LTS), various solutions have been developed and introduced in mass production of magnets with great success. Therefore, the projected implementation of high temperature superconductors (HTS) in MRI and NMR is not only determined by the availability of long, uniform, performing and affordable wires, but also by the capability to consistently operate HTS magnets in PM.

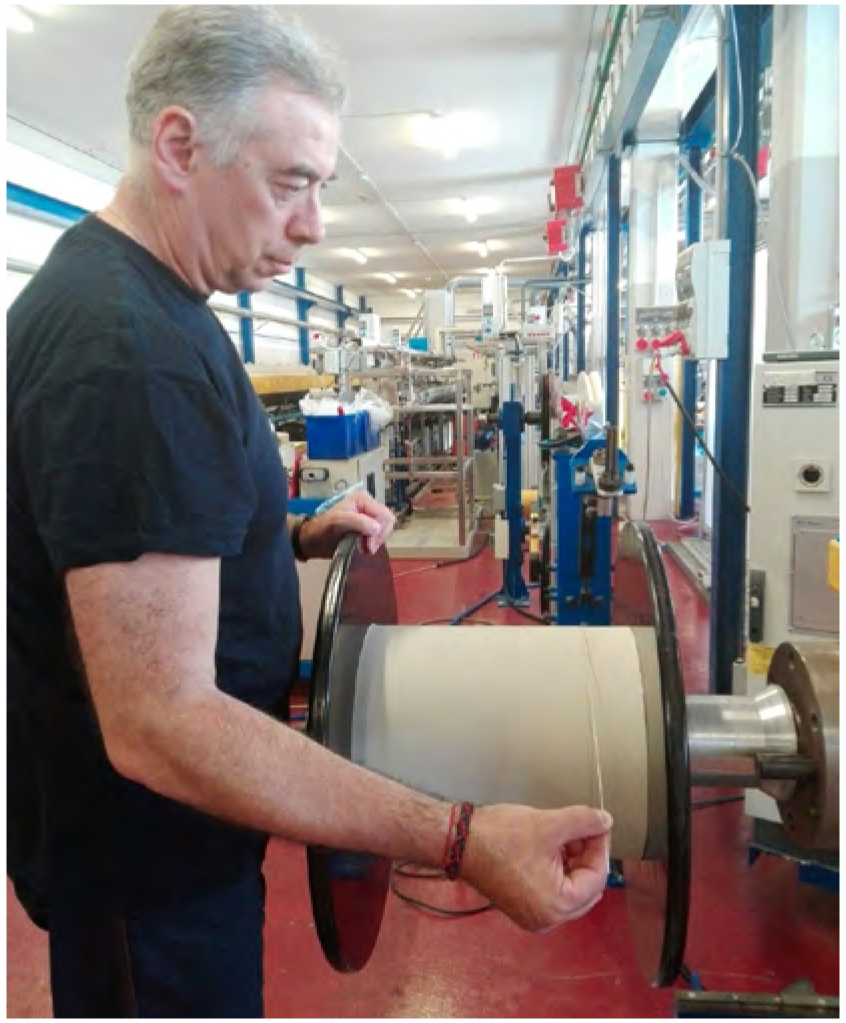





**$MgB_2$ is the HTS material with most promising impact on MRI systems.** Length, cost and performance are steadily improving and **cryogen-free operation** of $MgB_2$ based MRI magnets in the temperature range between 6 and 20K has become a realistic target. As a matter of fact, Paramed's 0.5T open MRI system[1] represents a further demonstration that the wire technology is on the right path, although being still operated in driven mode. $MgB_2$ superconducting joints and switches need a comparable level of attention than the wire itself in the path to industrialization of this material for application in MRI and NMR. Many researchers and companies ave engaged in the development of $MgB_2$ superconducting joints, and the typical answer has been substantially positive.

[1] Paramed's MR Open

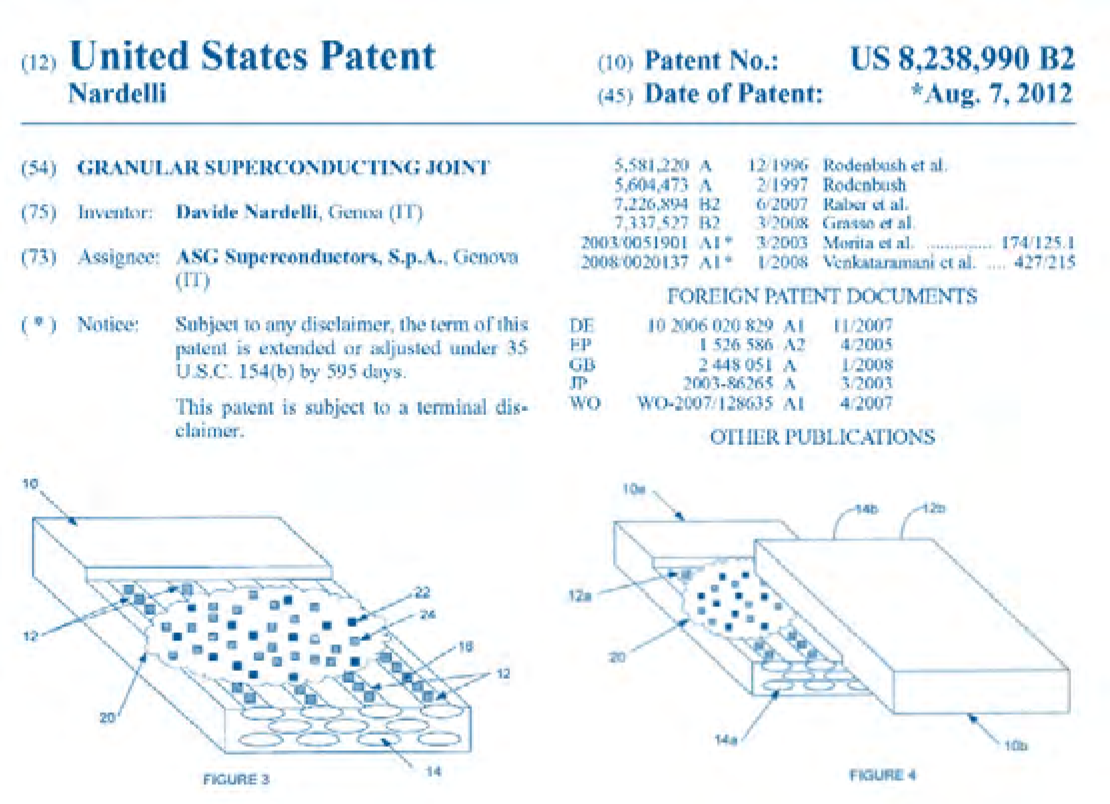
(12) United States Patent
Nardelli

(10) Patent No.: US 8,238,990 B2
(45) Date of Patent: *Aug. 7, 2012

(54) GRANULAR SUPERCONDUCTING JOINT

(75) Inventor: Davide Nardelli, Genoa (IT)

(73) Assignee: ASG Superconductors, S.p.A., Genova (IT)

( * ) Notice: Subject to any disclaimer, the term of this patent is extended or adjusted under 35 U.S.C. 154(b) by 595 days.

This patent is subject to a terminal disclaimer.

| | | | | |
|---|---|---|---|---|
| 5,581,220 | A | 12/1996 | Rodenbush et al. | |
| 5,604,473 | A | 2/1997 | Rodenbush | |
| 7,226,894 | B2 | 6/2007 | Raber et al. | |
| 7,337,527 | B2 | 3/2008 | Grasso et al. | |
| 2003/0051901 | A1 * | 3/2003 | Morita et al. | 174/125.1 |
| 2008/0020137 | A1 * | 1/2008 | Venkataramani et al. | 427/215 |

FOREIGN PATENT DOCUMENTS

| | | | |
|---|---|---|---|
| DE | 10 2006 020 829 | A1 | 11/2007 |
| EP | 1 526 586 | A2 | 4/2005 |
| GB | 2 448 051 | A | 1/2008 |
| JP | 2003-86265 | A | 3/2003 |
| WO | WO-2007/128635 | A1 | 4/2007 |

OTHER PUBLICATIONS

FIGURE 3

FIGURE 4

In spite of the brittle nature of $MgB_2$, various experts in the field have reported successful loss-less jointing, mostly on in-situ wires, by means of different technologies, including purely $MgB_2$ to $MgB_2$ joints as well as through low-melting temperature superconducting alloys. $MgB_2$ to NbTi superconducting joints were also reported, implying that a conventional LTS switch circuit may be used for magnets operated at or close to liquid helium temperature. **MIT researchers[2] have reported on an in-situ $MgB_2$ coil having a number of superconducting joints successfully operated at 0.5 Tesla.**

At ASG we have been developing a purely $MgB_2$ to $MgB_2$ superconducting joint technology applicable to fully reacted $MgB_2$ wires[3]. This is the most challenging goal as it requires the achievement of a negligible contact resistance between superconducting wires having freshly exposed filaments. Moisture and surface oxidation are the typical enemies of such process. In addition, wires with exposed filaments are subject to mechanical stresses that may introduce cracks and microstructural defects acting as supercurrent barriers.

In our process, we mechanically uncover filaments from rectangular ex-situ $MgB_2$ wires by controlled 3D milling, and then we embed the exposed surfaces in an $MgB_2$ bulk that is thermally reacted in order to maximize the contact area with the wires and minimize the contact resistance. By such process, the superconducting joint has a very compact size, and can be realized both in shaking and praying hands configuration. The superconducting joint performance is measured inductively, by determining the current decay in closed loops having a trapped current. The resistance criterion we select is very severe, of 10^-14 Ohm. After the lengthy development of the basic jointing process was completed, we engaged in a reliability test phase.

[2] Yukikazu Iwasa, "Towards liquid-helium-free, persistent-mode MgB2 MRI magnets: FBML experience", Superconductor Science and Technology, Volume 30, Number 5, pg. 53001 (2017)

[3] ASG Superconductors SpA, patent number WO2009127956A1

The very same process has been repeated multiple times in order to produce a meaningful statistic for evaluating technology readiness for industrial scale-up. After a few tens of superconducting joint trials, the achieved superconducting joint performance at 20K has been evaluated in 431 A with a standard deviation of 148 A. This value is quite promising and reflects the effective capability to produce $MgB_2$ superconducting joints with an industrial process. Effort is currently ongoing to further reduce the spread in superconducting joint performance.
Most of the residual performance variation has been attributed to specific imperfections in the superconducting loop mounting and in the soldering method of the current leads, and not to the joint itself. Future work will aim at demonstrating PM operation of $MgB_2$ magnets, followed by technology transfer of the superconducting joint process to the end users of $MgB_2$ wires in need of such technology.

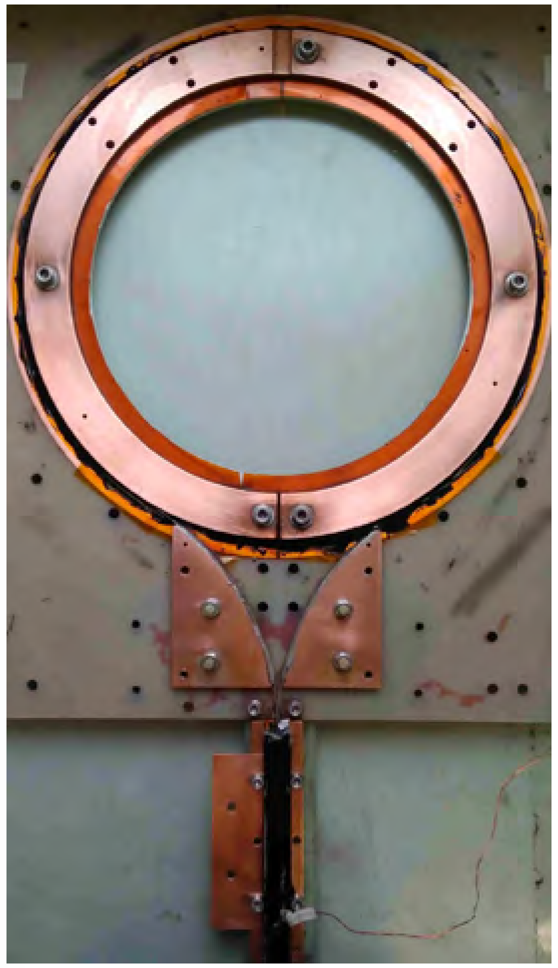

Discover the latest ASG technical articles

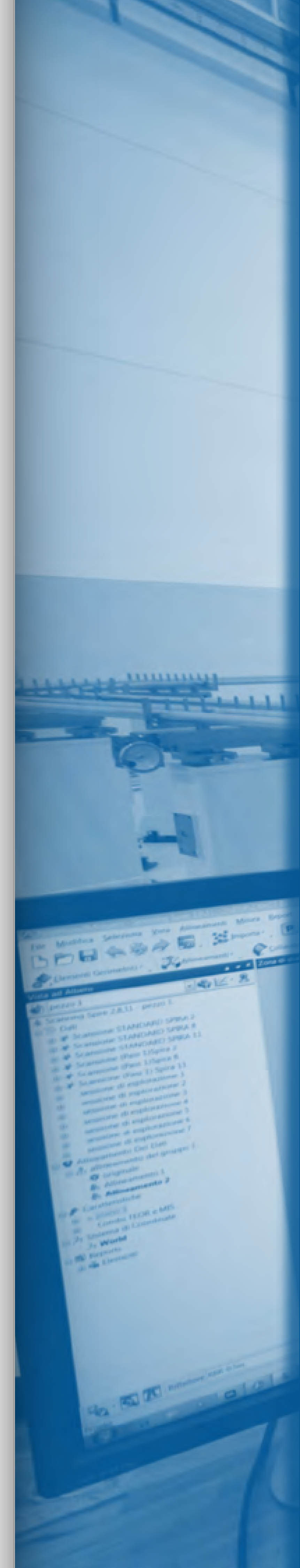

www.asgsuperconductors.com